Validatiemethoden
voor diffusiegewogen magnetische-resonantiebeeldvorming
in de witte hersenstof

Validation Methods
for Diffusion Weighted Magnetic Resonance Imaging
in Brain White Matter

Els Fieremans

UNIVERSITEIT
GENT

Promoters:

prof. dr. Yves De Deene
prof. dr. Ignace Lemahieu

Members of the examination board:

prof. dr. ir. Luc Taerwe (Ghent University, chairman)
prof. dr. Stefaan Vandenberghe (Ghent University, secretary)
prof. dr. Eric Achten (Ghent University)
prof. dr. ir. Yves D'Asseler (Ghent University)
dr. Matt Hall (University College Londen, UK)
prof. dr. ir. Patrick Segers (Ghent University)
prof. dr. Jan Sijbers (University of Antwerp)
prof. dr. Ignace Lemahieu (Ghent University)
prof. dr. Yves De Deene (Ghent University)

Ghent University
Faculty of Engineering
Department of Electronics and Information Systems
Medisip-IBBT-IBiTech
Blok B level 5
De Pintelaan 185
9000 Ghent
Belgium

Acknowledgments

The pursuit for Ph.D is proven to be a difficult road that is difficult to walk without the support and motivation of family, friends, colleagues and other supporters. So I would like to express my sincere gratitude and appreciation to everyone who has been supportive and or has contributed to this work. I especially want to thank:

Prof. dr. Ignace Lemahieu, my promotor of the MEDISIP research group. Thank you for giving me the opportunity to conduct research in the exciting multidisciplinary research field of MRI and for offering me a lot of freedom to explore and discover new research areas. I am very grateful for your continuous support to participate in international scientific conferences, workshops and courses. Those experiences definitely give an added value to this final work.

Prof. dr. Yves De Deene, my supervisor, for being a great mentor and his excellent guidance throughout this research. Thank you for helping me getting started in the diffusion MRI field, for all the feedback and clearing up my manuscripts. Your high knowledge on MRI both theoretically and experimentally, but also your enthusiasm and inspiration provided invaluable advice to me.

Prof. dr. Eric Achten from the Ghent University Hospital, for providing me with the necessary research facilities and MR scanners, for sharing his fresh ideas and helping me a lot with practical issues. I feel fortunate to have been conducting research at the MR-department of the Ghent University Hospital during a period of tremendous growth. The MR-research, under the inspirational leadership of prof. Achten, provided a great vibrant environment. I particularly value my interactions with Pieter, Benedicte, Harmen, Leslie, Karel, Ann and Marjan from the GIfMI group. Thank you for the great moments during measurements and the incredible fun we had at conferences!

Table of Contents

Acronyms, symbols and notation

List of Acronyms

ADC	apparent diffusion coefficient
ADK	apparent diffusion kurtosis
BW	band width
CNS	central nerve system
CSD	constrained spherical deconvolution
2D	two-dimensional
3D	three-dimensional
DC	diffusion coefficient
DDC	distributed diffusion coefficient
DFT	discrete Fourier transform
DW	diffusion weighted
DW-MR	diffusion weighted magnetic resonance
DW-MRI	diffusion weighted magnetic resonance imaging
DWI	diffusion weighted image
DT	diffusion tensor
DTI	diffusion tensor imaging
ELIS	Electronics and Information Systems
EPI	echo-planar imaging
FA	fractional anisotropy
FD	fibre density
FID	free induction decay
FLAIR	fluid-attenuated inversion recovery
FT	Fourier transform
GM	grey matter
GIfMI	Ghent Institute for Functional and Metabolic Imaging of the brain
H	head
HARDI	high angular resolution diffusion imaging
IBiTech	Institute Biomedical Technology

IG	internal gradients
L	left
MC	Monte Carlo
MD	mean diffusivity
MEDISIP	Medical Imaging and Signal Processing group
MR	magnetic resonance
MRI	magnetic resonance imaging
MS	multiple sclerosis
NMR	nuclear magnetic resonance
ODF	orientation distribution function
P	posterior
PD	proton density fraction
PDF	probability displacement function
PFG	pulsed field gradient
PNS	peripheral nerve system
ppm	parts per million
QMRI	laboratory for Quantitative and Molecular NMR Imaging
R	right
RA	relative anisotropy
ROI	region of interest
RF	radio frequency
SE	spin echo
SNR	signal-to-noise ratio
STE	stimulated echo
TE	echo time
TR	repetition time
TRSE	twice-refocused spin echo
VR	volume ratio
WM	white matter

List of Symbols

A	area
b	b-factor in s/mm^2
$\vec{B}$	magnetic field
χ	magnetic susceptibility
c	concentration
D	diffusion coefficient
D$_0$	diffusion coefficient of water in an unrestricted medium D$_0$ (20°C) = 2.023×10$^-$3mm^2/s
δ	small diffusion time, i.e. duration of the diffusion gradient
Δ	diffusion time
d$_w$	anomalous diffusion coefficient or walk dimension
E	energy
$\vec{e}$	eigenvector
$\vec{G}(t)$	time-dependent magnetic gradient field
γ	gyromagnetic ratio in rad/(sT)
h	Planck constant 6.62607095×10^{-34} Js
$\hbar$	Dirac constant or reduced Planck constant $\hbar=\frac{h}{2\pi}$ = 1.054571628×10^{-34} Js
I	the spin quantum number
$\vec{I_d}$	diffusion flow rate
$\vec{I_e}$	electrical current
$\vec{j_d}$	diffusion flux
$\vec{j_e}$	electrical flux density
k	Boltzmann's constant 1.3806504×10^{-23} J/K
K	diffusion kurtosis
$\vec{k}$	spatial vector in k-space
$\lambda_1, \lambda_2, \lambda_3$	the three eigenvalues of a diffusion tensor (DT)
Λ	tortuosity
$\vec{L}$	spin angular momentum
l_d	mean diffusion length $\sqrt{D_0\Delta}$
$\vec{M}$	spin magnetisation vector
$\vec{\mu}$	magnetic dipole moment
μ	mean value
$N \downarrow$	spin population in the spin-down energy state
$N \uparrow$	spin population in the spin-up energy state
ν_L	Larmor frequency in Hz

$\vec{n}$	unit vector, normal to a surface
n_d	spatial dimension
ω_L	angular Larmor frequency $\frac{\nu_L}{2\pi}$
$O(...)$	rest term including higher order terms
P	permeability
π	3.14159265
Φ	electrical potential
ϕ	porosity
ρ	surface relaxivity [μm/s]
r_{fibre}	fibre radius
r_{rms}^2	mean square displacement
$\vec{r}$	spatial vector
R^2	correlation coefficient
S	signal
s	stretching parameter
$\frac{S}{V}$	surface to volume ratio
σ^2	variance
std	standard deviation
T	absolute temperature in K
T_1	spin-lattice or longitudinal relaxation time
T_2	spin-spin or transverse relaxation time
V	volume

Notations

k	scalar
$\vec{k}$	vector
k_x	vector element
$\mathbf{K}$	tensor or matrix
K_{xy}	tensor element

Samenvatting
Summary

Samenvatting

Magnetische-resonantiebeeldvorming (MRI) is een gesofisticeerde medische beeldvormingstechniek die gebruik maakt van de grote hoeveelheid watermoleculen in ons lichaam en deze opmeet met behulp van radiogolven en het sterke magneetveld van een MRI-scanner. Een belangrijk voordeel van MRI is dat de patiënt hierbij niet blootgesteld wordt aan radioactieve straling zoals dit het geval is bij klassieke röntgendiagnostiek en computertomografie (CT). Door het grote contrastbereik van MRI in zacht weefsel wordt bovendien een gedetailleerde visualisatie mogelijk van de hersenen, het ruggenmerg, andere inwendige organen en tumoren.

Een sterk in belang groeiende tak van MRI is diffusiegewogen magnetische resonantie beeldvorming (DW-MRI). Het contrast in MR-diffusiebeelden is afkomstig van de willekeurige beweging of moleculaire zelfdiffusie van de watermoleculen in weefsel. Deze diffusie zorgt voor een verval van de opgemeten magnetisatie. Het totale effect dat geobserveerd wordt in voxels van diffusiebeelden reflecteert de (statistische) distributie van de verplaatsing van de watermoleculen in deze voxels. Deze beelden kunnen unieke biologisch en klinisch relevante informatie onthullen over de microstructuur van weefsels. Zo wordt bijvoorbeeld in hersenregio's die aangetast zijn door een acuut herseninfarct een verlaagde diffusieactiviteit waargenomen.

Omdat de mobiliteit van de watermoleculen niet noodzakelijk dezelfde is in alle richtingen, wordt het ook mogelijk om met DW-MRI anisotropie in weefsels te detecteren. Een interessant voorbeeld van diffusie anisotropie vindt plaats in de witte hersenstof die bestaat uit parallel gegroepeerde zenuwbundels of axonen. Deze axonen bestaan uit membranen en myelinewanden die obstakels vormen voor de willekeurige beweging van de watermoleculen. Hierdoor bewegen de watermoleculen makkelijker langsheen de vezelrichting dan dwars op de vezelrichting. Met DW-MRI en vezeltractografie worden de axonen van de hersenen in kaart gebracht. Dit maakt onderzoek mo-

gelijk naar de werking van het zenuwstelsel en zenuwaandoeningen in
de hersenen zoals multiple sclerose (MS) en Alzheimer.

Hoewel de eerste klinische toepassingen van DW-MRI al dateren
van 1986, zijn er nog steeds problemen met de validatie, kwantifice-
ring en interpretatie van DW-MRI data. De meetprocedure is volledig
niet invasief, wat enerzijds voordelig is voor de patiënt, maar ander-
zijds de kwaliteitscontrole en verbetering van de techniek aanzienlijk
bemoeilijkt. Er is nood aan een fysisch diffusiefantoom dat kan dienen
als gouden standaard voor de kwantitatieve validatie van DW-MRI in
klinische toepassingen. Fantomen met een gekende structuur zijn ook
gewenst voor het ontwikkelen en testen van vezeltractografie algorit-
men. Bovendien is de oorzaak van het opgemeten diffusiesignaal in de
witte hersenstof niet volledig gekend en is het nog steeds onduidelijk
wat de specifieke bijdragen zijn van de verschillende compartimenten
(diffusie in de extracellulaire en intracellulaire ruimte en uitwisseling
tussen deze). Een gekend fysisch of gesimuleerd diffusiefantoom is
ook nuttig om hierin meer inzicht te verwerven.

In deze doctoraatsverhandeling worden zowel fysische fantomen
als computersimulaties besproken voor de validatie en interpretatie
van DW-MRI data.

Fysische fantomen worden onderverdeeld in isotrope fantomen
(zoals vloeistoffen) en anisotrope fantomen. Vloeistoffen zoals water
hebben een nauwkeurig gekende diffusiecoëfficiënt en worden veel-
vuldig gebruikt om diffusiemeetsequenties te testen en gerelateerde
artefacten te beoordelen. Anisotrope fantomen zijn essentieel voor
de evaluatie van kwantitatieve anisotropieparameters zoals de diffu-
sie tensor (DT), de fractionele anisotropie (FA), en om de variabiliteit
van deze grootheden te analyseren tussen verschillende MR-scanners.
Zowel biologische fantomen (planten en gedisecteerd ruggenmerg) als
synthetische fantomen worden gebruikt voor de validatie van DW-
MRI.

Anisotrope vezelfantomen werden ontwikkeld omdat deze een goed
gekende en reproduceerbare structuur bezitten en er complexe geome-
trieën mee kunnen gemaakt worden zoals bochten en kruisende vezels.
Een vezelfantoom bestaat essentieel uit parallele synthetische vezels
die in water worden geplaatst. Door het gebruik van een krimpkous
rondom de vezels wordt een homogene, dicht gepakte vezelbundel
geproduceerd.

Een vergelijkende studie tussen verschillende vezelmaterialen (car-

bon, nylon, Dyneema® en glasvezel) werd uitgevoerd om te onderzoeken hoe de vezelafmetingen en materiaaleigenschappen van de vezels de MR diffusiemeting beïnvloeden. Enerzijds bepalen de vezeldichtheid en vezeldiameter de diffusie eigenschappen zoals de FA in de beelden. Anderzijds wordt de signaal-ruis verhouding voornamelijk bepaald door het effect van de oppervlakterelaxatie en magnetische susceptibiliteit op de T_2-relaxatietijd. De meest geschikte vezelfantomen blijken dichtgepakte vezelbundels te zijn, gemaakt van een hydrofoob vezelmateriaal met een magnetische susceptibiliteit dicht bij deze van water. Dyneema® bezit de meest geschikte vezeleigenschappen om te dienen als diffusiefantoom en werd dan ook verder gebruikt in dit werk.

De diffusie in de Dyneema® vezelbundels is opgemeten met DW-MRI en bulk MR diffusiemetingen. De diffusie in de interstitiële ruimte tussen de vezels is gesimuleerd met Monte Carlo (MC) simulaties om deze metingen kwantitatief te evalueren. De tijdsafhankelijke diffusiecoëficiënt en kurtosis werden gesimuleerd door diffunderende watermolecules in geometriën bestaande uit parallelle cylinders gepakt volgens variërende geometrieën en met variërende dichtheid. De MC simulaties bevestigen de accuraatheid en nauwkeurigheid van bestaande analytische modellen voor geordende pakkingsgeometrieën. De simulaties in de random pakkingsgeometrieën tonen een hogere FA en een langere diffusietransitietijd tussen de korte en lange diffusielimiet in vergelijking met geordende pakkingsgeometrieën. Een goede overeenkomst werd gevonden tussen de experimenteel bepaalde diffusiecoëfficiënt van een vezelfantoom met een bepaalde pakkingsdichtheid en de gesimuleerde diffusiecoëfficiënt in de random pakkingsgeometrie met overeenkomstige pakkingsdichtheid. De vezelfantomen zijn dus geschikt voor de kwantitatieve validatie van DW-MRI op klinische MRI-scanners.

Het nut van de vezelfantomen voor het ontwikkelen, testen en optimaliseren van MR diffusiesequenties en de evaluatie van beeldartefacten is geïllustreerd in dit werk. Door de flexibiliteit van de fantomen kan een anthropomorf hoofdfantoom gemaakt worden dat de belangrijkste vezelbundels in de witte hersenstof bevat. Een fantoom met kruisende vezels werd eveneens gefabriceerd, waarmee vezeltractografie-algoritmen getest kunnen worden.

De MC simulaties zijn vervolgens uitgevoerd in een geometrie bestaande uit intra- en extracellulaire compartimenten zoals in de witte

hersenstof. De simulaties werden uitgebreid om het DW-MRI signaal zelf te simuleren en ook uitwisseling van watermoleculen tussen beide compartimenten toe te laten. De geldigheid van het bi-exponentieel model en de cumulant expansievorm, beide modellen voor het DW-MRI signaal in de witte hersenstof, werd onderzocht als functie van het beschouwde b-interval en als functie van toenemende uitwisseling tussen de compartimenten.

Hoewel een bi-exponentiele functie de data goed lijkt te beschrijven, hangen de waarden van de gefitte diffusiecoëfficiënt en kurtosis sterk af van het beschouwde b-interval. Bovendien is het bi-exponentieel model, dat gebaseerd is op diffusie in de intra- en extracellulaire ruimte van de witte hersenstof, niet eenduidig interpretabel in het geval van uitwisseling tussen deze ruimtes.

De cumulant expansievorm vormt een alternatief voor het bi-exponentieel model. De diffusiecoëfficiënt en kurtosis kunnen accuraat worden gefit wanneer de hoge orde termen van de cumulant expansievorm worden meegefit. De kurtosis lijkt een nuttige parameter te zijn om de uitwisseling te meten tussen de intra- en extracellulaire ruimtes van de witte hersenstof. Het fitten van de kurtosis aan het DW-MRI signaal is nuttig om de geobserveerde veranderingen in celpermeabiliteit te koppelen aan pathologische veranderingen in de cel zoals waargenomen bij infarcten en tumoren.

Het hier voorgestelde onderzoek is uitgevoerd binnen de onderzoeksgroep MEDISIP (Medical Imaging and Signal Processing group), deel van de vakgroep ELIS (Electronics and Information Systems) en IBiTech (Institute for Biomedical Technology), Universiteit Gent. De MRI metingen werden uitgevoerd in samenwerking met de MR afdeling en GIfMI (Ghent Institute for Functional and Metabolic Imaging of the brain) van het Gents universitair ziekenhuis. De bulk MR diffusiemetingen en de fabricatie van de fantomen werden uitgevoerd in samenwerking met de onderzoeksgroep QMRI (Laboratory for quantitative and molecular NMR imaging), vakgroep Radiotherapie van het Gents universitair ziekenhuis. Dit werk resulteerde in 4 publicaties in internationale tijdschriften en verschillende abstracten en proceedings op nationale (7) en internationale conferenties (19).

Summary

Magnetic resonance imaging or MRI is a powerful medical imaging technique. This non-invasive technique utilizes a strong static magnetic field and radio frequent electromagnetic waves to align the magnetic dipole moments of water molecules in the body. Images are created based on the local density of water molecules and their mutual interactions. MRI provides great contrast between soft tissues and is generally regarded to be a safe imaging method since no ionizing radiation is used.

An important modality of MRI is diffusion weighted MRI (DW-MRI), which provides unique biologically and clinically relevant information of water in tissues that is not available from other imaging modalities. The overall effect observed in a diffusion weighted MRI image voxel reflects, on a statistical basis, the displacement distribution of water molecules which are present in that voxel. During their random diffusion driven displacement, molecules probe tissue structure at a microscopic scale. As diffusion is a three-dimensional process, the molecular mobility is not necessarily equal in all directions, which enables the detection of tissue anisotropy.

An interesting application is the diffusion anisotropy in brain white matter (WM) originating from its specific organization in bundles of more or less myelinated axonal fibres running in parallel. Assuming that the direction of the fastest diffusion indicates the overall orientation of the fibres, DW-MRI provides a way to map the spatial orientation of the white matter tracks in the brain. Fibre tractography algorithms are used to reconstruct and visualize the neural fibre tracts in the WM. DW-MRI is also useful in the diagnosis of stroke and to investigate white matter pathologies such as Alzheimer disease, multiple sclerosis (MS) and brain tumours.

Despite the fact that the first clinical applications of DW-MRI were presented in 1986, problems with validation, quantification and interpretation of the DW-MRI data still persist. A hardware diffusion

phantom serving as a gold standard for the quantitative validation of DW-MRI is crucial for clinical purposes but still not available. In addition, phantoms with a well-known anisotropic structure would be useful to develop and test fibre tractography algorithms. Moreover, the origin of the DW-MRI signal in WM is not completely understood and the contributions of the different compartments (diffusion in the intra-, extracellular space and exchange between the intra-, extracellular compartment) are elusive. A well-known physical or simulated phantom would be useful to gain more insight in this matter.

In this Ph.D. dissertation, both hardware and software diffusion phantoms are presented for the validation and interpretation of DW-MRI data.

Hardware diffusion phantoms can be classified into isotropic and anisotropic phantoms. Isotropic phantoms contain liquids such as water. They are widely used to test diffusion sequences and to evaluate related imaging artefacts. Anisotropic phantoms are essential in order to evaluate quantitatively measured parameters expressing the anisotropy such as the diffusion tensor and the fractional anisotropy (FA). They are also useful in analysing the variability of different MR-scanners in terms of anisotropy and fibre orientation. Both biological diffusion phantoms (plants and excised spinal cord) and synthetic diffusion phantoms are used for the validation of DW-MRI.

We focus here on the development of anisotropic fibre phantoms because on the one hand, they have a well-known and reproducible structure and on the other hand they can be used to imitate complex geometries such as curved fibres and fibre crossings. A fibre phantom bundle consists of parallel fibres placed in water and surrounded by a shrinking tube to pack the fibres densely.

In order to investigate how the different fibre material properties, size of the fibres and packing density influence the outcome of the DW-MRI experiment, fibre bundles are created with varying fibre density and made of different fibre materials (carbon fibre, nylon fibre, Dyneema® and fibreglass). The fibre density and fibre diameter are the two major factors determining the diffusion properties such as the FA, while the SNR is mainly determined by the surface relaxation and the magnetic susceptibility of the fibre. The most appropriate fibres to manufacture diffusion phantoms turn out to be densely packed fibre bundles made from a hydrophobic material with a magnetic susceptibility close to water. Of the tested fibre materi-

als, Dyneema® fibres show to have the best fibre characteristics for making diffusion phantoms and are used further in this work.

The diffusion in the Dyneema® fibre bundles is measured using DW-MRI and bulk NMR diffusion measurements. The measured diffusion properties are compared to simulations. The diffusion coefficient and kurtosis in the interstitial space between fibres is modelled using Monte Carlo (MC) simulations of random walkers. The time-dependent apparent diffusion coefficient and kurtosis are simulated in geometries of parallel fibres with varying packing geometries and packing densities. The MC simulations confirm the accuracy and validity of the existing analytical models for ordered packing geometries. The simulations in the random packed fibre geometries show a higher FA and a longer diffusion transition time between the short and long-time diffusion limit in comparison with ordered packing geometries. Based on the correspondence between simulations and experimental measurements, the fibre phantoms are shown to be useful for the quantitative validation of DW-MRI on clinical MRI-scanners.

Next, the MC simulations are elaborated in a geometry with intra- and extracellular compartments imitating the WM. The simulations are extended to simulate the DW-MRI signal and exchange is enabled between the different compartments. The bi-exponential model and the cumulant expansion form are evaluated as models for the DW-MRI signal in WM. The validity of these models is investigated by evaluation of the models as a function of the considered b-interval and considering the effect of exchange.

The simulated DW-MRI signal shows to be rather pseudo-bi-exponential because there is a strong dependence on the diffusion time and considered b-interval. Moreover, when assuming that a bi-exponential function models the diffusion in two compartments, i.e. the intra- and extracellular space, this model is not straightforward interpretable in case of exchange between those compartments. The cumulant expansion form is proposed as an alternative. The diffusion coefficient and kurtosis can be accurately fitted when including higher order terms in the cumulant expansion form. The kurtosis appears to be a useful parameter to measure the exchange between the intra- and extracellular compartments. It could be potentially useful to correlate the kurtosis with the observed changes in cell permeability to cell pathological changes such as during stroke and in malignant tumours.

Finally, some potential applications of Dyneema® fibre phantoms for the validation of DW-MRI are demonstrated as well in this work. As they have a well-known structure and anisotropy, they show to be suitable for sequence design, optimisation and the evaluation of imaging artefacts. Thanks to the flexibility and the variety of the shrinking tubes, an anthropomorphic head phantom containing the major WM *in vivo* fibre tracts can be created. In addition, a crossing fibre phantom is manufactured to test and evaluate fibre tractography algorithms.

The research presented here was conducted at the Medical Imaging and Signal Processing group (MEDISIP) research group, part of the Institute Biomedical Technology and the Electronics and Information Systems (ELIS) department of Ghent University. The MRI measurements were performed in collaboration with the MR department and the Ghent Institute for Functional and Metabolic Imaging of the brain (GIfMI) of the Ghent University hospital. The fabrication of the phantoms and the bulk MR measurements were performed in collaboration with laboratory for Quantitative and Molecular NMR Imaging (QMRI) of the Ghent University hospital. Our work resulted in 4 papers in international journals and several abstracts and proceedings at national (7) and international (19) conferences.

Validation Methods for Diffusion Weighted Magnetic Resonance Imaging in Brain White Matter

1
Introduction

1.1 Introduction

Nuclear magnetic resonance is the phenomenon that arises when an object -or a patient- is exposed to a strong magnetic field. An important application of nuclear magnetic resonance is magnetic resonance imaging (MRI), a powerful imaging technique primarily used to produce high quality medical images. Within this technique, diffusion weighted MRI (DW-MRI) is taking an increasingly important place. DW-MRI is a non-invasive imaging method that can measure the random motion of water molecules in all directions. In tissues containing a large number of fibres, such as skeletal muscles and brain white matter, water tends to diffuse along the direction of those fibres. This way, DW-MRI is a footprint of the organization in space of tissue microstructural components.

An interesting application in this domain is the study of the human nerve system. The brain white matter consists of bundles of myelinated axonal fibres running in parallel, which are responsible for the conduction of neural signals. Diffusion anisotropy is present because the diffusion in the direction parallel to the fibres is faster than in the perpendicular direction. Assuming that the direction of the fastest diffusion is determined by the overall orientation of fibres, DW-MRI provides a method to display the orientation of white mat-

ter tracts. The measurement of the diffusion signal and fibre tracking algorithms enable the visualization of the three-dimensional structure of brain white matter tracts. The insight in the anatomy of neural networks is of great interest for the understanding of normal and pathological brain structure which affects brain function.

Although DW-MRI is becoming a mature MRI method, the validation of this *in vivo* technique is still an issue that needs to be solved before implementation in the clinic.

A gold standard for the quantitative validation of DW-MRI is crucial for clinical purposes but is still not available. For the determination of the accuracy and precision and the evaluation of artefacts in a DW-MRI experiment, a phantom is required which has a well-known structure and diffusion behaviour similar to that in brain white matter. The use of phantoms with a well-known connectivity and anisotropy would also be useful for testing fibre tracking algorithms. Moreover, the origin of the DW-MRI signal in brain white matter is not completely understood. Several models exist, based on specific assumptions about the diffusion in the complex geometry of brain white matter. Validation of those models is also necessary.

This PhD dissertation proposes several methods for the validation of DW-MRI. The research presented here was conducted at the MEDISIP research group, part of the ELIS department of Ghent University. The MRI measurements were performed in collaboration with the MR department and the GIfMI of the Ghent University hospital. The fabrication of the phantoms and the bulk MR measurements were performed in collaboration with QMRI of the Ghent University hospital.

This research was funded by a Ph.D. grant of the Institute for the Promotion of Innovation through Science and Technology in Flanders (IWT-Vlaanderen) and by Ghent University by a specialisation scholarship (BOF). This work was also supported by an IUAP grant of the federal government of Belgium.

Our work resulted in 4 papers in international journals and several abstracts and proceedings at national (7) and international (19) conferences. A list of all publications that were published during the course of this research can be found at the end.

1.2 Outline

In chapter 2, the principles of nuclear magnetic resonance (NMR) and magnetic resonance imaging (MRI) are briefly introduced. The basics of MRI pulse sequence design, $\vec{k}$-space trajectory design and artefact reduction are mentioned. It is impossible to treat all these topics in depth in this work. The reader is referred to more specialized literature for further reading. The MR application of interest to this work is DW-MRI. A basic grounding of DW-MRI is also provided to support the material that is discussed in the later chapters. A brief description of the diffusion process and the origin of the diffusion signal in WM is given. Mathematical diffusion models are also presented, along with methods to visualize the dominant diffusion direction in brain white matter. Finally, we look at the clinical uses of DW-MRI and illustrate fibre tractography.

The following chapters report on the original contributions of this work. Several methods for the validation of DW-MRI are proposed: on the one hand by the use of hardware diffusion phantoms and on the other hand by the use of software diffusion phantoms based on analytical models and on Monte Carlo (MC) simulations of random walkers.

In chapter 3, an overview of the different kinds of diffusion hardware phantoms is given. The advantages and disadvantages for each phantom type are discussed. Further, we focus on the design of anisotropic diffusion fibre phantoms. The optimal manufacturing process for diffusion fibre phantoms is presented. Several fibre phantom materials are compared with respect to their performance in terms of signal-to-noise ratio (SNR) and diffusion properties.

Chapter 4 describes how the diffusion process in the anisotropic fibre phantoms is quantitatively validated. The diffusion in the anisotropic fibre phantoms is modelled by MC simulations of random walkers. An accurate description of the phantom geometry is provided. The time-dependence of the diffusion process and the effect of the fibre packing geometry and fibre material are discussed. The diffusion parameters extracted from the simulations are used to evaluate the MRI and bulk MR experiments of the diffusion in the fibre phantoms quantitatively. A fibre phantom can be considered as a two-dimensional (2D) porous medium. The MC simulations of random walk and the experimental results are used for the validation of the analytical models for ordered porous media.

Chapter 5 describes the applicability of the MC simulations of

random walkers for the validation of diffusion models in WM. Simulations are performed for a geometry including the main parts of the WM structure. The simulations are extended to simulate the raw DW-MRI signal. In addition, exchange between the different compartments has been studied. The bi-exponential model and the cumulant expansion form are both models for the DW-MRI signal in WM. Both models are studied as a function of the considered b-interval and by investigating the effect of exchange.

Chapter 6 presents some potential applications of the developed anisotropic fibre phantoms. They are used as test objects for sequence design and the evaluation of imaging artefacts. As the fibre bundles are mechanically very flexible, they can be used to create an anthropomorphic head phantom. In addition, a crossing fibre phantom is presented that can be used to validate fibre tractography algorithms.

Chapter 7 is the final chapter summarizing the main contributions of this work. Some aspects for future study are mentioned as well.

2

Diffusion Weighted MRI in Brain White Matter

2.1 Introduction

Magnetic resonance imaging (MRI) is a powerful medical imaging technique that enables the visualization of structure and function *in vivo* because of large contrast within soft tissue. An additional advantage is that non-ionizing radiation is used to acquire an MR-image. Diffusion weighted magnetic resonance imaging (DW-MRI) is a growing application within the field of MRI. A correct understanding of DW-MRI requires first of all a basic knowledge of MRI. Therefore, this chapter explains the principles of nuclear magnetic resonance (NMR) and image formation in a nutshell. Also, the basics of pulse sequence design, $\vec{k}$-space trajectory design and artefact reduction, all substantial research fields on their own, are mentioned very briefly here. For more in-depth information on these topics we refer to literature [1–4].

Once we have explained the theory of self-diffusion and the origin of the diffusion signal in the brain, we introduce the concepts of diffusion weighted magnetic resonance imaging (DW-MRI) concisely. The concept of the diffusion tensor and methods to characterize and visualize the dominant direction of diffusion are introduced whereby

Nucleus	Spin quantum number I
^{1}H	1/2
^{13}C	1/2
^{19}F	1/2
^{31}P	1/2
^{23}Na	3/2

Table 2.1: Spin quantum numbers for some nuclei.

we also discuss more refined models to describe the diffusion weighted signal. Finally, some clinical applications are addressed and fibre tractography is illustrated.

2.2 Basic principles of magnetic resonance imaging

2.2.1 Short historical overview

The property of NMR was first described by Rabi in 1938. In 1946, Purcell [5] and Bloch [6] showed NMR in fluids, work for which they received the Nobel prize in Physics in 1952. Since then, NMR has become a powerful tool for the chemical and structural analysis of substances. In 1973, Lauterbur [7] and Mansfield [8] used the principles of NMR to produce non invasive images of the body. For this work, they were both awarded with the Nobel prize in Medicine and Physiology in 2003. Since the seventies, MRI has been applied in many biomedical, chemical and engineering applications.

2.2.2 Spin physics

The spin and magnetic moment of protons

The atomic nucleus, consisting of neutrons and protons, has the quantum mechanical property of a spin angular momentum $\vec{L}$. Atomic nuclei with an odd number of neutrons or protons also possess a magnetic dipole moment $\vec{\mu}$ which is related to the spin angular momentum $\vec{L}$ by:

$$\vec{\mu} = \gamma \vec{L},$$

with γ the gyromagnetic ratio of the considered nucleus.

The spin angular momentum $\vec{L}$ is characterized by the spin quantum number I, an intrinsic property of the nucleus (see table 2.1). To exhibit the property of magnetic resonance, the nucleus must have a non-zero value of I, which is the case when the number of neutrons or protons in the considered nucleus is odd. For the majority of clinical MR-exams, and also for this thesis work, the proton (^{1}H) is the nucleus of interest, because of its high natural abundance under the form of H_2O in the human body. However, other nuclei such as ^{19}F, ^{13}C, ^{23}Na and ^{31}P can also be studied with NMR.

According to quantum mechanics, the intrinsic angular spin momentum $\vec{L}$ of a proton is quantized, which means that its measurement along the z-axis can only result in two values, $\pm\frac{\hbar}{2}$, where $\hbar$ is the Dirac constant. Consequently, when measuring the magnetic moment $\vec{\mu}$ along the z-axis, only two components are possible. This phenomenon comes to expression when the protons are placed in a magnetic field. The potential energy of a proton with a magnetic moment $\vec{\mu}$ in a magnetic field $\vec{B}_0$ is then:

$$E = \vec{\mu}.\vec{B}_0 = \begin{cases} -\frac{1}{2}\gamma\hbar B_0 & \text{spin down} \\ +\frac{1}{2}\gamma\hbar B_0 & \text{spin up.} \end{cases}$$

This phenomenon is called the Zeeman splitting and is shown as an energy level diagram in figure 2.1. The two energy levels are commonly referred to as "spin-up" and "spin-down" with the spin-down state having higher energy than the spin-up state. Transitions between the two levels can be induced by absorption or emission of a photon of frequency ν_L such that:

$$E_{foton} = h\nu_L = \Delta E = \gamma B_0 \hbar$$
$$\nu_L = \frac{\gamma}{2\pi} B_0,$$

where h is the Planck constant and ν_L is called the Larmor frequency. Replacing the frequency by the angular frequency gives the Larmor equation which underpins NMR:

$$\omega_L = \gamma B_0. \tag{2.1}$$

In an external magnetic field, the spins of all protons together result in a net magnetic momentum with the population of spins distributed amongst the two energy levels according to the Boltzmann statistics:

$$\frac{N\downarrow}{N\uparrow} = e^{\frac{-\Delta E}{kT}} = e^{\frac{-\gamma\hbar B_0}{kT}}, \tag{2.2}$$
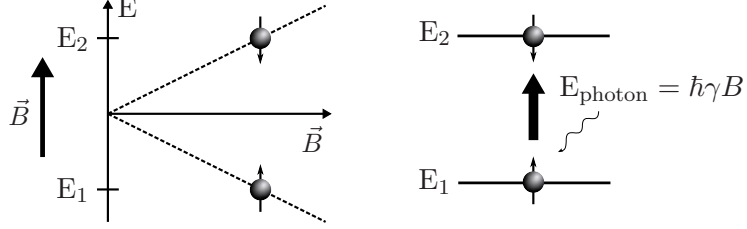
Figure 2.1: Illustration of the Zeeman effect for a proton spin in an external magnetic field $\vec{B}$. A proton spin can be excited to a higher energy level by absorption of a photon with the Larmor frequency.

where k is the Boltzmann's constant, T the absolute temperature and $N\downarrow$, $N\uparrow$ the spin populations in the spin-down and spin-up state respectively. In a magnetic field of $3T$ and at normal body temperature ($310K$), the fractional excess of protons at the low energy level is only about 10^{-5}. Nevertheless, this small difference is significant, and is measurable on a macroscopic scale as an isochromat. An isochromat is a physical construct containing a large population of spins within a very small region of space. Isochromats are small enough that microscopic field inhomogeneities have spatial dimensions much larger than the isochromat dimension. They are much smaller than a voxel [1].

The bulk magnetisation of an isochromat $\vec{M}$ is now:

$$\vec{M} = \chi \vec{B}_0 \approx N \frac{\gamma^2 \hbar^2 B_0}{4kT}, \qquad (2.3)$$

where N is the number of spins in the isochromat. The factor χ links the magnetisation of the isochromat with the static field strength and is called the magnetic susceptibility. The magnetic susceptibility is usually expressed in parts per million (ppm). Being able to treat the behaviour of all spins in the system in terms of a net magnetisation vector $\vec{M}$ allows a classical description of NMR, which gives a more feasible picture of the NMR experiment.

Spin relaxation - Bloch equations

When the spin magnetisation vector $\vec{M}$ is placed in a magnetic field $\vec{B}_0$, $\vec{M}$ will experience a torque. The equation of motion for $\vec{M}$ is

---

[1] A voxel (a combination of the words volumetric and pixel) is a volume element, representing a value on a regular grid in three dimensional space.

(a) (b)
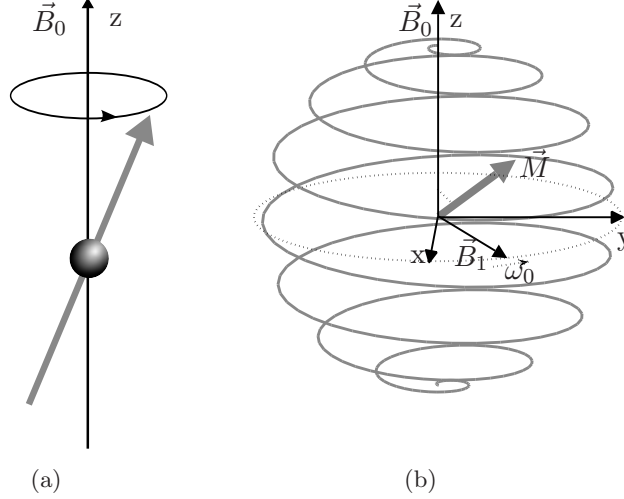
Figure 2.2: (a) A proton precesses in a magnetic field $\vec{B}_0$ similar to the movement of a top in the earth gravitational field. (b) The magnetic moment $\vec{M}$ precesses under the influence of a longitudinal field $\vec{B}_0$ and a transversal field $\vec{B}_1$

then:

$$\frac{d\vec{M}}{dt} = \gamma\vec{M} \times \vec{B}_0. \tag{2.4}$$

If $\vec{B}_0$ is a static magnetic field along the z-axis, equation (2.4) becomes:

$$\frac{dM_x}{dt} = \gamma M_y B_0 \qquad \frac{dM_y}{dt} = -\gamma M_x B_0 \qquad \frac{dM_z}{dt} = 0,$$

which results in the following solutions:

$$
\begin{aligned}
M_x(t) &= M_x(0)\cos(\omega_0 t) + M_y(0)\sin(\omega_0 t) \\
M_y(t) &= -M_x(0)\sin(\omega_0 t) + M_y(0)\cos(\omega_0 t) \\
M_z(t) &= M_z(0),
\end{aligned}
$$

with $\omega_0 = \gamma B_0$. The x-, y- and z-directions are indicated on figure 2.2. These equations describe the precession of the magnetisation vector around the z-axis as shown in figure 2.2(a). This precession is similar to that of a spinning gyroscope when placed in the earth's gravitational field. The angular frequency of the precession is the

Larmor frequency ω_L as described above in equation (2.1), showing how the classical and quantum mechanical description coincide.

Subsequently, when a time varying field $\vec{B}_1$ perpendicularly to $\vec{B}_0$ and oscillating at ω_L is superimposed, the solution of equation (2.4) results in a magnetisation $\vec{M}$ which precesses simultaneously about $\vec{B}_0$ at ω_0 and $\vec{B}_1$ at $\omega_1 = \gamma B_1$, as shown in figure 2.2. In fact, applying a $\vec{B}_1$-field has the effect of rotating the magnetisation vector at an angular frequency ω_1 about an axis perpendicular to $\vec{B}_0$, which rotates itself at an angular frequency ω_0 about $\vec{B}_0$. This is the effect of applying an RF pulse to an isochromat. If the duration of the RF pulse is t, then the magnetisation will rotate by an angle $\Phi = \gamma B_1 t$. In a typical NMR experiment, a 90°-pulse is applied so that Φ is 90° and the magnetisation is flipped into the transverse plane (perpendicular to $\vec{B}_0$).

The movement of an isochromat in a sample consisting of many protons is not completely described by equation (2.4). An excited isochromat will not precess indefinitely at a fixed angle from the longitudinal direction but its magnetisation will gradually return to an equilibrium state with the magnetisation aligned along the main magnetic field. This relaxation is caused by a combination of processes. Some of the excitation energy will be spontaneously transferred to the environment as heat. This results in an exponential decay process known as the spin-lattice relaxation and characterized by the spin-lattice or longitudinal relaxation time T_1. Evolution of the z-component of the magnetisation is described by:

$$\frac{dM_z}{dt} = -\frac{M_z - M_0}{T_1},\qquad(2.5)$$

where M_0 is the initial magnetisation at the start $M(t = 0)$.

The spins however do not only exchange energy with the surrounding lattice, but also among themselves, which causes a variation in the precession rate between each other. This in turn results in dephasing of the spin states which is a faster process than the spin-lattice relaxation and is characterized by the spin-spin relaxation time, T_2. The evolution of the transverse magnetisation can be described by:

$$\frac{dM_{x,y}}{dt} = -\frac{M_{x,y}}{T_2}.\qquad(2.6)$$

Equations (2.5) and (2.6), when combined with the equation of motion (2.4), are collectively known as the Bloch equations for nuclear induction [6].

Solving the Bloch equations for a magnetisation vector after applying a 90°-pulse gives now:

$$
\begin{aligned}
M_x(t) &= M_0 \sin(\omega_0 t) e^{-\frac{t}{T_2}} \\
M_y(t) &= M_0 \cos(\omega_0 t) e^{-\frac{t}{T_2}} \\
M_z(t) &= M_0 \left[1 - e^{-\frac{t}{T_1}} \right].
\end{aligned}
$$

The transverse magnetisation components will describe an inward spiral movement with an exponentially decreasing radius $M_0 e^{-\frac{t}{T_2}}$ and with an angular frequency equal to the Larmor frequency at the static magnetic field $\vec{B}_0$.

Spin relaxation times

Different physical processes are responsible for the relaxation of the magnetisation $\vec{M}$ in the presence of a static magnetic field $\vec{B}_0$ [9]. The longitudinal relaxation time T_1 involves redistributing the populations of nuclear spin states in order to reach the thermal equilibrium distribution described by equation (2.2). The nuclear spins exchange energy with their surroundings, the lattice, by several interaction mechanisms. Hence, T_1-relaxation is also known as spin-lattice relaxation. T_1-relaxation rates are strongly dependent on the magnetic field strength B_0.

T_2-relaxation corresponds to a decoherence of the transverse magnetisation. Random fluctuations of the local magnetic field lead to random variations of the immediate Larmor frequencies of the different spins. As a result, the initial phase coherence of the spins is lost and the transverse magnetisation vanishes. T_2-relaxation is often called spin-spin relaxation because it involves only the phases of other spins. T_2-relaxation rates are less dependent on the field strength B_0 than T_1-relaxation rates. The T_1-relaxation rate of spins in a given sample is always slower than the T_2-relaxation rate.

If an electrically conducting coil is placed around the subject in the transverse plane, the rotating transverse magnetisation component will induce a voltage in the coil whose amplitude decays exponentially due to relaxation. This phenomenon, known as the free induction decay (FID), forms the signal for an NMR experiment and is illustrated in figure 2.3. It should be noted that in a sample, there are microscopic magnetic field inhomogeneities in each imaging voxel, which contains many isochromats. As a result, the relaxation decay
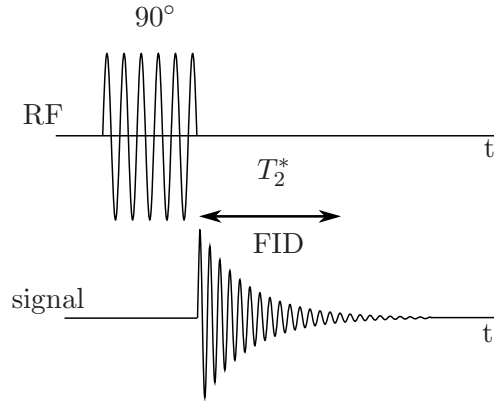
Figure 2.3: A 90°-pulse induces a free induction decay (FID) signal.

after a 90°-pulse will actually be faster than by T_2 relaxation only. The corresponding relaxation time is T_2^*.

In the next chapters, porous media are described consisting of an impermeable matrix filled with an MR-visible solvent. The observed T_2-relaxation time of the solvent molecules in a porous medium may be shorter in comparison to solvent molecules in bulk due to *surface relaxation* [10]. At the surface interface, a rapid exchange takes place between solvent molecules constrained or bound to the interface with a short T_2-relaxation time and free solvent molecules in the bulk with a longer time. Although there are solvent molecules with different relaxation times in the system, a single exponential magnetisation decay is observed described by a dynamically averaged T_2-relaxation rate. The higher the interaction between the interface and the solvent, the shorter the observed T_2-relaxation rate. The effect of surface relaxation on the T_2-relaxation rate and diffusion is studied in more detail in this work and described in chapter 3 and chapter 4 respectively.

Spin Echo

The relaxation times T_1 and T_2, together with the proton density, are very important in MRI, as they have the greatest effect in determining contrast. T_1 and T_2 are not invariant throughout the brain [11]. Moreover, there are systematic differences in these parameters between healthy and pathological tissue. It is thus advisable from a clinical point of view to acquire MR-images with a contrast depending on these relaxation parameters. In NMR and MRI, this contrast
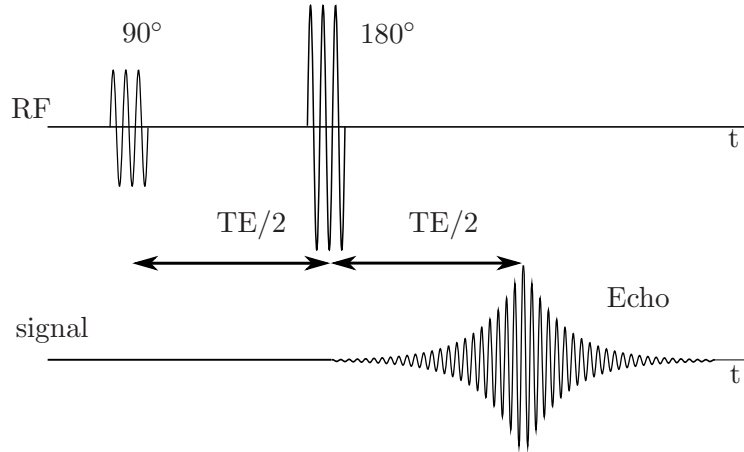
Figure 2.4: A spin-echo sequence uses a 90° -pulse and a 180° -pulse to form an echo.

is obtained by the design of pulse sequences consisting of a repetitive train of RF-pulses.

A pulse sequence for weighting the signal by the T_2-value, known as the spin-echo [12], consists of a pulse inducing a flip angle of 90°, followed after a time $TE/2$ by 180°-pulse. A schematic overview of a spin-echo is presented in figure 2.4. By the 90°-pulse, the spins are flipped in the transverse plane and start to dephase for a time $TE/2$, after which the magnetisation is flipped by the 180°-pulse. The spins are now rephasing and get in phase with one another after another time period of $TE/2$ and produce a measurable signal S at the echo time, TE, according to:

$$M_{xy}(TE) = M_0 e^{-\frac{TE}{T_2}} . \tag{2.7}$$

The T_2 constant can be determined by use of a multiple spin-echo sequence, in which the 180°-pulse is repeated for several TE-values. The repetition time TR between successive 90°-pulses is taken long enough so that the longitudinal magnetisation can recover fully. In this way, the effect of T_1 is eliminated and M_0 depends only on the number of protons.

2.2.3   Image formation

Gradient encoding and the Fourier transformation

In order to make the move from NMR to MRI, spatial encoding of
the NMR signal is required. Spatial information can be encoded
in the signal by applying magnetic field imaging gradients $\vec{G}$. A
magnetic field gradient is in fact a spatially dependent magnetic field
and is superimposed on the constant static magnetic field $\vec{B}_0$ (as
illustrated in figure 2.5). The magnitude of these gradients is small
in comparison to that of the static field $\vec{B}_0$ but they are large enough
to induce variations in the angular Larmor frequency at which the
local magnetisation vectors precess. A gradient with magnitude and
orientation described by a vector $\vec{G}$ will produce a local frequency
shift, relative to the Larmor frequency, described by

$$\Delta\omega(\vec{r}) = \omega(\vec{r}) - \omega_L = \gamma\vec{G}.\vec{r} = \gamma(G_x r_x + G_y r_y + G_z r_z), \qquad (2.8)$$

where $\vec{r} = (r_x, r_y, r_z)$ represents the location in the brain.

Hence, by applying magnetic gradients, the angular frequency
at which the local magnetisation vectors precess becomes spatially
dependent, which means they are all encoded by a specific frequency
and phase determined by the local field strength. The phase of a
local magnetisation vector by a gradient $\vec{G}$ can be characterized by

$$\vec{k} = \frac{1}{2\pi}\gamma\int_0^\tau \vec{G}(t)dt. \qquad (2.9)$$

It is assumed that the magnetisation vector is determined only
by the number of protons. The total signal S of the whole object is
then given by:

$$S(\vec{k}) = \int_V \rho(\vec{r})e^{i2\pi\vec{k}.\vec{r}}d\vec{r}, \qquad (2.10)$$

where the scalar field $\rho(\vec{r})$ represents the proton density, i.e. the num-
ber of spins per unit volume at each location of the brain. The proton
density is proportional to the initial magnetisation $\vec{M}$ as we saw in
equation (2.3). Equation (2.10) describes a Fourier relationship be-
tween the proton density and the measured signal in the presence
of the magnetic field gradients. This is a fundamental relationship
in MRI. When the signal is sampled at a number of locations in $\vec{k}$-
space, we can recover the local proton density using a discrete Fourier
transform (DFT). In more general terms, the local signal M not only
depend on the proton density, but also on the T_1- and T_2-relaxation
times. The principle of MRI is illustrated in figure 2.5.
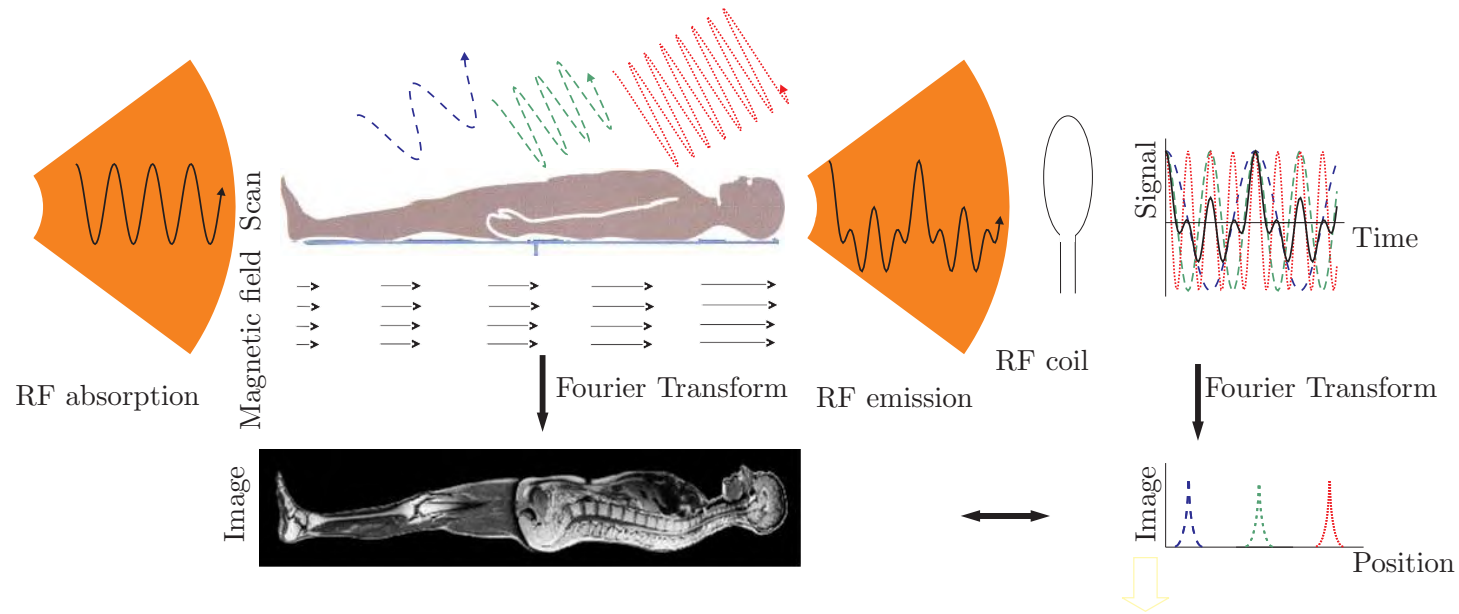
Figure 2.5: *Illustration of the working of MRI. After excitation of the subject, a magnetic gradient field is applied by which the angular frequency of the spins become spatially dependent. The detected RF signal emitted from the subject consist of several frequencies and can be converted by a Fourier transform into an image. This is illustrated in one dimension at the right side of the figure. To obtain a 2D (3D) image, magnetic gradients are applied in 2 (3) orthogonal directions.*
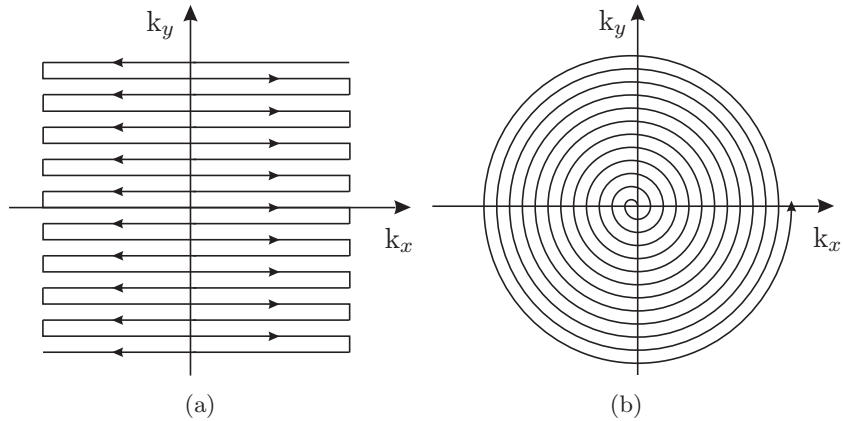
Figure 2.6: (a) Cartesian sampling scheme. (b) Spiral sampling scheme.

Trajectory design

A $\vec{k}$-space trajectory is outlined by applying a time-dependent magnetic gradient $\vec{G}(t)$, defined by the derivative of equation (2.9):

$$\vec{G}(t) = \frac{2\pi}{\gamma}\frac{d\vec{k}(t)}{dt}.\tag{2.11}$$

There are many possible schemes for traversing $\vec{k}$-space, each scheme having its own advantages and disadvantages. For diffusion imaging, fast sequences are required to reduce scan time and eliminate motion artefacts. Two fast sampling schemes used in diffusion imaging are presented in figure 2.6.

The standard fast imaging technique is diffusion enhanced echo-planar imaging (EPI), by which the k-space is sampled in a meandering trajectory (see figure 2.6(a)) [8]. EPI is widely available and has a relative easy reconstruction algorithm (DFT). On the other hand, imperfections in the hardware and eddy currents may cause image artefacts.

As an alternative, a spiral scanning scheme is proposed as one of the most efficient sampling schemes (see figure 2.6(b)) [13]. The very smooth trajectory of a spiral sequence does not place such high demands on the hardware of an MR-scanner. Moreover, spiral sequences are relatively insensitive to motion artefacts because of the gradient nulling property [4] of the time integral of the measured signal.

2.2.4   Image artefacts

Artefacts in NMR consist of deviations in an image containing erroneous information. MR images are vulnerable for several kinds of artefacts. We describe here the three most significant artefacts for diffusion MRI.

Most subjects (except phantoms) may move during the MR-scan. For brain imaging, even in the case of no bulk motion, there will be still localised movement present due to eye motion, swallowing and dilation and contraction of the carotid arteries. The ventricles, which are full of fluid, exhibit pulsatile movement. Motion during the MR-scan causes inconsistencies in the read-out data, resulting in image blurring and ghosting. Ghosting is the appearance of signal not corresponding to the scanned object. By using a sequence that acquires the images very quickly, motion artefacts can be significantly reduced. Single shot sequences such as Cartesian and spiral EPI that sample the $\vec{k}$-space at once are therefore most often used in diffusion MRI. Besides this, gating, where each slice is collected at the same point in the cardiac cycle, is also advisable [14].

Whereas EPI is less sensitive to motion in comparison to standard SE sequences, it is considerably more sensitive to artefacts due to eddy currents and susceptibility effects. Both artefacts are described here shortly.

Eddy currents are caused by high magnetic fields that switch rapidly in time. According to Lenz's law, electric current loops will be induced that counteract the applied magnetic field. Eddy currents bias the phase encoding in $\vec{k}$-space and result in magnification, translation, and shearing of the image. A method to significantly reduce this effect is by using a twice-refocused spin echo (TRSE) sequence, which is discussed further (section 2.4.1).

Strong susceptibility related artefacts may appear in the brain at transitions between regions with different magnetic susceptibility such as air and soft tissue. At those boundaries, the magnetic field is locally distorted and inhomogeneous. Signals coming from a voxel in an inhomogeneous region will be considered to originate from another spatial position resulting in signal drop-out in some areas and piling up in others. An example of susceptibility artefacts in a diffusion image is shown in figure 2.7, where a significant signal drop-out in the regions near the sinuses can be seen. Severe susceptibility artefacts can also be noticed when the subject contains small pieces of metal near the head such as a brace or glasses.

(a)   (b)

(c)
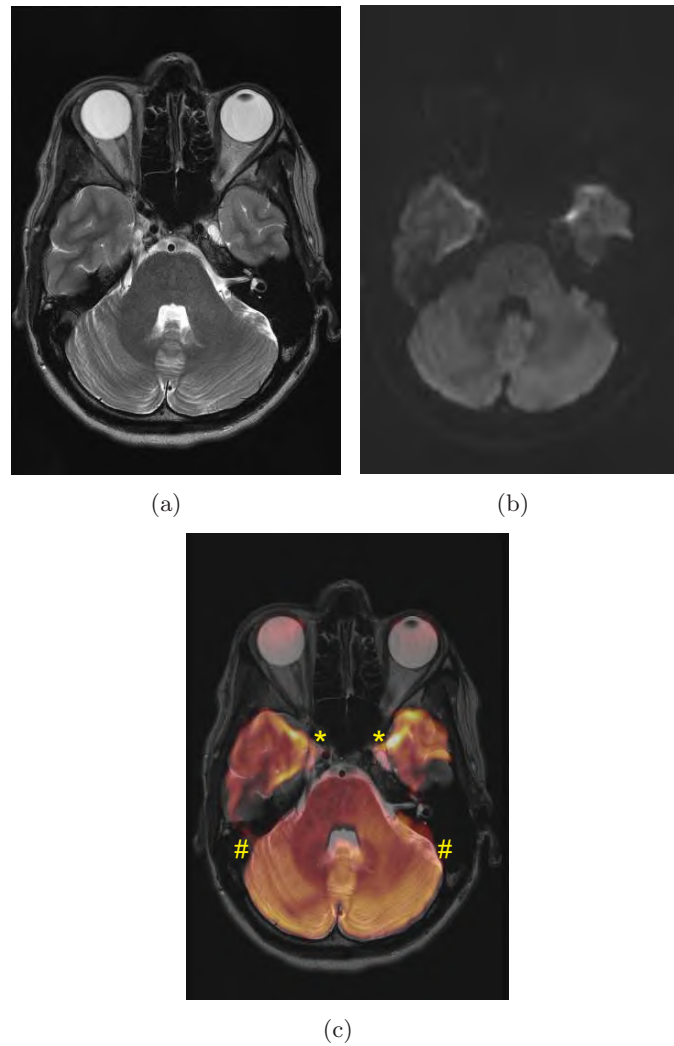
Figure 2.7: Example of a susceptibility related artefact: (a) T_2 SE image as a reference. (b) Diffusion MR image. (c) The T_2-image of (a) with the diffusion image of (b) as overlay. The diffusion image is colour encoded ranging from red to yellow according to increased signal intensity. Artefacts are noticed around the sphenoid sinus (indicated by a *-sign) and petrous bone (indicated by a #-sign). There is considerable signal drop out in the anterior medial temporal lobes and the anterior temporal pole. Signal pile up is evident at the edges of the artefacts (abnormal higher signal intensity).

Figure 2.8: Illustration of a single realization of Brownian motion.

2.3   The diffusion process

2.3.1   Self diffusion of water molecules

Brownian motion

Water molecules at a temperature greater than absolute zero (0K) are in constant motion and collide with one another. The greater the kinetic energy, the faster the movement. With each collision, a water molecule experiences a random displacement. As a result, a group of molecules that start at the same location will be spread out over time. This random motion also leads to microscopic motion of suspended particles and was observed by Brown in 1828 for grains of pollen in water and is referred to as "Brownian motion" [15]. A theory that explained the observations by Brown was developed by Einstein in 1905 [16] who presented the theory as an indirect confirmation of the existence of molecules. An illustration of the Brownian motion is shown in figure 2.8.

Molecular self-diffusion can be described as a random walk of molecules with a very complex distribution of step sizes and directions on a molecular scale. In case of isotropic diffusion in a homogeneous medium, the different steps are independent. Following the central limit theorem, the distribution of distances travelled by the molecules after many elementary steps is Gaussian. For a one-dimensional system whose properties depend on a coordinate x, the probability that a given molecule has travelled from x_0 over a distance x during a
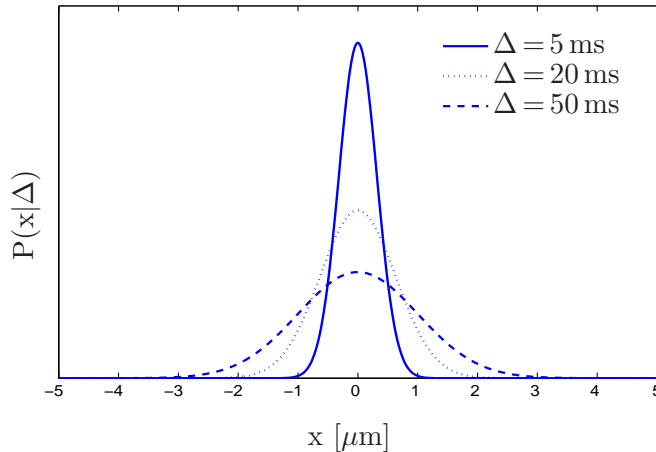
Figure 2.9: Probability density function for increasing diffusion times in case of one-dimensional diffusion. D was taken 10^{-9} m^2/s, which is similar to the mean diffusion coefficient in brain white matter.

time period Δ is given by

$$P(x|x_0, \Delta) = \frac{1}{\sqrt{4\pi D\Delta}} e^{-\frac{(x-x_0)^2}{4\pi D\Delta}}, \tag{2.12}$$

where D is the diffusion coefficient. Figure 2.9 illustrates the evolution of the probability displacement function $P(x|x_0, \Delta)$ for increasing diffusion time Δ. This function, also called the probability displacement function (PDF), is a Gaussian function with a mean value of x_0 and a variance proportional to the time:

$$\sigma^2 = \left\langle (x-x_0)^2 \right\rangle = 2D\Delta. \tag{2.13}$$

The proportionality constant defines the diffusion coefficient D. The general case is given by the well-known Einstein equation:

$$r_{rms}^2 = \left\langle (\vec{r} - \vec{r}_0)^2 \right\rangle = 2n_d D\Delta, \tag{2.14}$$

with n_d the spatial dimension.

Restricted diffusion

The diffusion of water molecules in heterogeneous media is in general not isotropic. This is illustrated in figure 2.10 for particles diffusion
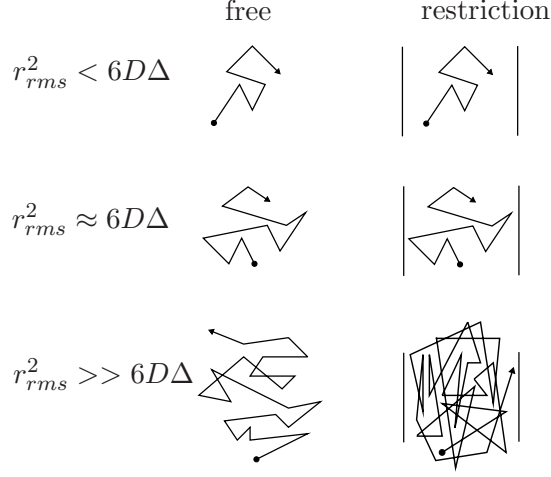
Figure 2.10: Illustration of restricted diffusion. Depending on the diffusion time Δ, particles will sense restriction and the diffusion becomes more preferable in one direction than another.

in the presence of two walls. For short diffusion times, most particles will not sense restriction and can still diffuse freely. For increasing diffusion time however, particles encounter the wall and the diffusion gets more restricted in one direction than another. The diffusion becomes time and direction dependent or anisotropic. The time-dependency of the diffusion coefficient is elaborated in detail further in this work (see section 4.2).

Diffusion anisotropy

When assuming that the particles satisfy a Gaussian displacement distribution, Einstein's equation (2.14) can be generalized to allow for directional dependency. The Gaussian displacement distribution at time Δ can then be described by a covariance matrix:

$$\mathbf{D} = \frac{1}{6\Delta}\langle(\vec{r} - \vec{r}_0).(\vec{r} - \vec{r}_0)^T\rangle = \begin{bmatrix} D_{xx} & D_{xy} & D_{xz} \\ D_{xy} & D_{yy} & D_{yz} \\ D_{xz} & D_{yz} & D_{zz} \end{bmatrix}. \qquad (2.15)$$

A covariance matrix is positive definite and symmetric. The diffusion coefficients spanning up the matrix $\mathbf{D}$ are the components of a three-dimensional diffusion tensor, relative to the chosen orthonormal basis set, $(\vec{u}_x, \vec{u}_y, \vec{u}_z)$. The special case of isotropic diffusion corresponds
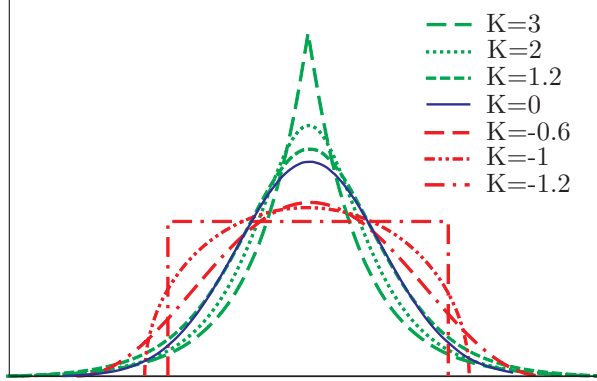
Figure 2.11: The kurtosis is a measure of the sharpness of a function and is demonstrated here for functions with varying kurtosis values. The plain curve represents a Gaussian curve, the dotted curves are leptokurtic (K>0) or platykurtic (K<0).

then with:

$$D_{xx} = D_{yy} = D_{zz} = D \quad D_{xy} = D_{xz} = D_{yz} = 0.$$

Diffusion kurtosis

In case of restricted diffusion, the diffusion profile is in general not characterized any more by a Gaussian displacement profile. The excess diffusion kurtosis K is a metric which quantifies the deviation from a Gaussian PDF and is defined by:

$$K = \frac{\left\langle (\vec{r} - \vec{r}_0)^4 \right\rangle}{\left\langle (\vec{r} - \vec{r}_0)^2 \right\rangle^2} - 3. \tag{2.16}$$

The excess diffusion kurtosis, also called "diffusion kurtosis", is a measure for the sharpness or pointedness of the PDF as illustrated in figure 2.11. A Gaussian PDF has a zero kurtosis and is called mesokurtic. A PDF with positive kurtosis is called leptokurtic. This distribution has a more acute peak and fat tails, meaning that the probabilities of values near the centre or extreme values are higher than in comparison to a Gaussian distribution. A PDF with negative kurtosis is platykurtic. This distribution has a more rounded peak and wider shoulders meaning that there is a lower probability than a
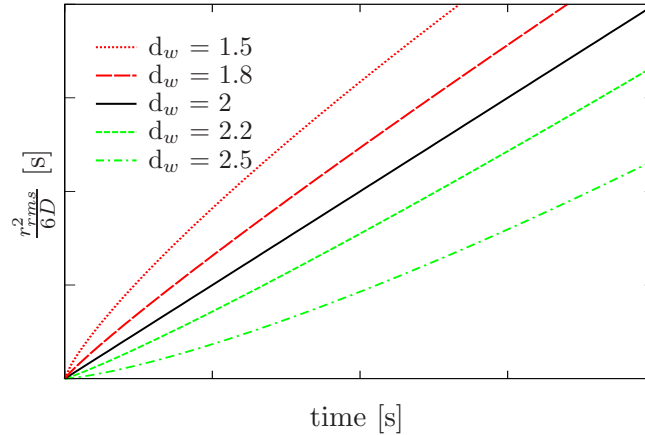
Figure 2.12: Illustration of anomalous diffusion. The plain curve represents normal diffusion when r^2_{rms} is linearly proportional to the time and d_w in equation (2.17) equals 2. The dotted curves show anomalous diffusion ($d_w \neq 2$): subdiffusion appears when $d_w > 2$, superdiffusion appears when $d_w < 2$.

Gaussian distribution for values near the centre or for extreme values. Distributions over a confined interval are always platykurtic.

Anomalous diffusion

In normal diffusion, the mean-square displacement r^2_{rms} of a diffusing particle is linearly proportional to the time as given by the Einstein equation (2.14). However, in disordered media and systems exhibiting fractal behaviour, the diffusion is anomalous. In that case, r^2_{rms} is proportional to a fractional power of time less than one,

$$r^2_{rms} \propto \Delta^{2/d_w}, \tag{2.17}$$

where d_w is the walk (or path or trail) dimension [17], also called the anomalous diffusion coefficient [18]. Normal diffusion appears if $d_w = 2$, whereas in the case when $d_w > 2$, the distances travelled by the diffusing particles have a slower-than-linear time dependence. This kind of a process is called subdiffusion. The opposite case ($d_w < 2$) corresponds to a faster-than-normal diffusion which is called superdiffusion. Anomalous diffusion is illustrated in figure 2.12. Various systems that give rise to these different behaviours are described in [19]. The theory of anomalous diffusion is used in section 4.2 to describe the time-dependency of the diffusion process.
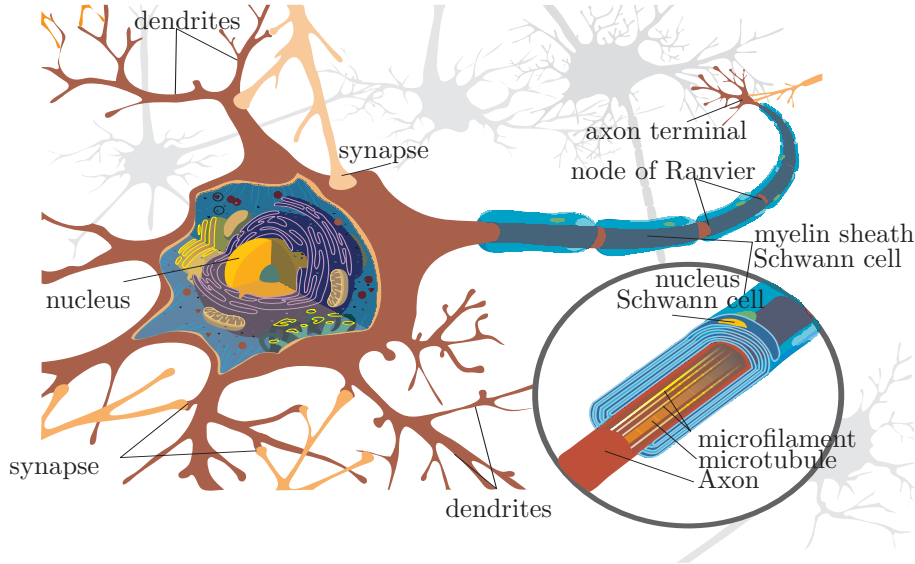
Figure 2.13: The structure of a neuron.

2.3.2   Diffusion in brain white matter

Fibre architecture of the brain white matter

The human nerve system is composed of billions of neurons, which are electrically excitable cells that process and transmit information. The structure of a neuron is shown in figure 2.13: it consists of a cell body or soma, a dentritic tree, and an axon. The dendrites receive input from other neurons at the synapse. The axons are in fact the transmission lines of the neural signal.

Axons transmit the impulses received at the dendrites and cell body away and can extend many times the soma in length. They consist of microtubuli and microfilaments and are wrapped by sheaths of fatty myelinated Schwann cells in the peripheral nerve system (PNS) (see figure 2.13) and oligodendrocytes in the central nerve system (CNS) [20]. These myelin sheaths serve as the insulator for the proper transmission of the electrical impulses along the axon. When myelin degrades, conduction of signals along the nerve can be impaired or lost. This is the case with certain neurodegenerative disorders such as multiple sclerosis (MS).

An example of a myelinated axon is shown in figure 2.14. The axon diameter in the CNS is typically about 1 μm but can increase up to 10 μm depending on the degree of myelinization [21].
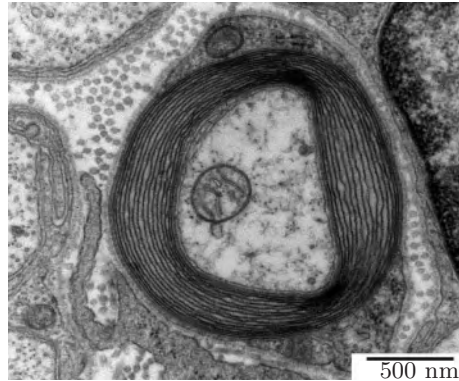
Figure 2.14: A myelinated axon.

Axons for their part are bundled together in fibre tracts or fasciculi. The human brain is organized in such a way that the cell body and dendrites are mainly situated at the cerebral cortex, which is the curved surface of the brain. Axonal bundles form the connections between the different functional regions in the cortex. The white matter of the brain is formed by those myelinated fibre bundles, that produce a high intensity in T_1-weighted MR images. Figure 2.15 shows dissected white matter of the brain. Several fibre bundle directions can be distinguished: fibres connecting the frontal part with the lateral part, connections between the left and right hemisphere (the *corpus callosum*) and fibre tracts starting from the basis pedunculi and fanning out to the outer parts of the cerebral cortex (*corona radiata*). The corpus callosum is also indicated on a coronal T_1-weighted MR image of the brain (see figure 2.16).

Macro structure of the brain

Figure 2.16 shows a coronal T_1-weighted MR image of the brain on which the WM and grey matter (GM) are indicated. The brain cortex is known as GM. Besides the GM and WM, there are also cavities in the inner part of the brain filled with cerebrospinal fluid (CSF), the ventricles. CSF and also the cortex, consisting of randomly oriented dendrites, both exhibit isotropic diffusion behaviour [22], whereas the diffusion in WM shows to be anisotropic. In this study, we will mainly focus on diffusion in the WM. Figure 2.17 shows a schematic image and photograph of the brain where the main anatomic regions such as the *corpus callosum* are indicated.

Figure 2.15: Dissected white matter. The nerve fibres are clearly visible and run in several directions.
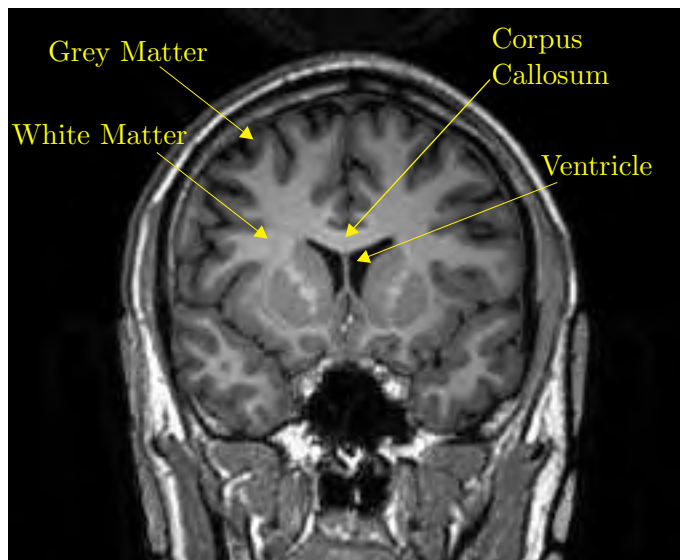
Figure 2.16: T_1-weighted MR image of a coronal section through the brain. grey matter and white matter are indicated, as well as the ventricles. The corpus callosum forms the bridge between the right and left hemisphere.
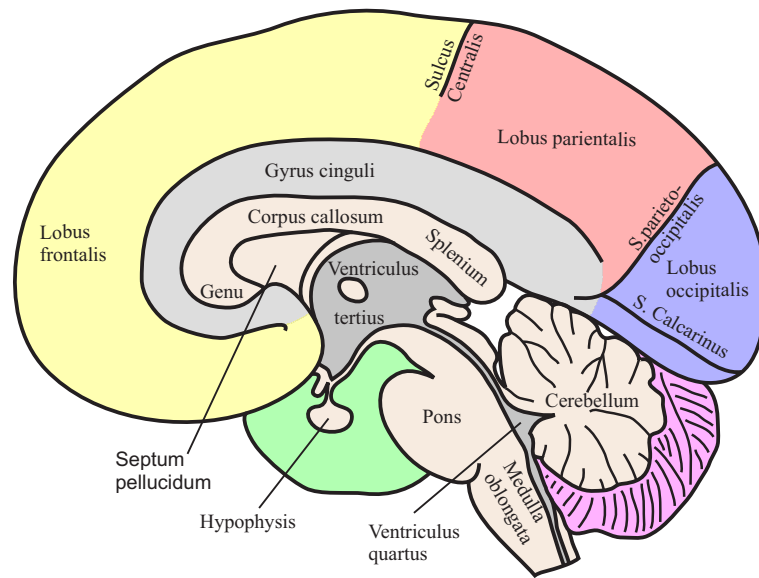
(a)
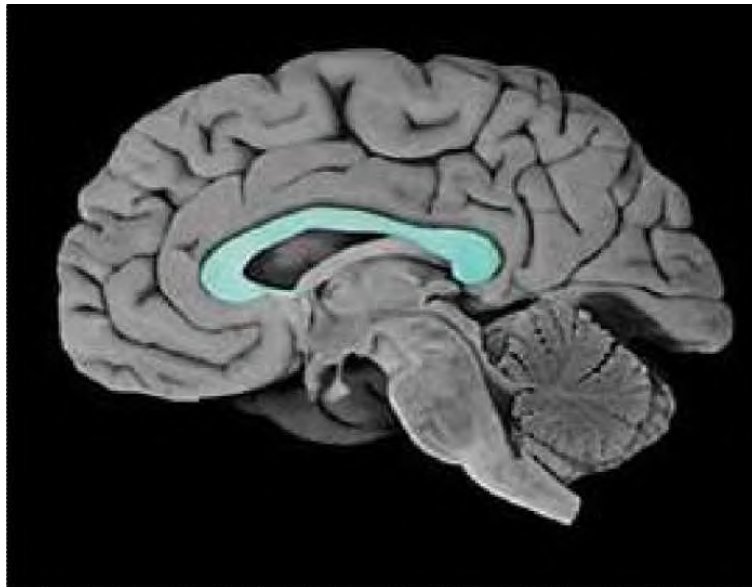
(b)

Figure 2.17: (a) Schematic image of a midsagittal section of the right hemisphere of the human brain showing the anatomy in Latin. (b) Corresponding photographic image.
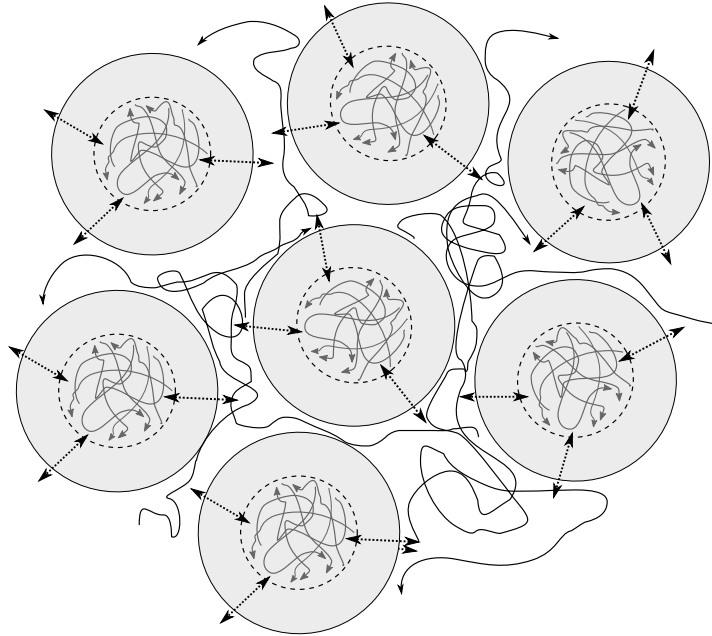
Figure 2.18: Illustration of the three contributions to the diffusion signal in WM: intracellular diffusion, extracellular diffusion and exchange between intracellular and extracellular space.

Origin of the diffusion signal in WM

The diffusion signal observed in WM is highly anisotropic [23–26]. The diffusivity measured in the longitudinal direction along the axons is up to five times higher than the diffusivity measured in the transverse direction [27]. The exact micro structural features that underlie the measured anisotropy remained matter of debate until now. Postulated sources of anisotropy include both intracellular and extracellular structures: axonal membranes, myelin sheaths and microtubules [28].

The axons in the WM are very densely packed. The measured volume fractions for the intra- and extracellular fractions are about 0.8 and 0.2 [29]. Studies performed by Beaulieu [27] suggest that anisotropic water diffusion in neural fibres is mainly due to the dense packing of axons and their inherent axonal membranes that hinder the diffusion water diffusion significantly perpendicular to the axis of the fibres relative to the preferential parallel direction. The presence of a myelin sheath surrounding the axons may enhance the anisotropy

in the order of 30%.

The three components contributing to the diffusion process inside the WM are illustrated in figure 2.18. On the one hand, intracellular water molecules may be restricted inside closed spaces such as inside the axons of the WM. On the other hand, water molecules in the extracellular parts might also contribute to the anisotropy effect. Exchange between the intra- and extracellular part may change the diffusion profile as well.

The apparent diffusion coefficient (ADC) in brain white matter as measured with MR ranges between 0.35×10^{-3} mm^2/s and 1.2×10^{-3} mm^2/s [24] which is three to ten times smaller than the diffusion coefficient of free water at 37° (which is 3.28×10^{-3} mm^2/s [30]).

The diffusion in the intracellular space has been assumed to be restricted, meaning that for long diffusion times, the diffusion coefficient becomes zero. Restriction of real intra-axonal metabolites, such as N-acetylasparate, has been observed [31] but not for water molecules in brain white matter.

The diffusion in the extracellular space is considered to be hindered because the fibres form obstacles for the water molecules they have to travel around (see figure 2.18). For long diffusion times, the water displacement profile will become Gaussian and can be characterized by a tortuosity (described further in chapter 4). The tortuosity has been measured in the extracellular space with ionophoretic point sources [32], but not yet for water molecules.

The overall low diffusivity of water in cells could not be fully explained by restriction and compartmentization effects in combination with hindered diffusion, and the exact role of the white matter structures involved (water fractions, membranes, myelin, etc...) is still elusive [33]. The correct assignment of water diffusion patterns to the underlying tissue micro structure remains thus a challenging task.

2.4   Diffusion magnetic resonance imaging

2.4.1   Diffusion weighted sequences

General Theory

The effect of diffusion on the NMR signal was first noticed by Hahn in 1950 [12], Carr and Purcell in 1954 [34], and Woessner in 1961 [35,36]. Torrey presented a generalized version of the Bloch equations in 1956 which incorporated elements of molecular diffusion:

$$\frac{d\vec{M}}{dt} = \gamma \vec{M} \times \vec{B}_0 + \begin{pmatrix} \frac{M_x}{T_2} \\ \frac{M_y}{T_2} \\ \frac{M_0 - M_z}{T_1} \end{pmatrix} + D\nabla^2 \vec{M}. \qquad (2.18)$$

While the first two terms of equation (2.18) come from the original Bloch equation as described in section 2.2.2, the third term accounting for molecular diffusion was added by Torrey. The complete equation (2.18) is called the Bloch-Torrey equation. The solution for magnetization in the transverse plane M_{xy} in a spin echo experiment after a 180°-pulse at time TE is given by:

$$M_{xy} = M_0 e^{-\frac{TE}{T_2}} e^{-bD}. \qquad (2.19)$$

This is the solution for a spin-echo sequence (equation (2.7)) multiplied with an extra attenuation factor e^{-bD} where b, given by:

$$b = \gamma^2 \int_0^{TE} \left(\int_0^t G(t')dt' \right)^2 dt, \qquad (2.20)$$

describes the diffusion sensitizing gradient amplitudes and timing.

Stejskal-Tanner sequence

While all MRI pulse sequences are to some extent sensitive to molecular motion and diffusion, the specific use of balanced bipolar gradients for the measurement of diffusion was developed by Stejskal and Tanner [37]. Starting from a standard spin-echo sequence as described in section 2.2.2, a symmetric pair of diffusion weighted gradients is added to either side of the refocussing 180° pulse as shown in figure 2.19. The first of these gradients will offset the phase of the spins by an amount that depends on their location, and the second will provide equal and opposite (due to the 180°-pulse) rephasing *if* the

spins have not moved during the diffusion time Δ, which is the time between the application of the two gradients. As the spins move randomly due to diffusion, the isochromats will dephase. The further the spins have diffused during the diffusion time Δ, the less perfect the rephasing and the smaller the amplitude of the final signal will be. More diffusion is thus indicated by a more attenuated signal. It should be noted here that the measured attenuation due to motion differs from the effect of coherent motion or flow because the latter will produce a phase shift in the spin isochromats without attenuating the signal as random motion does [38].

The diffusion coefficient along the direction of the applied diffusion gradients can be measured by comparing the MRI signal with and without diffusion-weighting gradients:

$$S(b) = M_0 e^{-\frac{t}{T_2}} e^{-bD} \tag{2.21}$$

$$S(0) = M_0 e^{-\frac{t}{T_2}} \tag{2.22}$$

$$\ln\left(\frac{S(b)}{S(0)}\right) = -bD, \tag{2.23}$$

where b can be calculated using (2.20):

$$b = \gamma^2 \delta^2 (\Delta - \frac{\delta}{3}) G^2. \tag{2.24}$$

The b-factor incorporates the relevant characteristics of the diffusion gradients, i.e. the gradient amplitude G, the duration δ and the (diffusion) time-interval Δ between the two diffusion gradients. The b-factor is also known as the diffusion weighting factor.

The relation between signal attenuation and the diffusion coefficient as derived by Stejskal and Tanner (2.23) makes the assumption that the diffusion has a Gaussian diffusion profile. This equation is only valid under the assumption that $\delta << \Delta$ such that the effect of diffusion during the application of the diffusion gradients is negligible [39]. Also, it is assumed that dephasing due to the application of imaging gradients can be neglected.

Other pulsed field gradient sequences

Instead of one unipolar gradient set in combination with a single refocussing RF pulse, as proposed by Stejskal and Tanner, many SE diffusion sequence variants can be created using multiple refocussing
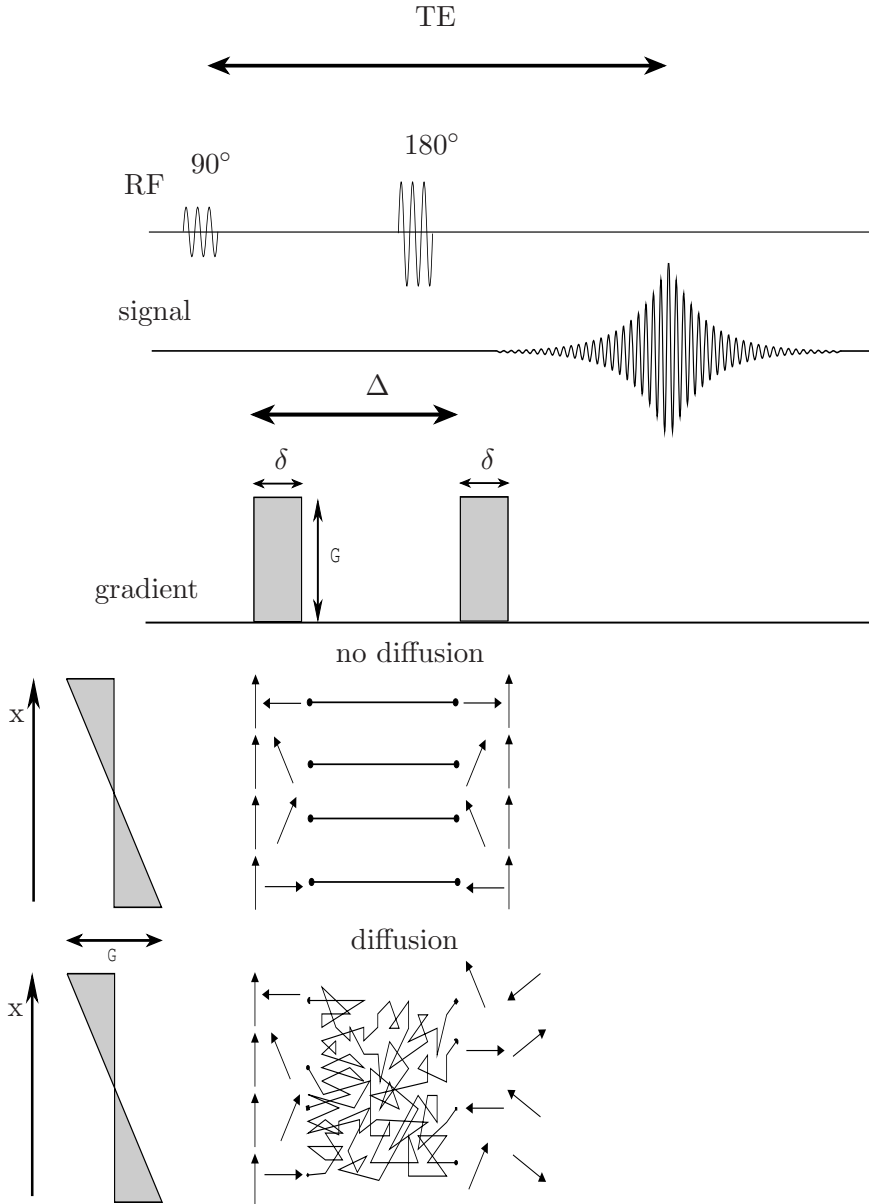
*Figure 2.19: Pulse sequence diagram for a diffusion-weighted spin-echo sequence. Two diffusion gradients are applied at each side of the 180°-pulse during a time δ. The first diffusion gradient causes a position dependent dephasing of the spins. In case of no motion, the second gradient will rephase the spins, while in case of diffusion, the rephasing will not be complete resulting in signal attenuation.*

pulses and several sets of bipolar gradients. The general term for this type of sequences is pulsed field gradient spin echo (PFGSE).

Using more than one refocussing pulse permits variable intervals between the pulses, requiring only that the dephasing and rephasing times sum up equally at the time of the echo. The *twice-refocused spin echo (TRSE)* sequence [40] utilizes this freedom to reduce the effect of eddy currents at the read-out. The diffusion gradients in diffusion sequences typically push the hardware of the MR-scanner to the limit, resulting in eddy currents and image distortion artefacts (as shown in section 2.2.4). The Stejskal-Tanner sequence is extended with an extra 180°-pulse and an extra set of bipolar gradients (see figure 2.20(a)). By adjusting the timings of the diffusion gradients, the eddy currents with a single exponential decay constant can be nulled, and eddy currents with similar decay constants can be greatly reduced. The TRSE sequence is often used to perform diffusion imaging in clinical settings and is used in this work for all measurements on clinical MR scanners.

In materials science, several pulsed field gradient (PFG) sequences are proposed to reduce the effect of internal gradients caused by local differences in magnetic susceptibility. The local differences in magnetic susceptibility produce field inhomogeneities and bias the diffusion experiment since additional dephasing is caused by magnetic field inhomogeneity (illustrated in 2.2.4). An overview of sequences to filter out the effect of internal gradients is presented in [41].

A PFGSE-sequence is only applicable if the diffusion time $\Delta \leq T_2$, otherwise the signal attenuation is dominated by transverse relaxation (see equation (2.19)). The *PFG stimulated echo (STE)* (figure 2.20(b)) is proposed in order to measure the diffusion for long diffusion times [42]. In this sequence, the 90°- and 180°-pulse of the Stejskal-Tanner sequence are replaced by three 90°-pulses. The first echo appears after the second 90°-pulse, with an amplitude of only half that of a spin echo of a PFGSE sequence. The other half of the magnetisation is flipped in the longitudinal direction and undergoes T_1-relaxation during τ. The third 90°-pulse flips the magnetisation again in the transverse plane and produces a diffusion weighted stimulated spin-echo. As this echo is mainly dominated by T_1-decay and T_1 is larger than T_2, this sequence is the most suitable for measuring diffusion at long diffusion times.
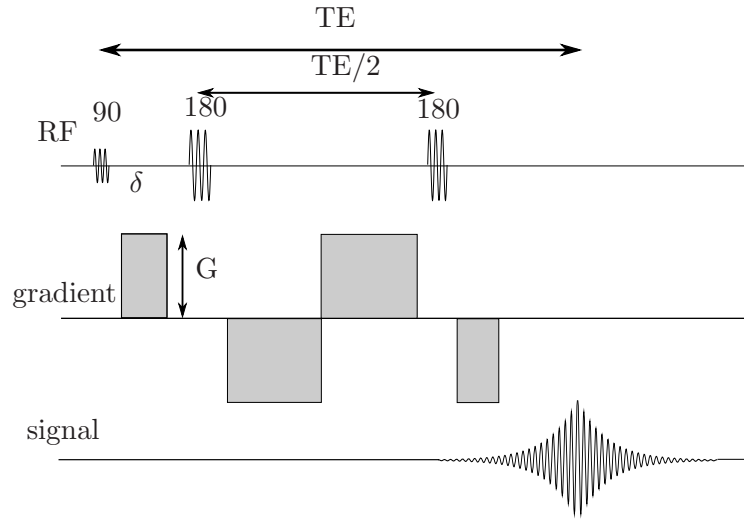
(a) TRSE
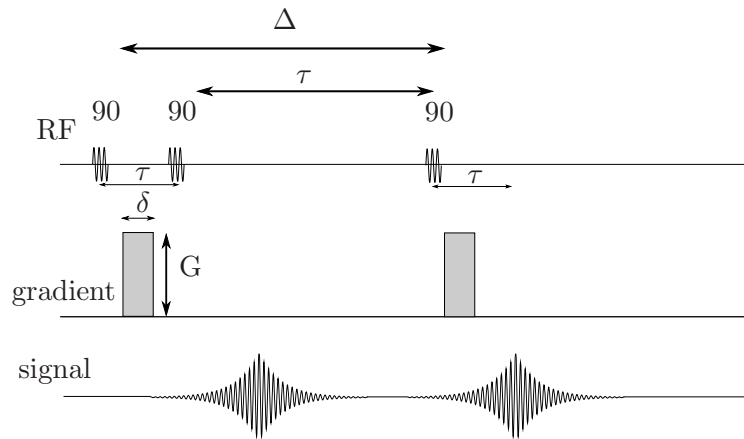
(b) STE

Figure 2.20: Sequence diagrams of PFG sequences. (a) A twice refocused spin echo (TRSE) sequence to reduce the effect of eddy currents at read-out time. (b) A stimulated echo sequence (STE) to measure the diffusion at long diffusion times.
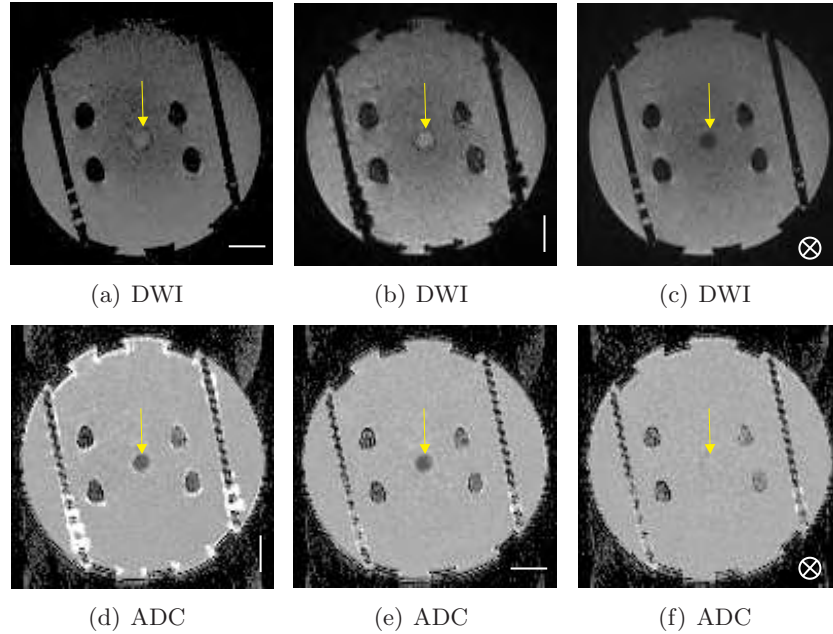
Figure 2.21: *Diffusion weighted images (DWI's) (a,b,c) and corresponding apparent diffusion coefficient (ADC) maps (d,e,f) of a fibre bundle phantom oriented in the in-plane direction. The fibre bundle is indicated by an arrow and the direction of the applied gradient is shown at the right bottom of each subfigure.*

2.4.2   Diffusion tensor imaging

Diffusion weighted images and ADC maps

The diffusion coefficient can be measured in a given direction by two measurements according to equation (2.23), one with diffusion weighting and one without diffusion weighting. However, the diffusion coefficient measured in biological tissue will depend on the direction, the diffusion time and gradient amplitude. It is thus more appropriate for biological applications to talk about the apparent diffusion coefficient (ADC) for a given direction and diffusion time and weighting. The ADC as a global parameter reflecting the diffusion properties of tissue was introduced by Le Bihan in 1986 [22].

Examples of diffusion weighted images (DWI's) and the corresponding ADC-maps of an anisotropic diffusion phantom directed in the in-plane direction are shown in figures 2.21(a-c) and figures

2.21(d-f) respectively for varying gradient directions. When the diffusion gradients are in the same direction as the fibre bundle, the diffusion is not restricted and the signal is more attenuated than when the gradients are perpendicular to the fibre direction where the diffusion is restricted. In contrast to a DWI, a higher signal intensity in an ADC-map denotes high diffusion and thus less restriction.

In vivo examples of DW images in white matter are shown in figure 2.23.

Diffusion tensor

Since biological tissue such as WM is anisotropic, the diffusion can not be described accurately by a single scalar. As shown in equation (2.15), the ADC can be generalized to an apparent diffusion tensor or diffusion tensor (DT). The extension of the principles described above to diffusion tensor imaging (DTI) was described by Basser in 1994 [43]. DW-MRI is preformed with diffusion gradients in different directions. For a gradient applied in a direction $\vec{v}_i$, equation (2.23) and equation (2.24) become now:

$$\ln\left(\frac{S_i(b)}{S(0)}\right) = -\gamma^2\delta^2(\Delta - \frac{\delta}{3})G^2\vec{v}_i^T\mathbf{D}\vec{v}_i = -b\vec{v}_i^T\mathbf{D}\vec{v}_i \qquad (2.25)$$

Usually the magnitude of the diffusion gradients in a diffusion weighted sequence are chosen to be identical for all directions. If not, $G^2\vec{v}_i^T\mathbf{D}\vec{v}_i$ in equation (2.25) should be replaced by $\vec{G}_i^T\mathbf{D}\vec{G}_i$.

The ADC_i measured along the direction corresponding to $\vec{v}_i$ has the following relation to the diffusion tensor $\mathbf{D}$:

$$ADC_i = \vec{v}_i^T\mathbf{D}\vec{v}_i. \qquad (2.26)$$

To derive the complete diffusion tensor, DW-MRI should be performed in several directions $\vec{v}_i$. Equation (2.25) represents a system of linear equations that can be solved for the six independent components of the tensor $\mathbf{D}$ given values of $S(b)$ in at least six non-collinear directions in addition to the T_2-weighted signal $S(0)$. However, since the diffusion weighted (DW) images are noisy and may be distorted by eddy currents and motion, it is common in practice to perform DW-MRI in more than six different gradient directions and then fit the tensor statistically using multivariate linear regression [44, 45].

The diffusion tensor can be obtained in every voxel from a set of DW images. Once the apparent diffusion tensor $\mathbf{D}$ has been estimated, it is always possible to transform $\mathbf{D}$ for every voxel into
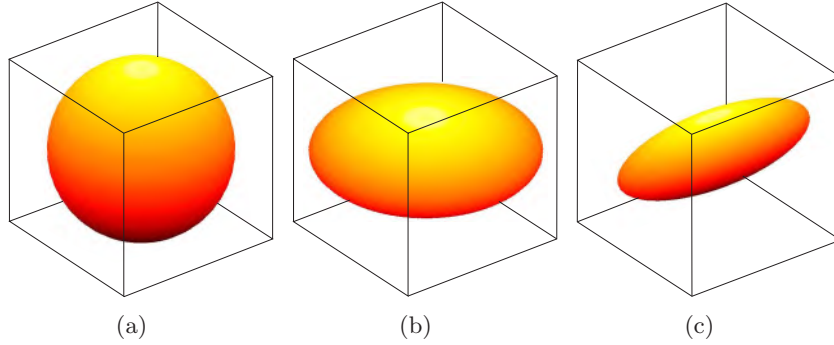
Figure 2.22: *Ellipsoids representing the diffusion tensor. (a) Isotropic (b) Oblate (c) Prolate diffusion profiles.*

another tensor **D'** with off-diagonal elements equal to zero and diagonal elements reflecting the intrinsic diffusion properties of the voxel, independent of the coordinate system in which they were measured. This can be achieved by diagonalisation of **D** as **D** is symmetric and positive definite which means it has real eigenvalues:

$$\mathbf{D} = \mathbf{E}\mathbf{\Lambda}\mathbf{E}^{-1}, \tag{2.27}$$

where

$$\mathbf{E} = \begin{bmatrix} \vec{e}_1 & \vec{e}_2 & \vec{e}_3 \end{bmatrix} \quad \text{and} \quad \mathbf{\Lambda} = \begin{bmatrix} \lambda_1 & 0 & 0 \\ 0 & \lambda_2 & 0 \\ 0 & 0 & \lambda_3 \end{bmatrix}. \tag{2.28}$$

$\vec{e}_1$, $\vec{e}_2$, $\vec{e}_3$ are the three eigenvectors of **D**, which are orthonormal vectors representing three unique directions along which the molecular displacement are uncorrelated. λ_1, λ_2 and λ_3 are the corresponding ADC values or the eigenvalues of **D**. For each DT, the combination of eigenvectors and eigenvalues is unique and reflects the microscopic diffusion properties of the sample under investigation [11]. The coordinate system of the eigenvectors ($\vec{e}_1$, $\vec{e}_2$, $\vec{e}_3$) is chosen by convention such that the largest eigenvalue is λ_1, corresponding to $\vec{e}_1$ and the smallest is λ_3 corresponding to $\vec{e}_3$ [46].

Visualization of the diffusion tensor

The general shape of the diffusion tensor is usually visualized by an ellipsoid[2]. The axes of the ellipsoid coincide with the eigenvectors and the corresponding eigenvalues are taken as radii. The ellipsoid represents an iso-probability surface corresponding to the diffusion tensor and is illustrated in figure 2.22. The case of isotropic diffusion ($\lambda_1 = \lambda_2 = \lambda_3$) is represented by a sphere, while oblate diffusion ($\lambda_1 \approx \lambda_2 > \lambda_3$) appears to be disc-shaped and prolate diffusion ($\lambda_1 > \lambda_2 \approx \lambda_3$) to be cigar-shaped.

Examples of diffusion ellipsoids are shown in figure 2.23(e) for an *in vivo* data set of the brain white matter.

Scalar rotationally invariant measures derived from the diffusion tensor

The average magnitude of the diffusion along the three eigenvectors can be calculated by taking the trace of the tensor matrix or the sum of eigenvalues. This quantity is called mean diffusivity (MD):

$$\text{MD} = \langle \mathbf{D} \rangle = \frac{\lambda_1 + \lambda_2 + \lambda_3}{3} = \frac{Tr(D)}{3}. \tag{2.29}$$

The MD characterizes the overall mean-squared displacement of the water molecules. Maps of MD or trace of the human adult brain tissue do not typically show a great deal of image contrast, indicating that the average diffusion property of each voxel is relatively uniform both in GM and WM.

Measures to describe the anisotropy and discriminate for instance between GM and WM are essential but there is no single obvious way to index anisotropy. Three scalar measures have been proposed: fractional anisotropy (FA), relative anisotropy (RA) and the volume ratio (VR) corresponding with the following definitions [47,48]:

$$FA = \sqrt{\frac{3}{2}} \sqrt{\frac{(\lambda_1 - \langle \mathbf{D} \rangle)^2 + (\lambda_2 - \langle \mathbf{D} \rangle)^2 + (\lambda_3 - \langle \mathbf{D} \rangle)^2}{(\lambda_1^2 + \lambda_2^2 + \lambda_3^2)}}, \tag{2.30}$$

$$RA = \sqrt{\frac{1}{3}} \sqrt{\frac{(\lambda_1 - \langle \mathbf{D} \rangle)^2 + (\lambda_2 - \langle \mathbf{D} \rangle)^2 + (\lambda_3 - \langle \mathbf{D} \rangle)^2}{\langle \mathbf{D} \rangle}}, \tag{2.31}$$

$$VR = \frac{\lambda_1 \lambda_2 \lambda_3}{\langle \mathbf{D} \rangle^3}. \tag{2.32}$$

---

[2]The equation of a standard ellipsoid body in an xyz-Cartesian coordinate system is $\frac{x}{a}^2 + \frac{y}{b}^2 + \frac{z}{c}^2$

A VR of 1 represents isotropic diffusion, whereas FA and RA are zero in that case. FA is 1 and RA is $\sqrt{\frac{2}{3}}$ in case of cylindrically symmetric anisotropy (i.e. $\lambda_1 >> \lambda_2$) while VR equals zero in the case of oblate or prolate diffusion profiles. Among them, the FA gives the highest SNR [49] and is by far the most commonly used. Other scalar measures for expressing the diffusion profiles and preferred directions are listed in [50].

An FA-map of a slice through the brain is shown in figure 2.23(d). A colour code is used to visualize the direction of the diffusion tensor: red stands for the left-right direction, green for the top-bottom direction and blue for the in-plane direction. The direction of the diffusion can also be derived from the DWI's in those 3 directions (figures 2.23(a), 2.23(b), 2.23(c)). For instance, when a gradient is applied in the left-right direction, the corpus callosum (also indicated on figure 2.17 and 2.16) is hypointense on the DW-MRI while it is hyperintensive on the DWI's when the gradients are applied in the bottom-top direction and the in-plane direction.

An extensive list of the typical range of DT parameters found in the human brain *in vivo* is given by Pierpaoli et al in [51]. Values of FA in white matter are typically of the order of 0.7 (e.g. 0.69 $\pm$ 0.03 in the optic radiation [11]) while the grey matter has very low FA values.

Sequence parameter optimization

The precision of the ADC depends on the b-factor due to the presence of noise in the images. Taking a too low b-factor for estimating the ADC will give a small signal attenuation resulting in a low precision of the estimation. On the other hand, taking a too high b-factor may result in such a high attenuation that the signal is lower than the noise. It has been found that the product (bADC) should be 0.85 corresponding with a signal attenuation of 43% with respect to $S(0)$ [52]. As the ADC depends on the direction in WM, a fixed trade-off b-factor is normally used for all diffusion gradient directions, e.g. $b = 1000$ s/mm^2.

The choice of the diffusion gradient scheme for DTI has been optimized in terms of signal-to-noise [49,53–55]. To obtain a robust tensor estimation, DW-MRI should be performed in at least 20 isotropically distributed directions. The gradient directions are commonly chosen such that they coincide with the vertices of an icosahedron [55] or by minimizing the electrostatic repulsion force when the gradients are
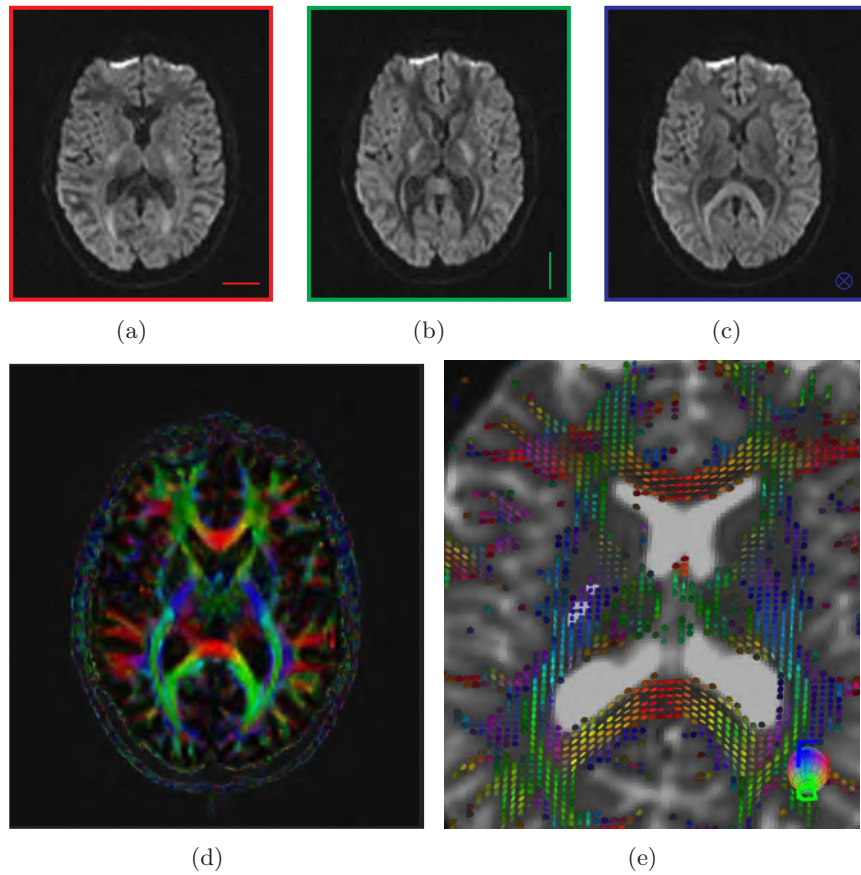
Figure 2.23: (a), (b), (c) DWI's. The direction of the applied gradient is colour-encoded and shown at the right bottom of each subfigure. (d) corresponding colour encoded FA map (e) Examples of diffusion ellipsoids representing the diffusion tensor.

treated as point charges [55, 56].

2.4.3 New techniques for characterizing diffusion- beyond the diffusion tensor.

The diffusion tensor model makes the assumption that the diffusion at the scale of a voxel is Gaussian, which allows us to use the generalised Einstein equation and the covariance matrix given by equation (2.15) as an appropriate model. However, this assumption, as we will see later in chapter 4 and 5, is not appropriate. Recent advances in MR gradient hardware have allowed high b-value diffusion imaging, revealing non-mono-exponential signal attenuation in brain white matter [57–60]. Moreover, the Gaussian diffusion model also fails in voxels containing fibre tracts in multiple directions. Due to these findings, the exponential model to describe the signal attenuation needs to be reconsidered. Different approaches are described below: the two-compartment model (section 2.4.3.1) and the cumulant expansion form (section 2.4.3.2) are alternative models to explain the non-exponential signal decay at high b-values while the q-space approach and derived HARDI models (section 2.4.3.3) are techniques mainly used to described the diffusion signal in voxels containing multiple diffusion directions.

2.4.3.1 Two-compartment model

Numerous studies [57,58] suggest that the DW-MRI signal S in brain white matter can be described by a bi-exponential model, i.e. a weighted sum of two exponential functions, corresponding to two water diffusion pools in slow exchange, with a slow and a fast diffusion coefficient [57, 58]:

$$\frac{S(b)}{S(0)} = \alpha e^{-bADC_{\text{slow}}} + (1 - \alpha)e^{-bADC_{\text{fast}}}, \qquad (2.33)$$

where ADC_{slow} and ADC_{fast} are the ADC's of the slow and fast diffusion pools, respectively, and α and (1-α) the corresponding population fractions.

Although it was suggested that these two pools would correspond with the intra- and extracellular water pools, the derived fractions do not agree with the corresponding intra- and extracellular fractions [33]. In addition, these compartments have not been histologically identified [61].

2.4.3.2   Cumulant expansion form

A model independent description for S has been investigated where the logarithm of S is fitted as a power series in b [62]:

$$\ln\left(\frac{S(b)}{S(0)}\right) = C_1.b + C_2.b^2 + b^3 + \ldots. \qquad (2.34)$$

This formula describes the cumulant expansion of $\ln(S)$ in powers of the applied gradients. The coefficients of the first and second order yield the apparent diffusion coefficient ADC and the apparent diffusion kurtosis ADK (see equation (2.16)):

$$C_1 = -ADC, \qquad (2.35)$$

$$C_2 = \frac{1}{6}ADK.ADC^2. \qquad (2.36)$$

The termination of the series in equation (2.34) after the Nth order term is called the b^N cumulant expansion form. The usefulness of the cumulant expansion form depends on its convergence. This can be characterized by the convergence radius b_c [63]. For $b < b_c$, termination of the series after the Nth-order provides good approximation of the real signal attenuation.

2.4.3.3   q-space

The q-space approach, originally introduced by Callaghan in [64] and Cory and Garroway [65], also assumes no specific model of water diffusion. Callaghan introduced the q-vector $\vec{q}$ as:

$$\vec{q} = \frac{\gamma\delta}{2\pi}\vec{G}, \qquad (2.37)$$

where $\vec{G}$ is the vector corresponding to the direction and magnitude of the diffusion gradient. $\vec{q}$ is analogous to the vector $\vec{k}$ in equation (2.9) which is at the basis of the MRI theory. If the diffusion gradients in a Stejskal-Tanner sequence are infinitely narrow ($\delta \to 0$ in figure 2.19), the signal attenuation ratio of the experiment is given by:

$$\frac{S(\vec{q},\Delta)}{S(0)} = \int P(\vec{r},\Delta)e^{-i2\pi\vec{q}.\vec{r}}d\vec{r}, \qquad (2.38)$$

where $P(\vec{r},t)$ is the conditional probability that a molecule (initially at the origin) is displaced over $\vec{r}$ in a time t (cf. equation (2.12)). By

taking the inverse Fourier transform, the probability density function can be recovered:

$$P(\vec{r}, \Delta) = \frac{1}{S(0)} \int S(\vec{q}, \Delta) e^{i2\pi \vec{q} \cdot \vec{r}} d\vec{q}. \qquad (2.39)$$

By sampling the signal attenuation $S(\vec{q}, \Delta)$ for a series of locations in $\vec{q}$-space, the measured profile can be directly related to molecular displacements due to incoherent random motion without assuming Gaussian behaviour. When integrating the PDF over a radial direction, the orientation distribution function (ODF) is obtained, which is related to the fibre directions in a voxel. The fibre ODF can be obtained using a spherical deconvolution [66]. As the fibre ODF gives in fact the distribution of the fibre orientation present in a voxel, spherical deconvolution is useful in the field of tractography [67]. This will be illustrated further in section 6.4.

Usually $\vec{q}$-space is sampled by incrementing the gradient strength and changing its direction such that several spherical shells are acquired in $\vec{k}$-space. This acquisition method is known as the high angular resolution diffusion imaging (HARDI) technique [68–70]. In the case of Q-ball imaging, only one spherical shell is sampled, which reduces the scan time [71]. The measurement of the small displacements to acquire the PDF requires very high diffusion gradient strength to satisfy the narrow pulse assumption $\delta \to 0$. Whereas the advantage of the $\vec{q}$-space approach is its model-free estimation, the major drawbacks of the technique are the technical requirements and the long scanning time. The gradients available on whole-body scanners are not strong enough to sample appropriately the whole q-space.

2.4.3.4 Stretched-exponential form

A stretched-exponential model is proposed by Bennett et al to [72]:

$$\frac{S(b)}{S(0)} = e^{-(bDDC)^s}, \qquad (2.40)$$

where s is the stretching parameter and DDC stands for distributed diffusion coefficient. This model assumes the signal attenuation to arise from a collection of uncoupled exponential decay processes. Hall et al [73] also used this form to link the signal decay to anomalous diffusion (see section 2.3.1) by relating s to the walk dimension as $s = 2/d_w$. The stretched-exponential form is mentioned for the sake of completeness here and is not used further in this work.

2.5   Examples of clinical applications of diffusion MRI

The first clinical potential of DW-MRI was demonstrated by Le Bihan et al in 1986 [22] who showed that the ADC in brain tumours is significantly reduced in comparison to normal brain tissue. They also demonstrated that the ADC increases in oedema in comparison to normal tissue and that the ADC in grey matter is higher than in white matter. The fact that water ADC is significantly decreased in malignant tissue [33] makes whole body diffusion MRI [74] a potential alternative approach to fluoro-deoxyglucose (FDG)-PET [75].

The most firmly established clinical application of diffusion MRI is the early detection of ischaemic stroke [11]. Using DW-MRI, ischaemic stroke in the early phase can be detected with a higher sensitivity and specificity than CT and conventional MRI. Examples are shown in figures 2.24 and 2.25. The diagnostic power of DW-MRI is mainly based on its capacity to differentiate between cytotoxic and vasogenic oedema. Nowadays, diffusion MRI is clinically used for detecting patients with acute ischaemic stroke [76]. The observed reduction of the ADC in cerebral fluid is explained by membrane depolarization and related cell swelling in ischaemia [77]. When assuming that the diffusion in the intracellular space is more restricted than in the extracellular space, a net transport of water from the extracellular space into the intracellular space causes a decrease in the ADC [77].

The ADC and diffusion anisotropy measures change dramatically during development, reflecting underlying changes in tissue water content and cytoarchitecture. Those DTI parameters also change in response to brain injury such that DW-MRI offer the possibility of detecting injury earlier than conventional imaging methods [78]. Also the effect of ageing can be studied with DW-MRI. In contrast to the white matter maturation process, investigators have observed significant declines in the white matter ordering in normal as well as abnormal ageing [79].

DW-MRI also enabled the investigation of the effect of disease on the white matter by studying diffusion anisotropy parameters. Various low level pathological processes such as oedema, neurotoxicity and inflammatory events may have an impact on the measured diffusion parameters. Several types of diseases such as MS, Alzheimer's disease, amyotrophic lateral sclerosis and neuropsychiatric disorders are current research topics for DW-MRI [80, 81].

(a) T_2 (b) DWI
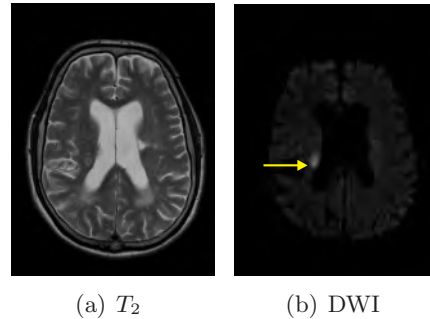
Figure 2.24: Images taken from a patient with ischaemic stroke in the early phase. T_2-weighted image is normal in the lesion region, but the averaged DWI shows significantly reduced diffusion compared with the equivalent region in the right periventricular lobe.

(a) T_2 (b) FLAIR   (c) DWI

(d) CT   (e) follow-up CT
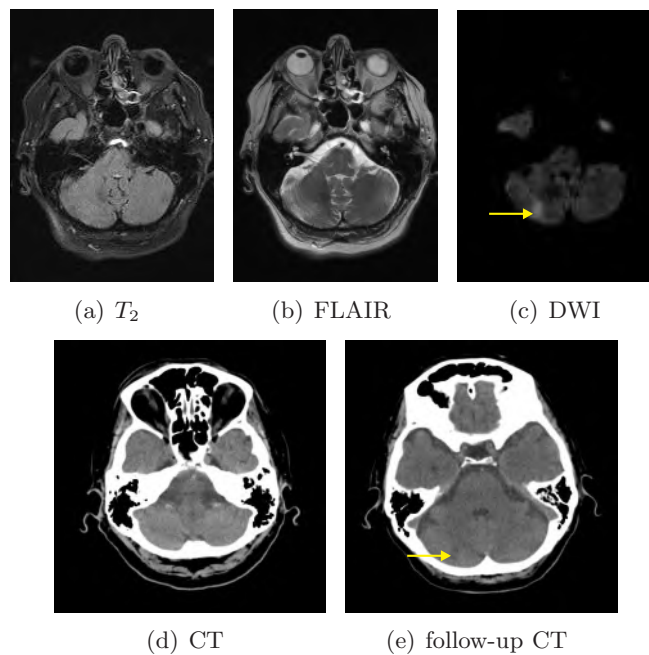
Figure 2.25: MR images of a patient with ischaemic stroke. Diffusion weighted (DW) and fluid-attenuated inversion recovery (FLAIR) images are typically used to establish the diagnosis of acute ischaemic stroke. The FLAIR image is T2-weighted with the signal of the cerebrospinal fluid (CSF) attenuated. At the early phase, the lesion in the right cerebellar hemisphere is only visible on the averaged DWI. A follow-up scan on CT the following day shows a slightly hypodense lesion.

2.6   Fibre tractography

The local white matter orientation provided indirectly by DW-MRI can be used to reconstruct the pathways of major white matter fibre tracts through the brain. This reconstruction process is known as fibre tracking, or fibre tractography. Two examples of fibre tractography are shown in figures 2.26(b) and 2.26(a). The corticospinal tract is formed by all the axons travelling from the cerebral cortex of the brain to the spinal cord. The corpus callosum connects the left and right hemispheres of the brain. More examples of fibre tracts can be found in [82].

A considerable number of tractography algorithms have been developed which vary in the way they deal with noise and how they model the original DW-MRI data and represent the reconstructed tract. Also non-tensor models for diffusion have been applied to overcome some of the shortcomings of tensor imaging. For a detailed overview of tractography and other algorithms to probe brain connectivity, we refer to some recent PhD theses covering these subjects [83, 84].

Validation

Fibre tractography can provide macroscopic neuroanatomical information of the white matter structure. Specifically, it can parcellate the white matter into several fasciculi containing fibres running largely in the same orientation. As the current resolution of DTI is a voxel size of about 2 mm^3, it is presently not possible to resolve white matter tracts into individual axons whose diameter is typically less than 10 μm. Moreover, there are still some unsolved issues such as revealing crossing fibres present within one voxel, especially in the presence of noise and low angular resolution. Also crossing fibre bundles and "kissing fibre" bundles [85] are indistinguishable from a fibre tracking point of view. It has become undeniable that validation is of central importance for the development of tractography [86].

Validation has been performed on post mortem tissue and with animal models using tract-tracing methods based on chemical tracers [86]. The results in these studies often have high uncertainties due to noise and subject motion. Software phantoms may overcome these issues. For the validation of fibre tractography, a mathematical framework for simulating DTI data is proposed by Leemans et al [87], based on the physical properties of the WM fibre bundles. Such synthetic data sets are useful for testing new tractography al-
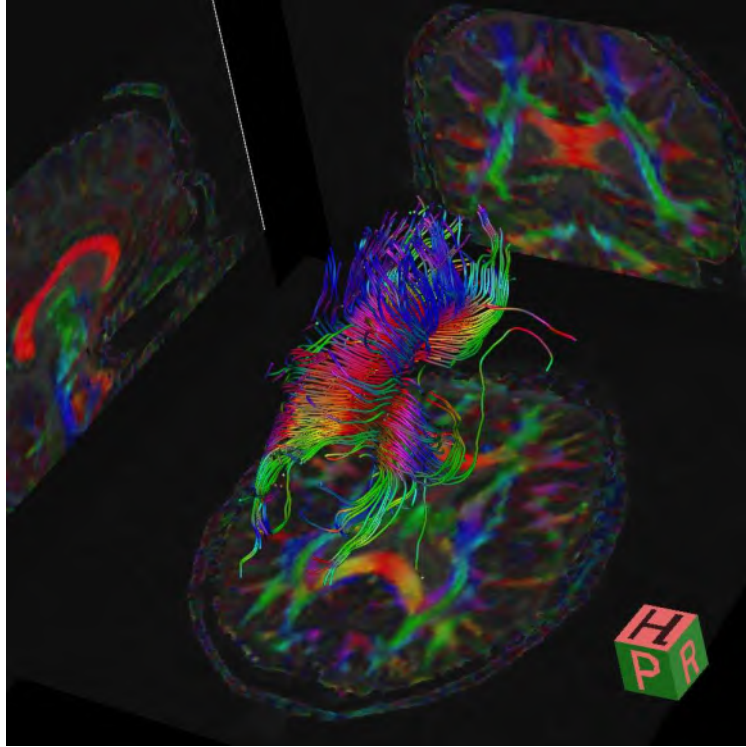
(a) corpus callosum
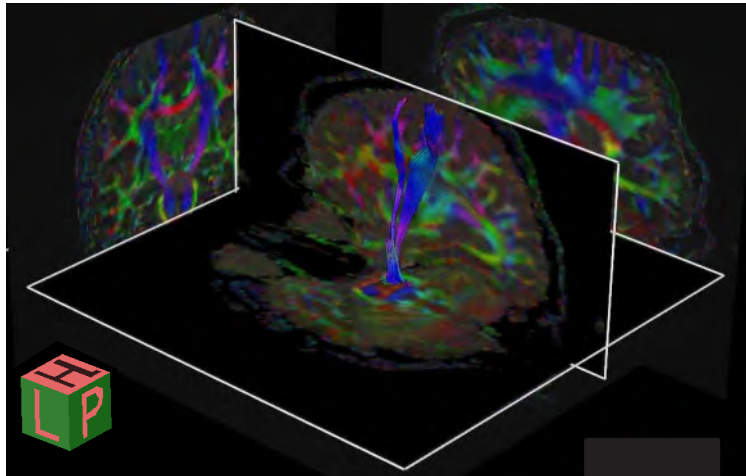
(b) corticospinal tract

Figure 2.26: Tractography result of the corpus callosum (a) and the corticospinal tract (b). H = head, P = posterior, R =right, L = left.

gorithms but as they are mostly based on the tensor assumption of a Gaussian diffusion profile, they will fail for the particular cases of crossing fibres. Probably the ideal validation study may require a physical hardware phantom with well-known structure and diffusion behaviour in which uncertainties as the effect of motion and partial volume effects can be removed [86].

2.7   Conclusion

For a good understanding of the following chapters, the basic principles of DW-MRI are explained.

We have shown how the magnetisation of atomic nuclei gives rise to a macroscopically measurable NMR signal. The NMR phenomenon can create an image with a desired image contrast. Attention was also paid to fast imaging sequences suitable for DW-MRI such as standard EPI and spiral EPI and the related image artefacts.

The physical process of self-diffusion as a random walk was discussed whereby the difference between free diffusion with a Gaussian displacement profile and restricted diffusion was explained. The diffusion of water molecules in brain white matter appears anisotropic, the specific causes and the role of the micro structure remain still unclear.

Consequently, the method of DW-MRI was explained by which the random motion can be indirectly measured with MRI and guidelines were provided on how to perform DW-MRI in practice. The diffusion tensor concept, based on a Gaussian diffusion profile, can be used to visualize the white matter anisotropy. A number of scalar indices to describe the shape of the diffusion tensor were introduced, including the widely used fractional anisotropy. As the diffusion tensor model fails at high b values and in voxels containing multiple fibre directions, some alternative models were introduced.

The potential applications of DW-MRI in clinic are innumerable, including examination of stroke, tumours, ageing and white matter diseases. The anisotropy of white matter enables also the reconstruction of the neural fibre tracts. For fibre tractography, but also for diffusion sequence design, system calibration and the study of diffusion models, an anisotropic diffusion fibre phantom with a well-known structure and diffusion properties is an essential tool for the validation and further optimization of DW-MRI. The design of such a phantom is the topic of the next chapters.

3

Design of anisotropic diffusion hardware fibre phantoms

3.1   Introduction

A gold standard for the validation of DW-MRI is crucial for clinical purposes. Physical hardware diffusion phantoms with a well defined structure, composition and architectural organization are required for the development of an accurate quality assessment protocol for DW-MRI on clinical MR-scanners and for the validation of diffusion models and tractography methods.

This chapter presents an overview of the different kind of hardware diffusion phantoms. The advantages as well as the disadvantages are mentioned for each phantom type (see section 3.2). Non-biological anisotropic diffusion fibre phantoms are investigated in more detail since they are the best candidate for quantitative validation of DW-MRI. Section 3.3 describes the manufacturing process of anisotropic fibre phantoms. In section 3.4 and following, several fibres are compared with respect to the fibre material and phantom size in terms of their diffusion properties and SNR.

3.2   Overview of hardware diffusion phantoms

3.2.1   Isotropic diffusion phantoms

Liquids exhibit isotropic diffusion and can be characterized with a well established diffusion constant. Isotropic liquids are used as a standard because they are well-defined, stable, readily available and require only a minimum of on-site laboratory work. The proposed liquids have preferably one frequency peak in the nuclear magnetic resonance spectrum.

Water has been widely used as a test liquid e.g. to calibrate and correct for eddy current induced artefacts in DW-MRI [88, 89] or to investigate the noise immunity characteristics of diffusion parameters [90]. However, using water has some drawbacks such as a rather high diffusion coefficient (DC) at room temperature (2.0×10^{-9} m^2/s at 20°C) in comparison with the DC found in normal brain (0.3-1.0×10^{-9} m^2/s) [51]. Moreover, the water must be doped to bring its T_2-relaxation time down to *in vivo* values and its relatively low viscosity can cause artefacts due to bulk motion.

Aqueous solutions of sucrose and agar gel have been used in [91] to design a test-object that simulates the diffusion and T_2 contrast differences between normal grey matter and areas of acute ischaemia. The presence of low agar concentrations in water reduces T_2 while the presence of sucrose at high concentration (400 g/l), both reduces the DC and T_2. Water doped with $CuSO_4$ and water doped with sucrose have been used in quality assurance protocols to assess the accuracy and precision of the ADC measurements in terms of SNR, signal reproducibility and differences between nominal and effective diffusion gradients [92].

Also several organic liquids have been proposed as suitable materials for use in isotropic test objects for quantitative diffusion measurements. Cyclic and linear alkanes are proposed in [30] for the measurement of the ADC or the DT because their DC, T_1 and T_2 are in the same range as those observed in white matter and they have a higher viscosity than water. DC's of water and other molecular liquids for quantitative calibration of DW-MRI in function of the temperature are listed in [93].

3.2.2   Anisotropic hardware diffusion phantoms

Anisotropic diffusion phantoms with a well-known structure and anisotropy become essential in order to evaluate quantitatively mea-

sured diffusion parameters expressing the anisotropy such as the DT, FA and to analyse the variability of different MR-scanners in terms of anisotropy and fibre orientation. They are also preferable while developing and testing new diffusion weighted sequences on clinical MR-scanners. Both biological phantoms and synthetic phantoms are used for the validation of DW-MRI.

3.2.2.1 Biological phantoms

Plants

Plants and fruits are widely available and often used as test-objects when performing DW-MRI [94]. Carrot is used for b-matrix correction [95], celery is used to evaluate the effect of inhomogeneous susceptibility samples on DW-MRI [96, 97] and asparagus [98] is applied to test new diffusion sequences [99] and as an illustrative model for restricted diffusion [100].

Monocotyl plants or monocots are most suitable as an illustrative model system for anisotropic diffusion since they demonstrate isotropic diffusion in the parenchyma and anisotropic water diffusion in the vascular bundles, consisting of the phloem and xylem. Examples of monocots such as celery (*Apium graveolens*) [96, 97] and asparagus (*Asparagus officinalis*) [98–100] are described in the literature for usage as diffusion phantoms.

Asparagus is described here as an example. Figure 3.1 shows a microscopic image of a cross-section through the inner part of the asparagus, composed of parenchyma in which vascular bundles are embedded. There is an increase in size of the vascular bundles towards the centre of the stem. Figure 3.2 shows a close-up of a vascular bundle. The diffusion of water is anisotropic in the xylem while the diffusion is isotropic elsewhere in the parenchyma and in the phloem. DW-MRI and fibre tracking was performed on the asparagus. The resulting fibre tracts are shown in figure 3.3. The FA was on average 0.15 ± 0.05.

The degree of anisotropy of diffusion in vegetables and plant stems is in general rather low and the presence of air may cause susceptibility artefacts. Therefore they are not useful as calibration phantoms. An additional drawback is their limited preservability because of season availability and dependence on storage and delivery conditions. They are also proposed as a model to test new diffusion models such as kurtosis imaging [100]. However, several physiological aspects such as the exchange of water trough the vessel walls are not very well-
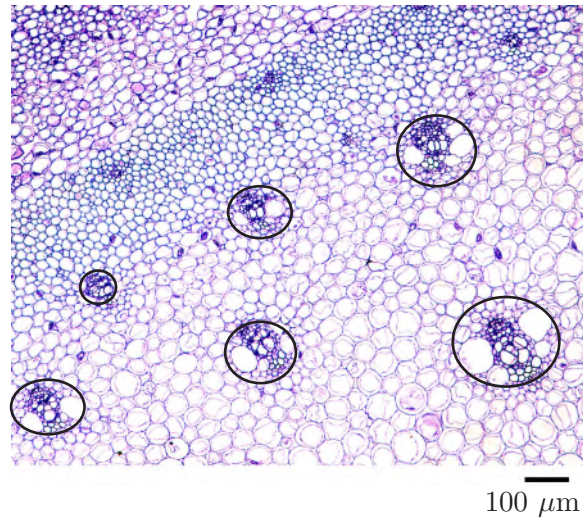
Figure 3.1: A microscopic image of a cross-section through the asparagus. The vascular bundles are indicated with ellipses.

Xylem   Phloem   100 μm
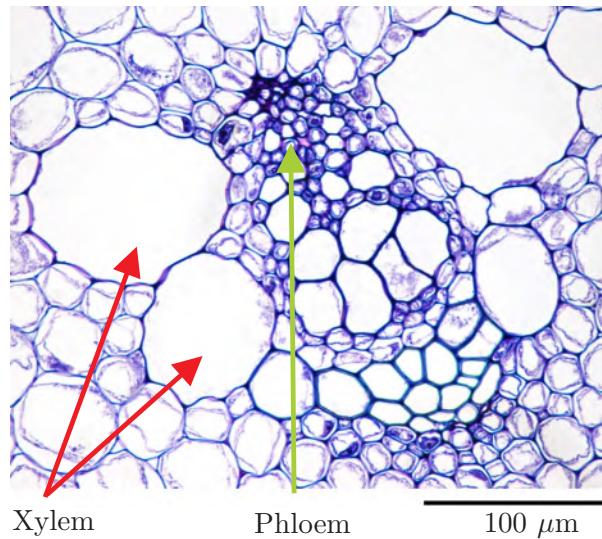
Figure 3.2: Close-up of a vascular bundle. Cells with a large diameter form the xylem, which are in fact long tubular vessels with a thick wall. The smaller cells form the phloem, which are either tubular and filled with air or spherical and containing water.
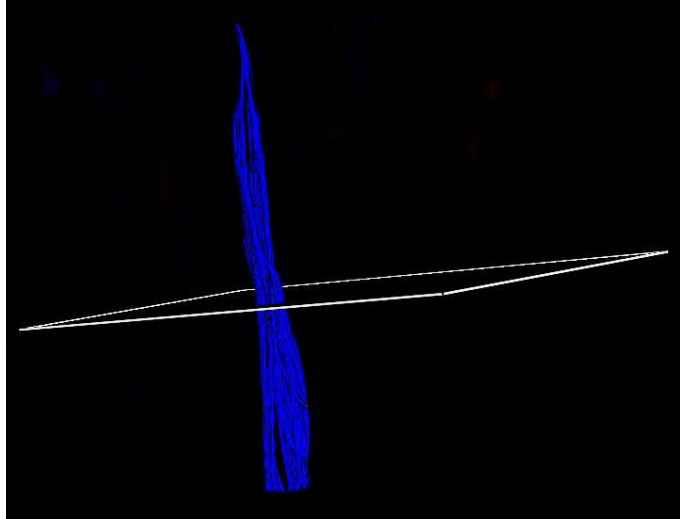
Figure 3.3: Fibre tracking results of an asparagus

known, which makes them cumbersome to use for validation of new diffusion models and imaging techniques.

Biological tissue

Besides plants, biological phantoms made of excised nerve tissue can be useful as test-object. Biological phantoms made of excised pig and spinal cord are described in the literature for testing new DTI sequences [97,101] and to develop new fibre tracking algorithms [102]. They are also used to validate diffusion models in brain white matter such as the CHARMED model [103] or spherical harmonics [104] and to verify new tissue segmentation and classification methods with DTI [105].

Biological phantoms are useful as test object and for validation of diffusion models because their structure is similar to the *in vivo* situation. On the other hand, the biological tissue is not widely available and the preparation requires specialized knowledge. Their exact structure remains in general unclear and they are not suitable for calibration purposes due to their limited storage time and lack of stability. Moreover, they can not be applied to create more complex structures similar to the WM geometry such as fibre crossings and curved fibres. Synthetic anisotropic hardware diffusion phantoms have been proposed recently to overcome these issues.

3.2.2.2 Synthetic phantoms

Several non-biological anisotropic hardware diffusion phantoms have been proposed in the literature recently. Two different kind of phantoms can be classified: capillary phantoms and fibre phantoms. There is a large variety in the size and type of the used materials. All the described phantoms are intended for the validation and quality assessment of DW-MRI, fibre tractography and Q-ball imaging on clinical MR scanners. The considered capillaries were made of glass [106] and plastic [106–110] whereby the diameter varied from $20\,\mu$m up to $80\,\mu$m. Diverse fibre materials were used for the manufacturing of fibre phantoms such as hemp, linen [111], polyamide [112], polyester [113], polyethylene [114–116] and rayon [117]. Diameters ranged from $10\,\mu$m up to $340\,\mu$m.

In the next sections, we will focus on the manufacturing of fibre phantoms and describe in more detail how the different material properties and size of the phantom influence the outcome of the DW-MRI experiment.

3.3 Manufacturing process of anisotropic diffusion fibre phantoms

All the constructed fibre phantoms consisted of straight bundles of parallel unwounded fibre filaments immersed in water. The fibres in the water were surrounded by a flexible poly-olefin low-temperature shrinking tube (Versafit, Tyco Electronics, Raychem). Subsequently, the water was heated to $90°$C for at least $600\,$s so that the shrinking tube shrinked and a homogeneously, densely packed fibre bundle was created, as shown in Fig. 3.4.

To reduce the effect of susceptibility differences caused by air bubbles, the whole fabrication process was performed under water. Remaining small air bubbles attached to the fibres and the shrinking tubes were removed by squeezing and repetitively placing the bundles in a vacuum chamber and subsequently in an ultrasonic bath. More efforts were required for hydrophobic materials such as Dyneema® fibre bundles to get rid of the air bubbles. The presence of air bubbles inside the fibre bundles was evaluated by acquiring a gradient echo B_0-field map using a phase encoding sequence ($TE_1 = 10\,$ms, $TE_2 = 12\,$ms) [118]. Almost no susceptibility artefacts due to the presence of air were noticed on the field map.
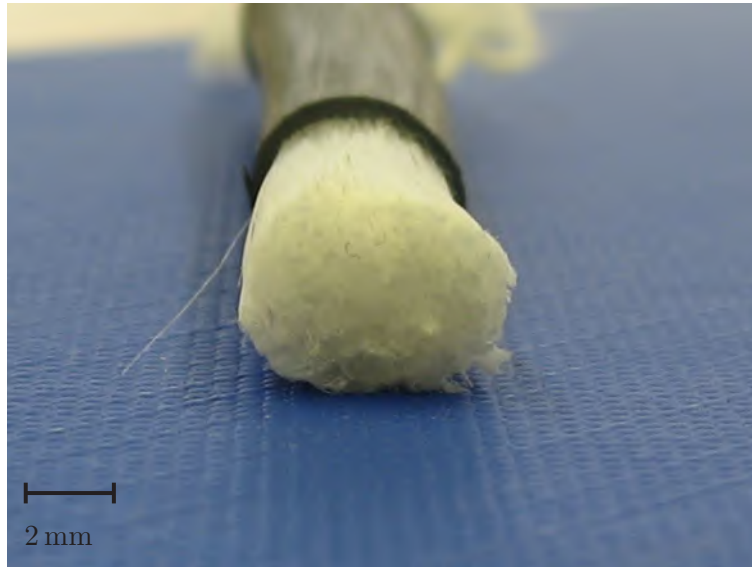
(a) Transversal view
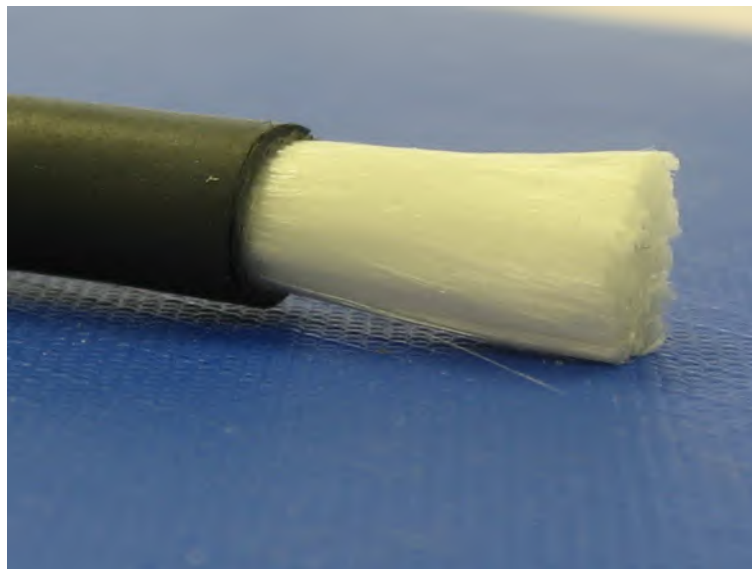
(b) Longitudinal view

Figure 3.4: Photographs of a fibre bundle with the shrinking tube partially removed: (a) transversal, (b) longitudinal view

Figure 3.5: System to wind the fibre filaments automatically and meanwhile count the number of filaments.

For each fibre phantom, the fibre filaments were wound and counted automatically (see figure 3.5). Fibre bundles with a varying fibre density (FD) were obtained by using various numbers of fibre filaments. The shrinking tube was left to shrink to a diameter of 9.5 mm. The fibre bundles were fixed to a PMMA plate and placed in a cylindrical container (see figure 3.6) to reduce the effect of motion during the magnetic resonance (MR)-measurements.

DW-MRI and tractography are performed as described further in section 3.4.2. An example of the colour coded cuboids of the FA in a Dyneema$^{®}$ fibre phantom is shown in figure 3.7(a). The corresponding fibre tracking result is shown in figure 3.7(b), demonstrating a good agreement between the actual fibre direction and the direction of the reconstructed fibres. FA was on average 0.3 with a standard deviation of 0.04.

The reproducibility of the manufacturing process and the homogeneity of the fibre phantoms was investigated by manufacturing 14 fibre bundles made of Dyneema$^{®}$ fibre material including exactly the same number of fibre filaments. The fibre bundles were manufactured in separate groups consisting each of 3 or 4 fibre bundles. The proton density fraction (PD) may serve as a measure for the FD with FD defined as 1-PD. The measured PD of different fibre

Figure 3.6: Photograph of the cylinder phantom with fibre phantoms placed inside

phantoms was on average 0.45. Figure 3.8 (a) shows the variation in the mean PD-values and corresponding standard deviation for all the fibre phantoms. The ROI's contained 386 ± 53 voxels. The fibre phantoms are reproducible within 10 %. The measured mean PD and corresponding standard deviations are shown in figure 3.9 (b) for the different slices in one fibre phantom. ROI's contained 770 voxels. The variation of PD within one fibre phantom was also 10 %.

Figure 3.8 and figure 3.9 demonstrate that anisotropic synthetic fibre phantoms can be manufactured in a reproducible way using shrinking tubes which pack the fibres densely and homogeneously together. During the whole process, special care should be taken to get rid of air bubbles inside the fibre phantoms, especially when using hydrophobic fibre materials such as Dyneema$^{®}$.
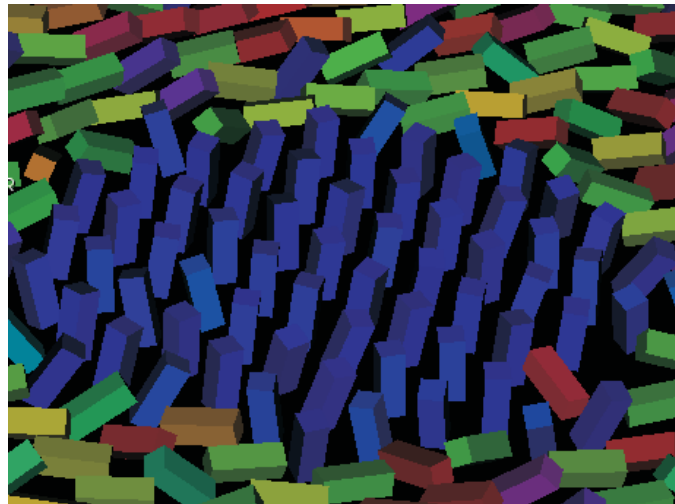
(a)
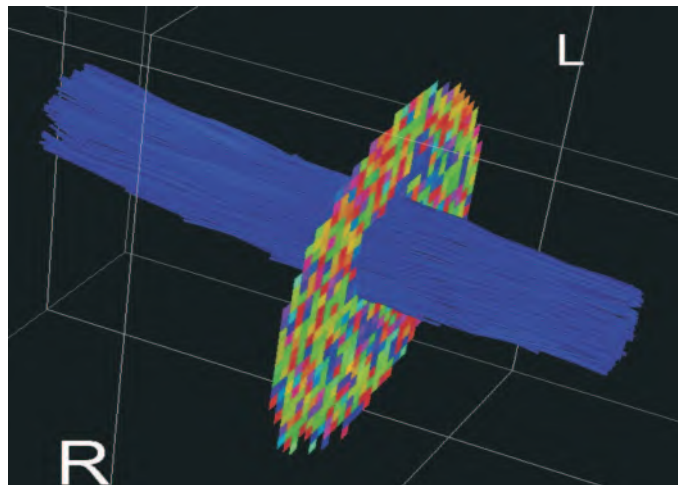
(b)

Figure 3.7: (a) A colour-encoded FA-map of a slice through a Dyneema®
fibre phantom. For each voxel, the principal eigenvector is rendered as a
cuboid. (b) Fibre tracts after DTI of a fibre phantom
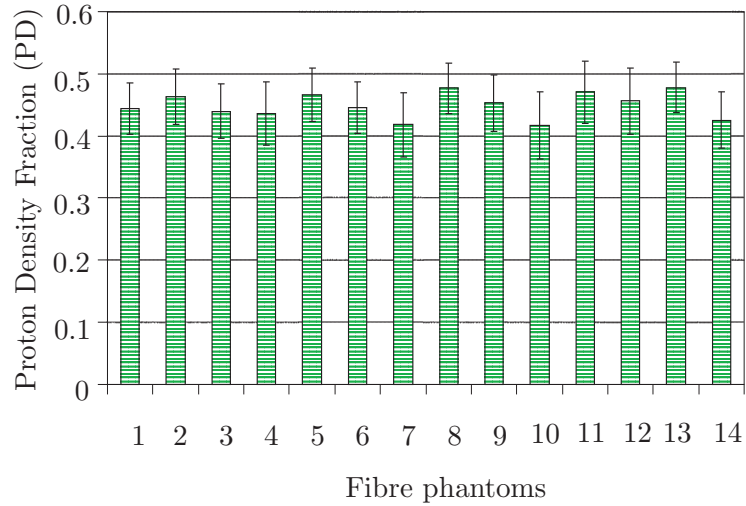
Figure 3.8: PD measurements in different fibre bundles containing equal number of Dyneema® fibres showing the reproducibility of the manufacturings process. The error bars indicate the standard deviation of the measured PD in each fibre phantom.
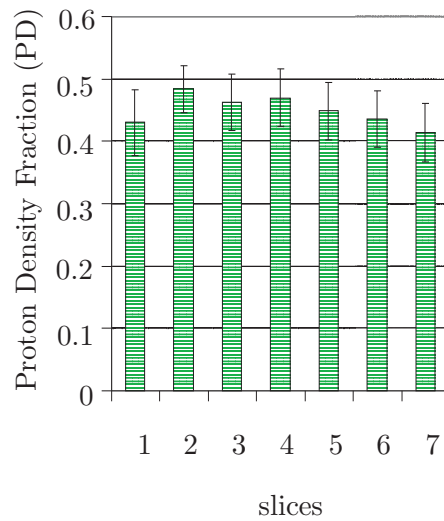
Figure 3.9: PD measured in different slices in one fibre bundle illustrating the homogeneity of one fibre phantom. The error bars indicate the standard deviation of the measured PD in each slice.

3.4   Comparison of fibre materials

When fabricating anisotropic diffusion fibre phantoms, a crucial question is how the different material properties and size of the phantoms influence the outcome of the DW-MRI experiment. Besides diffusion properties such as FA, also SNR is considered. Equation (2.19) which describes the signal decay in case of diffusion, shows an exponential decay determined by T_2 and an initial magnetisation determined by the PD. Both parameters affect the SNR of the measurement.

The diffusion properties of several potential synthetic fibre materials are compared. The effect of the fibre radius and fibre density on the FA is evaluated. The role of surface relaxation on the FA, as well as on the measured T_2-relaxation time is investigated. Differences in magnetic susceptibility between fibres and water may bias the outcome of the DW-MRI experiment and reduce the T_2-time. This effect has been studied as well.

3.4.1   Tested fibre materials

Four potential fibre materials for constructing fibre phantoms are studied. Fibre filaments with varying diameter were chosen to evaluate the effect of the fibre radius:

- Dyneema® (Dyneema SK75 1760 dTex, DSM) is a high strength, lightweight high performance fibre made from Ultra High Molecular Weight Polyethylene (UHMWPE). The fibre is chemically inert to water, ultra hydrophobic and impermeable to water.

- Nylon (DuPont Tynex® 612 Nylon Filament, Dupont Filaments) is a polyamide fibre produced by a condensation reaction of dodecanedioic acid and hexamethylene diamine. This nylon fibre absorbs small quantities of water.

- Fibreglass (Owens-Corning) are extremely fine fibres made of glass. Fibreglass is hydrophilic.

- Carbon fibre is a material consisting of long thin sheets of graphite-like carbon, packed to form a fibre. Carbon fibre is hydrophilic.

Scanning electron microscope (SEM) images were made of the Dyneema®, Fibreglass and carbon fibre to measure its radius (see figure 3.10). The radius of the nylon fibre, $32\,\mu$m with a tolerance allowance for variation of $\pm 2.5\,\mu$m, was provided by the manufacturer.

(a) Dyneema

(b) Carbon
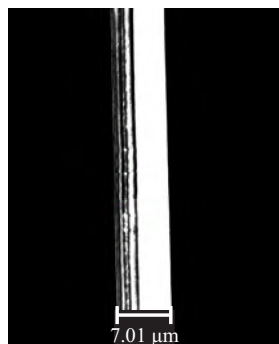
(c) Glass

Figure 3.10: SEM images of the different types of tested fibre materials: (a) Dyneema®, (b) Carbon, (c) Fibreglass
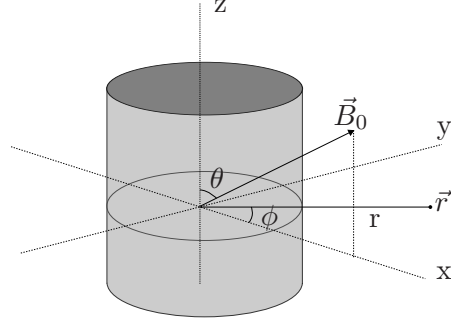
Figure 3.11: The coordinates (r, φ) to describe the position $\vec{r}$ relative to a cylinder. An external magnetic field $\vec{B}_0$ is applied that makes an angle θ with the longitudinal axis of the cylinder.

In order to evaluate the effect of the fibre density, 5 carbon fibre phantoms, 6 fibreglass phantoms, 12 nylon phantoms and 8 Dyneema® phantoms were manufactured containing varying numbers of wires as described in section 3.3.

3.4.2   MR-measurements

Measurements were performed at 20°C on a Siemens Trio scanner (3T, Erlangen, Germany) equipped with an 8-element head coil. Measured parameters were PD, T_2 and FA.

Susceptibility induced magnetic field inhomogeneity

Differences in magnetic susceptibility between fibres and water may induce internal gradients when placing the fibre phantom in an external magnetic field $\vec{B}_0$. As the radius r_{fibre} of the fibres is extremely small in comparison to the length of the fibres, they can be considered as infinite cylinders with a susceptibility χ. When a static external magnetic field $\vec{B}_0$ is applied in a medium consisting of one long cylinder, the magnetic field deviation, $\Delta B = (\vec{B} - \vec{B}_0).\vec{B}_0$, in a point $\vec{r}$ around the cylinder can be approximated in the limit of a small susceptibility difference between water and cylinder, $\Delta\chi <<$ 1 [2]:

$$\Delta B \approx \frac{\Delta\chi}{2} B_0 sin^2(\theta) \left(\frac{r_{\text{fibre}}}{r}\right)^2 cos(2\phi), \qquad (3.1)$$
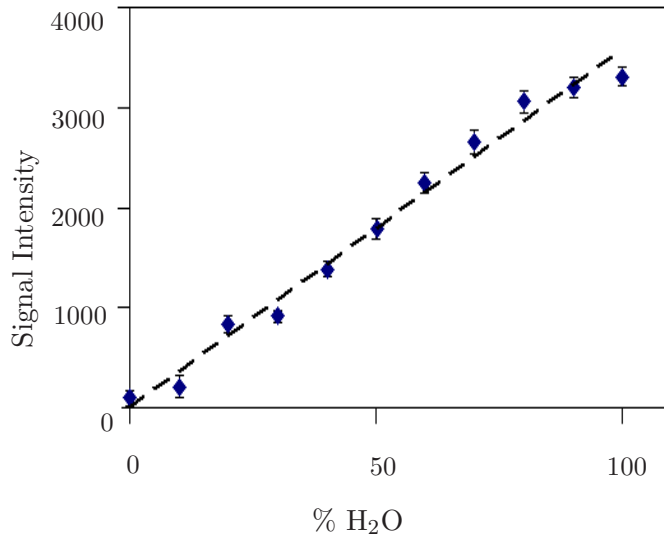
Figure 3.12: The MR signal intensity of test tubes containing varying solutions of water and deuteriumoxide was measured showing a linear relationship between signal intensity and proton fraction.

with the position of $\vec{r}$ determined by the coordinates r and ϕ as shown in figure 3.11 and θ the angle between $\vec{B}_0$ and the axis of the long cylinder. It is clear that in case of parallel alignment of all the fibres with $\vec{B}_0$, all normal field components of all magnetic field vectors vanish and the field outside the cylinders is equal to B_0. By increasing the angle θ, a spatial dependent offset in the magnetic field ΔB is induced resulting in increasing local field inhomogeneities.

Proton density and T_2-measurements

T_2- and proton density (PD) measurements were performed using a multiple spin-echo sequence. The PD and T_2 were obtained by fitting M_0 and T_2 to the T_2-decay function (equation (2.7)) using a Levenberg-Marquardt algorithm in Matlab. Test tubes containing a mixture of water (H_2O) and heavy water (D_2O) were used as a concentration standard. Deuterium has a different magnetic moment than hydrogen and therefore does not contribute to the NMR signal at the hydrogen resonance frequency. Figure 3.12 proofs the linear relationship between signal intensity and proton density.

The PD of the fibre phantoms was calculated as the signal M_0 in

a region of interest (ROI) of the phantom over M_0 in a neighbouring ROI containing water. This way, local variations in the signal intensity due to B_1 inhomogeneities were minimized.

T_2- and PD measurements were performed with a multiple spin-echo sequence with a TR of 10 s and a receiver band width (BW) of 130 Hz/pixel. Image series with 32 contrasts were obtained with an inter-echo time spacing ΔTE varying between 7 ms and 40 ms to enable a robust fit of the T_2 decay function in a wide range of T_2-values (0.1 s up to 1.8 s). The resolution was 0.9 mm × 0.9 mm × 2 mm.

Estimation of the surface relaxivity

There exists a relationship between T_2 and pore size, i.e. the volume-to-surface ratio (V/S), in a water-wet pore system, well-known from NMR measurements in well logging [119]. The surface relaxivity ρ is the proportionality constant between T_2 and pore size in a water-wet pore system. When the pores between the fibres are completely water-saturated, the T_2 relaxation rate or R_2 will be described as [120, 121]:

$$R_{2\text{fibre}} = \frac{1}{T_{2\text{fibre}}} = \frac{1}{T_{2\text{water}}} + \rho\frac{S}{V} + R_{2IG}, \qquad (3.2)$$

with $T_{2\text{water}}$ the T_2 of water in bulk and $T_{2\text{fibre}}$, $R_{2\text{fibre}}$ the T_2, R_2 of water between the fibres in the phantoms. . An additional decay R_{2IG} can be observed in case of internal field gradients caused by susceptibility differences between water and fibre material.

For fibre phantoms, modelled as long cylinders, the surface-to-volume ratio $\frac{S}{V}$ equals

$$\frac{S}{V} = \frac{2}{r_{\text{fibre}}}\frac{1 - PD}{PD}. \qquad (3.3)$$

In the case of parallel alignment of the fibres with the B_0-field, the influence of field inhomogeneities caused by local variations of the susceptibility is minimized as the term R_{2IG} in equation (3.2) can be neglected. For each fibre material, the measured PD-values and radius were used to calculate the surface-to-volume ratios using equation (3.3). The surface relaxivity ρ of each fibre material is derived by fitting the measured T_2 and derived $\frac{S}{V}$ to equation (3.2) using a Levenberg-Marquardt algorithm.

fibre	radius	surface relaxivity
Dyneema	$8.5 \pm 1.3 \mu m$	$0.13\,\mu m/s$
Nylon	$32 \pm 2.5\,\mu m$	$4.6\,\mu m/s$
Carbon fibre	$4 \pm 0.1\,\mu m$	immeasurable
Fibreglass	$3.5 \pm 0.1\,\mu m$	$7.7\,\mu m/s$

Table 3.1: Radius (mean value and standard deviation) and estimated surface relaxivity of the fibres investigated in this study.

FA measurements

DW-MRI was performed in 30 directions with an EPI DW SE sequence with a BW of 1715 Hz/pixel. A total of 30 slices were acquired in a TR of 6.6 s and with an effective TE of 110 ms. To minimize the influence of eddy currents, a TRSE diffusion preparation [40] was used with b-factors of 0 and $1000\,s/mm^2$. Based on the scanning protocol, the actual diffusion time Δ was estimated to be 50 ms. The resolution was $2\,mm \times 2\,mm \times 2\,mm$.

The diffusion weighted images were used to estimate the DT's by linear regression [43]. The dependency of fibre direction on the DC was determined. Fibre tractography was performed using an adaptive fourth order Runge-Kutta integration algorithm [85].

Evaluation of the effect of susceptibility differences

The PD, T_2 and FA measurements were performed for varying angles between the fibre bundle and B_0-field ($0°$, $15°$, $30°$, $45°$, $60°$, $75°$ and $90°$) to investigate the effect of increasing field gradients. Increasing the angle between fibres and B_0-field will increase the contribution of local field inhomogeneities of the magnetic susceptibility as illustrated in equation (3.1). The increase in the R_2 relaxation rate by internal field gradients with respect to the R_2 in case of parallel alignment of the fibres with the B_0-field, R_{2IG} in equation (3.2), was measured for each angle. R_{2IG} was derived as a measure of the effect on T_2 due to susceptibility differences between fibre material and water.

To evaluate the effect of internal gradients on the diffusion properties, FA-values were measured for both parallel and perpendicular alignment of the fibres with the B_0-field.
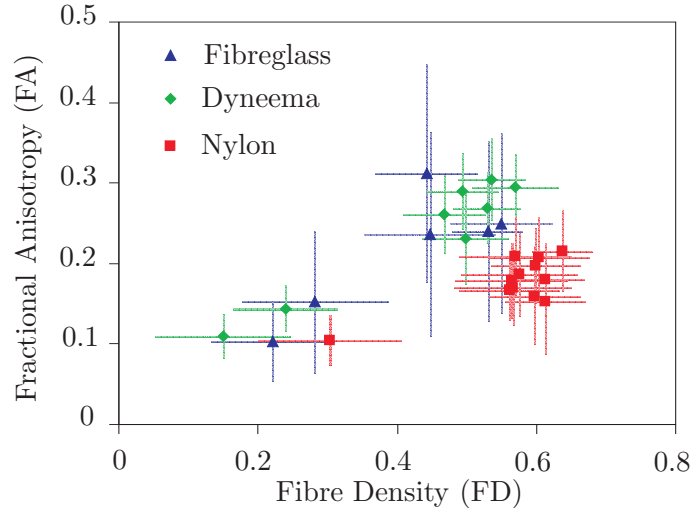
Figure 3.13: Demonstration of the dependency of the measured FA-values on fibre density and fibre radius for each fibre material.

3.5   Results

The radii (mean value and standard deviation) of the fibre materials, as measured with SEM, are presented in table 3.1.

FA, PD and T_2 measurements were performed on the four tested fibre materials. The results are presented below. However, results of the phantoms made of carbon fibre are not described since the signal in these phantoms was too low to be measured with MRI, even at short echo times (TE ≥ 8ms).

FA measurements

In figure 3.13, FA is plotted as a function of the measured fibre density. The error bars of the experimental data show the standard deviation of the FA and FD in pixels of the chosen ROI's within the fibre phantoms. The ROI's were determined by the reconstructed fibre bundle using fibre tractography through each fibre phantom and contained 270 ± 103 voxels. For each fibre material, FA increases with increasing FD. When comparing the FA-values for equal FD, nylon fibre phantoms were found to have a lower FA than fibreglass and Dyneema®.
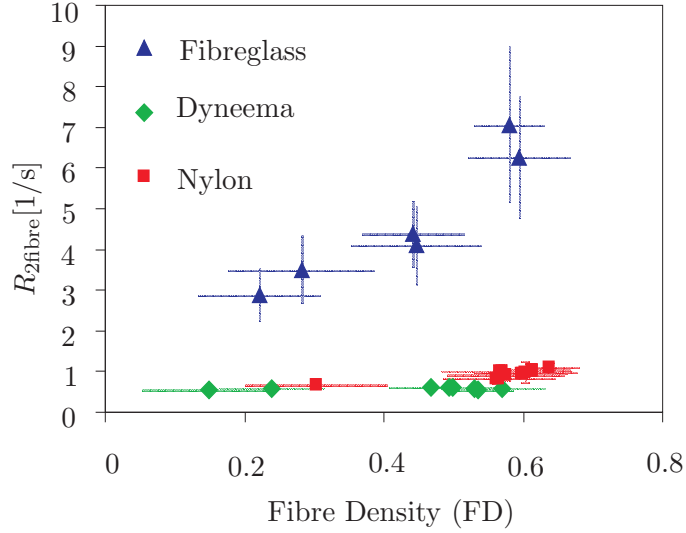
(a)
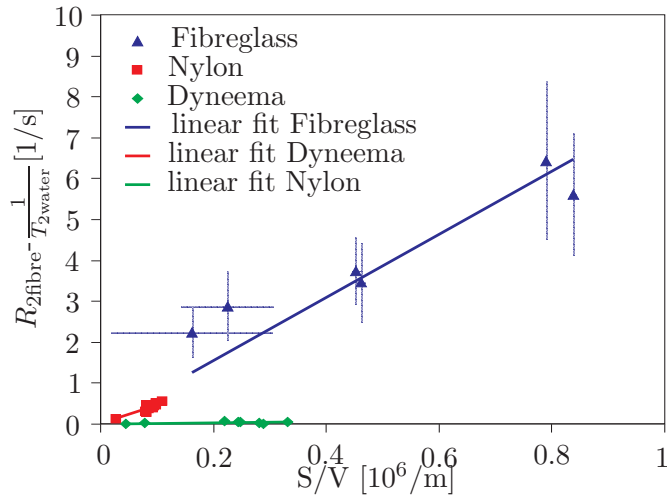
(b)

Figure 3.14: Evaluation of the effect of the surface relaxation by comparison of R_2 for the three tested fibre materials. (a) the change in R_2 is dependent on the fibre density due to different surface relaxivity. (b) R_{2fibre}- $\frac{1}{T_{2water}}$ as a function of the surface to volume ratio (S/V). The surface relaxivity ρ is determined as the slope. T_{2water} was measured to be 0.5 s.

Evaluation of the effect of surface relaxation on the T_2 measurements

The effect of surface relaxation is demonstrated in figure 3.14. Figure 3.14 (a) shows the measured T_2-relaxation rates, R_2, for the different materials with the fibre phantoms aligned parallel to B_0. The error bars show the standard deviation within the chosen ROI's (containing 354 ± 113 voxels). Due to surface relaxation, R_2 increases for increasing fibre density, but the change in R_2 is different for each fibre material. Values for the surface relaxivity ρ were estimated by fitting equation (2.7) to the R_2 versus S/V curve (figure 3.14 (b)) and are presented in table 3.1.

The effect of surface relaxation on the R_2 is also plotted in figure 3.15 by combining equations (3.2) and (3.3). Figure 3.15 (a) shows the increase in R_2 as a function of the fibre density and surface relaxivity for fibre phantoms with a fibre radius of $2 \, \mu$m. R_2 increases for increasing fibre density and surface relaxivity. The effect of the fibre radius on the increase of R_2 due to surface relaxation is illustrated in figure 3.15 (b) for a fibre surface relaxivity of $3 \, \mu$m/s. The increase in R_2 is inversely proportional to the fibre radius for a given fibre density and surface relaxivity.

Evaluation of the effect of susceptibility differences.

The effect of local variations in the magnetic susceptibility on the MR-measurement is demonstrated in figure 3.16.

Figure 3.16 (a) shows the increase in R_2 for increasing angle between the fibre phantoms and $\vec{B}_0$. The effect of susceptibility differences on T_2-relaxation is illustrated here for fibre phantoms of the three materials with a fibre density of about $30\,\%$.

The FA-values plotted in figure 3.13 were measured with the fibres aligned parallel to $\vec{B}_0$. When the fibre phantoms were not aligned parallel to $\vec{B}_0$, diffusion measurements could not be performed for the phantoms made of fibreglass because of the low signal which results from a short T_2-relaxation time ($\leq 100\,$ms). The measured FA-values for the Dyneema® and nylon fibre phantoms in the case of parallel alignment are plotted against the case of perpendicular alignment in figure 3.16 (b), illustrating the negligible effect of field inhomogeneity caused by magnetic susceptibility differences.
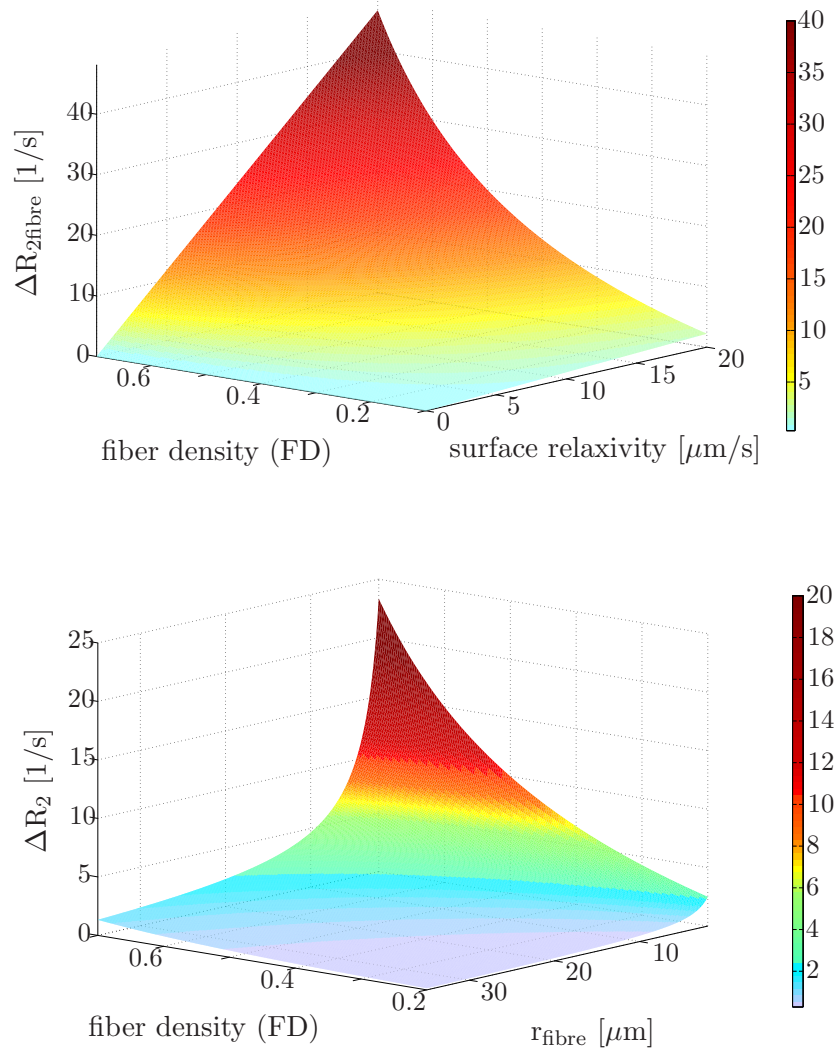
Figure 3.15: The effect of surface relaxation on the R_2. (a) Increase in the R_2-relaxation rate as a function of the fibre surface relaxivity and the fibre density (with a fibre radius of $2\mu m$). (b) Increase in the R_2-relaxation rate for a fibre surface relaxivity of $3\,\mu m/s$ as a function of the fibre density and the fibre diameter.
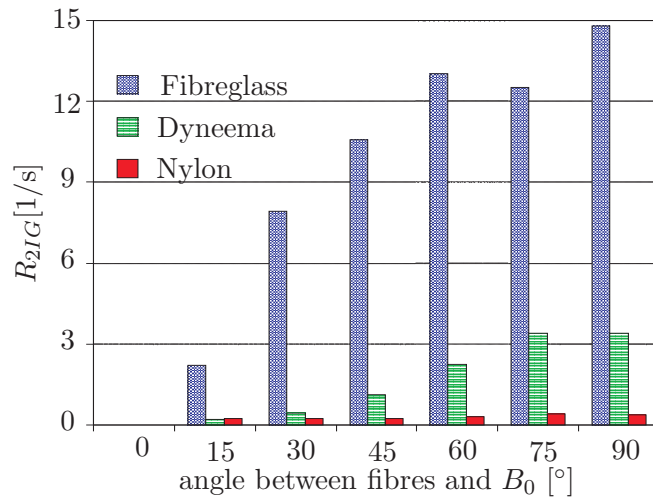
(a)
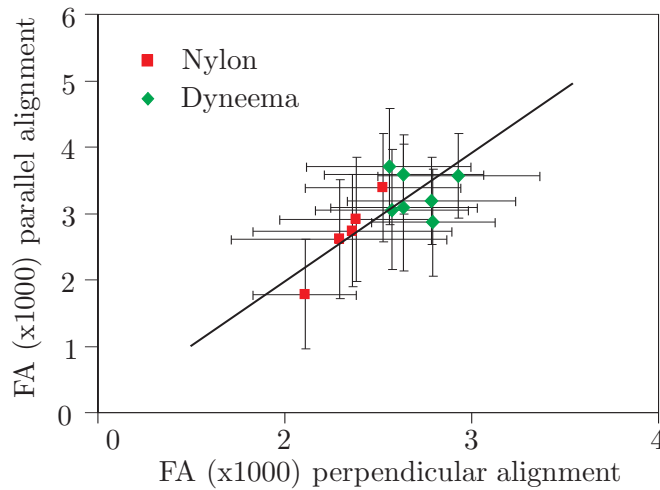
(b)

Figure 3.16: Evaluation of the effect of local field inhomogeneity caused by magnetic susceptibility differences between fibre and water. (a)Change in R_2 as a function of the angle between the fibres and B_0 for three of the tested fibre materials. The increase in R_2 when changing the angle between the fibres and B_0 depends on the magnetic susceptibility of each fibre material and is shown here for phantoms with a fibre density of 30%. (b) Measured FA-values for the Dyneema® and nylon fibre phantoms in the case of parallel alignment versus perpendicular alignment. The solid line denotes the bisector of the first quadrant.

3.6   Discussion

3.6.1   SNR considerations

The SNR of the fibre phantoms is determined by the PD and the T_2-relaxation time of the fibre phantoms. The PD in the fibre phantoms is rather low in comparison to BWM since plain fibres were used for the phantoms whereas the signal in DWI in BWM originates from the water in both the intra- and extracellular space. The loss in signal due to the lower PD can be compensated by choosing a fluid and fibre material with long T_2 in comparison to BWM. As an example: PD of the water in the intra- and extracellular space is about 65% with a T_2 of about 85 ms [11]. To obtain the same signal intensity in fibre phantoms with a PD of 30% at a TE of 100 ms the T_2 of the fibre phantoms should be chosen around 270 ms according to equation (2.7). However, several other factors may affect the T_2-relaxation time in the fibre phantoms such as surface relaxation and susceptibility differences between the fibre and the water.

Surface relaxation

Figure 3.15 clearly demonstrates the strong effect of surface relaxation on R_2 especially for high fibre densities and small fibre radii. As the T_2-value of free water is around 2.5 s at 3T, an appropriate T_2 of minimum 270 ms can be obtained if the increase in R_2 due to surface relaxation is less than $3.3\,\mathrm{s}^{-1}$. The experimental results of figure 3.14 and equations (3.2) and (3.3), illustrated in figure 3.15, both prove that for fibre phantoms with a high fibre density and small radius such a small increase in R_2 is only feasible for fibre materials with a very low surface relaxivity value.

The surface relaxivity values for three of the tested fibres could be derived by fitting equation (3.2) to the measured data (see figure 3.14) showing that Dyneema$^{\circledR}$ has a very low surface relaxivity, while nylon and fibreglass have higher relaxivities (see table 3.1).

The surface relaxivity is a measure for the interactions between fluid and fibre surface: the stronger the interaction, the higher the surface relaxation. Another parameter reflecting the intermolecular interactions between liquid and solid surface is the degree of wetting, which depends on the interface energy (or corresponding surface tensions) involved such that the total energy is minimized. The degree of wetting or wettability is described by the contact angle, i.e. the angle at which the liquid-vapour interface meets the solid-liquid in-
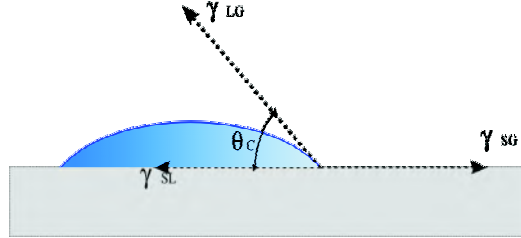
Figure 3.17: The contact angle of a liquid droplet wetted to a rigid solid surface. γ is the surface energy between the two indicated phases (l=liquid, s=solid, g=gas)

terface (see figure 3.17). In case of hydrophilic materials, the wetting is favourable and the contact angle will be low ($< 90°$) so that the fluid will spread to cover a larger area of the surface. In the opposite case of hydrophobic surfaces, the water droplets rest on the surface without actually wetting and the contact angle will be larger than $90°$.

NMR surface relaxation is related to the wettability of a surface for a given liquid [122]. The derived surface relaxivities for the three tested fibre materials are related to the contact angles between fibres. Nylon, fibreglass and carbon are all hydrophilic materials, with low contact angles of $64°$ [123], $37°$ [124] and $45°$ [125], while Dyneema® is highly hydrophobic resulting in a contact angle $> 90°$. Since hydrophobic materials have low surface relaxation, hydrophobic fibres seem most suitable for the fabrication of anisotropic diffusion phantoms.

Local variations in magnetic susceptibility

Another important fibre parameter which influences T_2 is the magnetic susceptibility difference between the fibre material and the water causing inhomogeneous magnetic fields. The total magnetic moment of spins decays faster due to the diffusion in an inhomogeneous magnetic field. The effect of the diffusion on the transverse relaxation time T_2 also depends on the echo time spacing [126].

In the case of perfect parallel alignment of the fibres with the B_0-field, there is no offset of the magnetic field and the field is homogeneous everywhere. When increasing the angle between the fibres and the B_0-field, an inhomogeneous magnetic field results whereby the inhomogeneity increases with increasing angle up to $90°$. This

results in a larger R_2 as shown in figure 3.16 (a).

The effect of different magnetic susceptibilities for different fibre materials is illustrated in figure 3.16 (a). Magnetic susceptibility values found in the literature are -9.02 ppm for water at $20°C$, -16.3 ppm for glass and -204 ppm for carbon [127]. The magnetic susceptibility of Dyneema® is estimated about -10 ppm [128]. Susceptibility values are found for nylon fibres in [129] where, depending on the crystalline ratio, the susceptibility varies between -3 ppm and -6 ppm parallel and -7 ppm and -10 ppm perpendicular to the fibre. The results shown in figure 3.16 (a) are semi-quantitatively supported by the susceptibility values reported in the literature. In addition to a high surface relaxivity, the fact that the water in the carbon fibre phantoms was not visible might also be caused by the very large difference in susceptibility between carbon and water. The second largest magnetic susceptibility difference was for fibreglass which results in the largest R_2 increase in comparison to nylon and Dyneema®.

Quantitative correlation of the theoretical magnetic susceptibility effect with the observed R_2 increase is compromised for the nylon and Dyneema® fibre phantoms because no information is found on the anisotropy of susceptibility for Dyneema® and it is not straightforward to measure because of the small size of the fibres. However, most crystalline fibres are anisotropic and will behave more diamagnetic when placed perpendicular than parallel with the magnetic field. Since for parallel alignment, the susceptibility of Dyneema® is estimated to be more diamagnetic and nylon to be less diamagnetic than water, the difference in magnetic susceptibility can be assumed to increase for Dyneema® and decrease for nylon fibre phantoms with increasing angle between fibres and $\vec{B}_0$. This might explain the higher increase in R_2 for Dyneema® as compared to nylon.

It is concluded that polymer fibres appear to be the most appropriate candidates to make diffusion phantoms in terms of magnetic susceptibility effects. As polymer fibres may have an anisotropic micro structure, it is always advisable to perform T_2-measurements for different angles between fibre and B_0-field to check the anisotropy of the susceptibility. When the fibre susceptibility is isotropic but has a significantly larger magnetic susceptibility than water, the water can be doped with paramagnetic contrast agents to match the susceptibility between fibre and water [130]. In the case of a lower susceptibility of the fibres in comparison with water, the water may also be replaced by another liquid with a closer susceptibility. A list of susceptibility values for organic liquids can be found in [131]. How-

ever, the requirement of using a hydrophobe material will be replaced then by the requirement of using a lypophobe material that should be investigated as well.

3.6.2 Optimization of the FA

Effect fibre radius and fibre density

Fibre phantoms with high FA are preferred since the white matter values of FA are typically of the order of 0.7 (see chapter 2). The degree of diffusion anisotropy is mainly determined by the FD and the fibre radius. As shown in figure 3.13, the highest FA-values were measured for fibres with a high FD and a small fibre radius.

When comparing fibre phantoms of different materials with similar FD, FA is higher for fibreglass and Dyneema$^{®}$ than for nylon fibre phantoms due to the smaller fibre radius.There is a time-dependency of the diffusion process which is related to the fibre diameter and the diffusion time, typically around 50 ms in DW-MRI. The next chapter will discuss in more detail the time-dependent diffusion properties using Monte Carlo simulations of random walk whereby the effect of fibre radius, fibre density and surface relaxation on the FA will be evaluated quantitatively.

Local variations in magnetic susceptibility

In the ideal case of a homogeneous B_0-field, the molecules only see the applied diffusion gradients. However, local differences in magnetic susceptibility in the fibre phantom induce additional internal gradients. The internal gradients can cause undesirable dephasing and rephasing and can compromise the accurate determination of diffusion.

The experimental measured FA-values in figure 3.16 (b) showed no significant difference between the FA-measurements performed with the fibres either parallel or perpendicular to $\vec{B_0}$. The effect of magnetic susceptibility differences between water and fibre on measured FA seems rather small in contrast to the large effect of magnetic susceptibility differences on the T_2-time. The major cause of an inaccurate diffusion measurement will be the noise caused by the short T_2 decay time in case of local magnetic susceptibility inhomogeneity.

3.7   Conclusion and original contributions

This chapter started with a classification of hardware diffusion phantoms. Isotropic liquids have a well-known diffusion coefficient and can be used in quality protocols assessing the accuracy and precision of the ADC. In order to evaluate anisotropic diffusion parameters such as the FA and fibre orientation, anisotropic fibre phantoms become indispensable. Among plants, monocots exhibit anisotropic diffusion and especially the asparagus may serve as a useful test object during sequence design. Biological phantoms made of excised spinal cord are interesting to test diffusion models because they come close to the *in vivo* situation. However, biological phantoms fail for calibration purposes because of their limited storage time and the fact that their exact structure often remains unclear. Synthetic anisotropic fibre phantoms are proposed recently to overcome these issues. Moreover, they can be used to create complex geometries such as curved fibres and fibre crossings.

Anisotropic fibre phantoms are suitable and reproducible test objects that can be useful for the validation of DW-MRI on clinical MR-scanners. The fibre density and fibre diameter are two important factors that determine the diffusion properties such as FA, while the SNR is determined by the surface relaxation and the magnetic susceptibility through their effect on the T_2 relaxation. The most appropriate fibre bundles to mimic diffusion measurements in brain white matter are densely packed fibres made from a hydrophobic material with a magnetic susceptibility close to water.

With respect to SNR from the four materials discussed in this chapter, Dyneema$^{®}$ is found to give the best performance because of its lowest surface relaxation. When placing the fibres perpendicular to the B_0-field, nylon fibre phantoms produce the best SNR because the magnetic susceptibility of nylon is closest to water. Dyneema$^{®}$ and fibreglass have the highest FA-values because of their small fibre radius. Overall for the tested materials, Dyneema$^{®}$ is the most suited fibre material for testing DW-MRI because of the combination of a high FA and a reasonable SNR. In the next chapter, we use this fibre to validate the diffusion within the fibre phantoms quantitatively.

In order to create more realistic phantoms imitating the diffusion in both intra- and extracellular space of BWM, one might consider the use of capillaries. The same criteria about fibre surface relaxivity and susceptibility influencing the T_2 as described above for plain fibres are valid when choosing appropriate fibre materials in this case. The ideal

fibre would be hollow with a small fibre diameter ($< 10\,\mu$m) and a magnetic susceptibility close to water (-9 ppm). To our knowledge, there are no such capillaries available at the moment.

4

Simulation and experimental verification of the diffusion in the interstitial space of a fibre phantom

4.1   Introduction

In the previous chapter, we have demonstrated that anisotropic fibre phantoms show to be useful test objects for the validation of DW-MRI. However, an accurate description of the phantom geometry and also of the diffusion behaviour is essential to use them as the ground-truth for the quantitative validation of diffusion parameters. In this chapter, we analyse in detail the diffusion process inside the anisotropic fibre phantoms.

To enable quantitative evaluation of the measurements, the diffusion is modelled in the interstitial space of the fibre phantom by Monte Carlo (MC) simulations of random walkers. In addition, the diffusion profile and excess kurtosis are extracted. The influence of the fibre packing density and ordered versus random packing geometry on the diffusion behaviour is examined in a regime extending from the short-time to the long-time diffusion limit. Also the effect of surface relaxation is addressed.

The anisotropic fibre phantoms constructed in this work can be regarded as 2D porous media. Simulation results can be compared

with the analytical equations derived for diffusion in porous media. The validation of these theoretical models has already been demonstrated for porous media in three dimensions with random packed beads [132, 133] and various types of porous rocks [134, 135]. In this chapter we compare the simulation and experimental results with the analytical models for diffusion within porous media in two dimensions.

4.2   Theory of diffusion in porous media

A porous medium is an impermeable matrix permeated by an interconnected network of pores filled with an MR-visible fluid. Porous media are found in nature, e.g. rocks, soils and biological tissue such as bone, but also in man-made materials such as foams and ceramics. The properties of porous media have been studied for several applications such as petroleum engineering, geophysics, well logging, material science and biophysics.

The fibre phantoms in this study can be considered as two dimensional porous media with a matrix consisting of an infinite pack of cylinders. The developed theory for diffusion in porous media can thus be applied to model the diffusion inside the fibre phantoms. The time-dependent properties of the ADC are reasonably well understood in porous media [133, 135–140].

Three different regimes in the time-dependent ADC(Δ) can be distinguished: a short-time diffusion regime, a long-time diffusion limit and a transition region in between. These regimes also depend on the diffusion direction. Each time region will be described in more detail.

4.2.1   Short-time diffusion regime

In the case of diffusion in a short-time, the mean diffusion length $l_d = \sqrt{D_0 \Delta}$ remains smaller than the typical pore size so that only the molecules located in a layer with a thickness of the order l_d can sense the presence of the surface [132, 136, 137]. This implies that the diffusion behaviour is determined by the surface-to-volume ratio S/V (see figure 4.1). For fibre phantoms, modelled as infinitely long cylinders, the ADC in the direction perpendicular to the infinitely long cylinders decays in the short-time diffusion regime according to
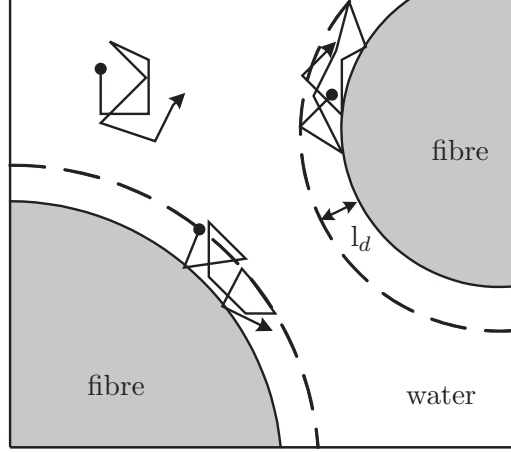
Figure 4.1: Illustration of the dependency of the diffusion coefficient on $\sqrt{D_0\Delta}$: at short diffusion times, only water molecules in a surface layer with a thickness equal to $l_d = \sqrt{D_0\Delta}$ are sensitive to the restriction created by the fibre walls. This water fraction equals $\frac{S}{V}\sqrt{D_0\Delta}$.

the following formula:

$$\frac{ADC(\Delta)}{D_0} = 1 - \frac{2}{3\sqrt{\pi}}\frac{S}{V}\sqrt{D_0\Delta} + O(D_0\Delta), \qquad (4.1)$$

with D_0 the diffusion coefficient in a free medium and $O(D_0\Delta)$ the rest term including the higher order terms proportional to $\sqrt{D_0\Delta}^2$, $\sqrt{D_0\Delta}^3$, ...

As S/V depends on the fibre density and fibre radius according to equation (3.3), the diffusion in the short-time regime becomes dependent on both parameters.

Surface relaxation

The term proportional to $\sqrt{D_0\Delta}$ in equation (4.1) is not affected by surface relaxation [137]. But when the diffusion time is increased, the higher order terms in $\sqrt{D_0\Delta}$ start to play a role. For smooth interfaces, the term proportional to $D_0\Delta$ is the following [137]:

$$-\frac{1}{8}H\frac{S}{V} + \frac{1}{4}\frac{\rho S}{D_0 V}, \qquad (4.2)$$

where H is the mean curvature averaged over the surface, which in the case for fibre phantoms equals:

$$H = \langle \frac{1}{r_{\text{fibre}}} \rangle. \tag{4.3}$$

According to equation (4.2), the term proportional to $D_0 \Delta$ causes an increase in the ADC(Δ) only when ρ is large enough. The ADC is relatively insensitive to surface relaxation at short diffusion times and can thus be neglected in most cases [137].

4.2.2 Long-time diffusion limit

In the other extreme limiting case of long diffusion times, the molecules can travel distances much longer than the pore size and thus probe the connectivity of the pore space. When ignoring the relaxation of molecules at the surface, the diffusion profile can be considered to be pseudo-Gaussian and the diffusion coefficient becomes independent of the diffusion time Δ and is expressed as a function of the tortuosity parameter Λ [132] according to:

$$\frac{ADC(\Delta \to \infty)}{D_0} = \frac{1}{\Lambda} + \frac{\mu_1}{\Delta} + \frac{\mu_2}{\Delta^{3/2}}, \tag{4.4}$$

where μ_1 and μ_2 are constants depending on the details of the geometry.

The tortuosity Λ is a property of the medium, i.e., the geometry and the connectivity of the pores. In general, its relation to the medium is not very clear.

The role of tortuosity in transport processes

Through the tortuosity, the diffusion coefficient is strongly related to many transport mechanisms confined in porous media such as the permeability, the electrical conductivity, the heat conductivity and the velocity of sound [132]. For a given pore geometry made of an insulating rigid homogeneous porous matrix containing a conducting fluid, the problem of electrical conductivity is equivalent to that of the diffusivity in this medium. An analogous problem is also that of the hydrodynamics of an ideal fluid moving in the same pore space, in the long-wavelength (incompressible fluid) limit [141]. Brown [141], Johnson et al [142] and Sen et al [143] noticed the fact that the microscopic and differential equations and boundary conditions governing the transport processes are identical in all those cases.

Electrical Conduction		Diffusion
$\vec{j}_e = -\sigma_0 \nabla \Phi$	microscopic equation	$\vec{j}_d = -D_0 \nabla c$
$\nabla^2 \phi = 0$	differential equation	$\nabla^2 c = 0$
$\vec{j}_e . \vec{n}_w = 0$	boundary equation	$\vec{j}_d . \vec{n}_w = 0$
$\vec{I}_e = \left[\iint (\vec{j}_e . \vec{n}) dA \right] \vec{n}$	definition	$\vec{I}_d = \left[\iint (\vec{j}_d . \vec{n}) dA \right] \vec{n}$
$\vec{I}_e = -\frac{A}{F} \sigma_0 \langle \nabla \Phi \rangle$	macroscopic solution	$\vec{I}_d = -\frac{A}{F} D_0 \langle \nabla c \rangle$

Table 4.1: Equivalence between the problem of electrical conductivity of a nonconducting porous matrix containing a conducting pore material and that of the diffusivity in this medium. All quantities have their usual meanings; $\vec{j}_e$ is the electrical flux density and $\vec{j}_d$ diffusion flux, Φ the electrical potential, c the concentration, $\vec{n}_w$ is a unit vector normal to the pore-matrix interface, $\vec{n}$ is a unit vector normal to a flat surface of area A over which the integration is performed. $\vec{I}_e$ represents the electrical current and $\vec{I}_d$ the diffusion flow rate trough an area A. The fact that both problems are described by the same equations and boundary conditions yields equations (4.5) and (4.6) of the text. More details are given in [141, 142].

A summary of this proof is given in table 4.1 for the problem of electrical conductance and diffusion. The quantity F, defined by the last entries in table 4.1 is a scalar for statistically homogeneous, isotropic samples. Inasmuch as the two problems are equivalent, the same value of F applies for the two problems for a given sample. Sen et al [143] have shown, in effect that

$$\frac{ADC(\Delta \to \infty)}{D_0} = \frac{1}{\Lambda} = F\phi, \qquad (4.5)$$

$$\frac{\sigma}{\sigma_0} = F, \qquad (4.6)$$

where ϕ is the porosity of the medium. These equations hold only of the matrix material is nonconducting and there is no interfacial surface relaxivity. The extra factor of ϕ for D in equation (4.5) comes from the fact that concentration enters into a transport problem involving diffusion [142] and not one involving electrical conduction.

From equations (4.5) and (4.6), we derive the following relation between the tortuosity and electrical conductivity of a given porous medium:

$$\frac{1}{\Lambda} = \frac{\sigma}{\sigma_0} \phi. \qquad (4.7)$$

Following descriptions for the tortuosity Λ are adopted from theories describing electrical conductivity:

- Archie's law

  Archie's law [144] was originally derived for impedance measurements and adapted for diffusion in porous media [138, 145]. This law suggests a correlation of Λ with the porosity ϕ, i.e., the fraction of the interstitial space (1-FD) with FD the fibre density, according to

$$\Lambda = \phi^{-\beta}. \tag{4.8}$$

  β depends on the packing geometry and usually lies in the range 1/2 to 2/3 [145]. For random spheres, β equals 1/2 [132, 133, 139, 146].

- Maxwell-Garnett formulas

  The transport properties between cylinders were discussed in [147] where the method used by Lord Raleigh is elaborated for square and hexagonal packings of cylinders, resulting in specific Maxwell-Garnett formulas. Also, the Maxwell-Garnett formulas for the tortuosity derived in [143] for hollow cylinders with a given thickness can be simplified to the situation for filled cylinders (with no water molecules inside the cylinders).

  When using polar coordinates the electrical potential Φ in each point can be expanded in a series of cos-terms. The unknown coefficients in this series are obtained by taking into account the boundary conditions and truncation of the series. To the lowest order in the multipolar expansion, the Maxwell-Garnett formula results in an equation for the tortuosity for both hexagonal and square packed cylinders:

$$\frac{1}{\Lambda} = \frac{1}{2 - FD}. \tag{4.9}$$

  When taking into account higher order terms, some coefficients are omitted depending on the specific geometry of the ordered packing. For hexagonal packed cylinders, the analytical expression for σ is derived in [147] when truncating the Maxwell-Garnett to the fourth order, which results in the following tortuosity:

$$\left[\frac{1}{\Lambda}\right]_H = \frac{1 - 2FD\left(1 + FD - \frac{0.075422FD^6}{1 - 1.060283FD^{12}} - 0.000076FD^{12}\right)^{-1}}{1 - FD}.$$

(4.10)

An analogous derivation for square packed cylinders when truncating the Maxwell-Garnett formula to the third order [147] gives then the following tortuosity:

$$\left[\frac{1}{\Lambda}\right]_S = \frac{1 - 2FD\left(1 + FD - \frac{0.305827FD^4}{1 - 1.402958FD^8} - 0.013362FD^8\right)^{-1}}{1 - FD}.$$

(4.11)

In the next section 4.3, we describe how MC random walk simulations can be used to derive $ADC(\Delta)$ in porous media with ordered and random 2D fibre geometries. In particular, the correspondence with Archie's law and the Maxwell-Garnett formulas in the long-time diffusion limit is investigated.

Surface relaxation

Due to surface relaxation, water molecules get absorbed at the pore-fibre surface resulting in loss of magnetisation. While the diffusion is relatively insensitive to surface relaxation in the short-time, its effect increases with Δ since more water molecules get absorbed. The absorption of water is caused by the enhanced surface relaxation due to a high interaction between the fluid and fibre material as explained in section 3.6 of the previous chapter. As the measured diffusion coefficient with MRI is an average based on the remaining magnetisation, surface relaxation may alter the diffusion coefficient in the long term.

The effect of surface relaxation in porous media in the long term is studied in [148] for ordered and disordered sphere packing geometries. In porous media containing "'dead-end"' channels, it is shown that the effective diffusion coefficient due to surface relaxation may be larger than the diffusion coefficient in case of no surface relaxation. However, in most systems, including the cylinder packings considered here, the opposite trend can be expected. The surface relaxation limits the diffusion in systems containing relatively large pores connected by narrow throats since the magnetisation of water molecules diffusing in those narrow channels is efficiently eliminated

because of surface relaxation. A decrease of the ADC(ρ) is expected
to be linear with ρ according to the formula:

$$ADC(\rho) = ADC(0)\left[1 - \frac{\rho L}{ADC(0)}\right], \qquad (4.12)$$

with L a typical length scale. L increases with decreasing porosity ϕ
or with increasing fibre density FD.

4.2.3 Transition between short-time diffusion regime and long-time diffusion limit

Padé interpolation

A general analytical equation for ADC(Δ) does not exist. However,
one can interpolate between the short- and long-time equations, (4.1)
and (4.4), for the $ADC(\Delta)$ using a Padé-approximant description. A
Padé approximant is the best approximation of a function $f(x)$ by a
rational function $R(x)$ of given order (m,n):

$$R(x) = \frac{p_0 + p_1 x + p_2 x^2 + \ldots + p_m x^m}{1 + q_1 x + q_2 x^2 + \ldots + q_n x^n}. \qquad (4.13)$$

Using a two-point Padé approximant, one can interpolate the follow-
ing function between the short- and long-time diffusion limit:

$$\frac{ADC(\sqrt{D_0 \Delta})}{D_0},$$

by fulfilling the following conditions in the two points $\Delta = 0$ and
$\Delta \to \infty$:

$$\begin{aligned}
R(0) &= 1, \\
R'(0) &= -\frac{2}{3\sqrt{\pi}}\frac{S}{V}, \\
R(\infty) &= \frac{1}{\Lambda}.
\end{aligned}$$

The simulation results summarized in section 4.3.2 reveal that the
transition of the ADC from the short-time to the long-time diffusion
limit depends both on the packing geometry and packing density.
When a Padé approximation consisting of the ratio of two first-order
polynomials is considered, the different time-dependencies between
different geometries can not be incorporated in the approximation.

The following equation, based on a two-point Padé approximation of the second order, has been widely used to interpolate between the short-time and the long-time limit [132, 133, 140]:

$$\frac{ADC(\Delta)}{D_0} = 1 - (1 - \frac{1}{\Lambda})\frac{\frac{2}{3\sqrt{\pi}}\frac{S}{V}\sqrt{D_0\Delta} + (1 - \frac{1}{\Lambda})\frac{D_0\Delta}{D_0\theta}}{(1 - \frac{1}{\Lambda}) + \frac{2}{3\sqrt{\pi}}\frac{S}{V}\sqrt{D_0\Delta} + (1 - \frac{1}{\Lambda})\frac{D_0\Delta}{D_0\theta}},$$

(4.14)

with θ a time constant defined by the Padé length ($\sqrt{D_0\theta}$). The Padé length is the length scale during which the diffusion process of a particle converts from the short diffusion time limit to the long diffusion time limit.

Anomalous diffusion

The diffusion in disordered media is anomalous as described in section 2.3.1 of chapter 2, meaning that the mean-square displacement r_{rms}^2 is not linear proportional to the diffusion time. At short and intermediate diffusion time, a porous medium can be considered as a disordered medium with anomalous diffusion behaviour. At very short times, the diffusion is not restricted and thus normal. Also at long diffusion times, a porous medium can be regarded as an homogeneous medium with normal diffusion behaviour. Hence, the diffusion in porous media is normal in the very short- and long-time diffusion limit and can be considered anomalous for the transition period between those limits. The crossover time is then the diffusion time at which the crossover from anomalous to normal diffusion occurs [18].

In the next section, we investigate with MC random walk simulations the time-dependency of the diffusion coefficient, in particular in the intermediate diffusion time. The validity of the Padé approximant and the description of anomalous diffusion are investigated using the simulation results.
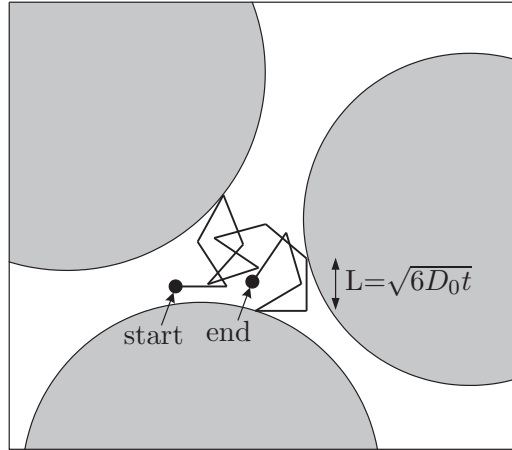
Figure 4.2: Illustration of the random walk in 3D. During each time step t, a particle moves over a distance L according to the Einstein equation.

4.3 Random walk simulations of the diffusion in the interstitial space

4.3.1 Methods

The random displacement of water molecules in synthetic fibre phantoms is simulated by a three-dimensional MC simulation of random walkers.

For each simulation, particles were initially randomly spread in a square plane of $1\,\text{mm} \times 1\,\text{mm}$, which was oriented transverse with respect to the fibre direction in a packing of infinitely long parallel aligned impermeable rigid cylinders. The trajectory of one spin particle was generated by moving the particle during each time step t over a distance of L in a randomly chosen direction with L according to the Einstein equation (2.14):

$$L = \sqrt{6D_0 t}, \tag{4.15}$$

where D_0 is the diffusion coefficient of water in a unrestricted medium. The random direction was selected using spherical coordinates by choosing the radial coordinate r, the azimuthal angle θ and the polar angle ϕ according to:

$$r = \sqrt{6D_0 t},$$

$$\theta = 2\pi u,$$

$$\phi = \arccos(1 - 2v),$$

with u and v numbers generated randomly between 0 and 1 according to a uniform probability distribution.

At the cylinder boundaries, water molecules were elastically reflected. Multiple reflections of the water molecules between multiple cylinders were enabled. Figure 4.2 illustrates the random walk process.

In the direction along the cylinders, the particles can travel infinitely long. In the transverse direction, random walkers that reach the border of the $1\,\mathrm{mm} \times 1\,\mathrm{mm}$ square, re-enter again at the opposite side of the square. The packed cylinders are distributed in the square such that a continuous geometry is obtained when the square is repeated periodically in both orthogonal directions. For each random walker, the number of times that it leaves and enters the square at each side is recorded so that for a given diffusion time Δ, the total travelled distance is calculated correctly. The first and higher-order moments of the total travelled distance in the x-, y- and z- directions are used to calculate the apparent diffusion coefficient ADC and the apparent diffusion kurtosis ADK according to the corresponding definitions, equations (2.14) and (2.16), as:

$$ADC(\Delta) = \frac{1}{2\Delta} \left\langle \left(\vec{n} \cdot \vec{s} \right)^2 \right\rangle, \qquad (4.16)$$

$$ADK(\Delta) = \frac{\left\langle \left(\vec{n} \cdot \vec{s} \right)^4 \right\rangle}{\left\langle \left(\vec{n} \cdot \vec{s} \right)^2 \right\rangle^2} - 3, \qquad (4.17)$$

where $\vec{s}$ is the net displacement of a particle during a diffusion time Δ and $\vec{n}$ is the considered direction.

Diffusion tensor and fractional anisotropy

In the case of a packing geometry of infinitely long parallel packed cylinders, we expect that the principal frame of reference of the diffusion tensor coincides with the axes of a coordinate system chosen according to the three orthogonal directions x, y and z with the z-direction parallel to the cylinders. This hypothesis is confirmed in [103, 143] and experimentally verified by the simulation results, which proves that the diffusive motion parallel and perpendicular to the cylinders are statistically independent. Moreover, it is found that

the diffusion coefficient is the same in all directions perpendicular to the cylinders.

The apparent diffusion coefficients in the x, y and z-direction are thus the eigenvalues of the diffusion tensor. The DT is then given by:

$$DT = \begin{bmatrix} ADC_Z & 0 & 0 \\ 0 & ADC_X & 0 \\ 0 & 0 & ADC_Y \end{bmatrix}. \tag{4.18}$$

The FA, equation (2.30), is thus described by:

$$FA = \frac{\sqrt{(ADC_Z - ADC_X)^2 + (ADC_Z - ADC_Y)^2 + (ADC_X - ADC_Y)^2}}{\sqrt{2}\sqrt{ADC_Z^2 + ADC_X^2 + ADC_Y^2}}. \tag{4.19}$$

Surface relaxation

The effect of surface relaxation was incorporated in the MC simulation of random walk. In the case of no surface relaxation ($\rho = 0$), there is complete elastic reflection at the cylindrical surface of the fibre. For $\rho \neq 0$, if a water molecule hits the surface during the random walk, its magnetisation is destroyed with a probability γ per unit time step t. By destroying its magnetisation, the specific water molecule becomes MR invisible and does not contribute to the calculation of the diffusion parameters. In [148, 149], the following equation between γ and ρ is presented for the case of weak surface relaxation ($\gamma \ll 1$):

$$\rho = \frac{\epsilon}{6t}\gamma. \tag{4.20}$$

Taking into account the relation between the step length L and timestep t described by equation (4.15) results in the following relation between γ and ρ:

$$\rho = \sqrt{\frac{D_0}{6t}}\gamma. \tag{4.21}$$

Accuracy and precision

The accuracy and precision of the simulated diffusion coefficient and kurtosis are assessed by considering the simulated ADC and ADK in the z-direction. Since the diffusion is not restricted in this direction, the diffusion coefficient should equal the diffusion coefficient in a free medium D_0 and the kurtosis should be zero.

For a simulation in a given fibre packing geometry, the average μ and the standard deviation std of the ADC_Z and ADK_Z were calculated over the simulated time-interval. The accuracy and precision of the simulation of the ADC were evaluated by considering the following parameters:

$$\text{accuracy} \quad = \quad \frac{\mu(ADC) - D_0}{D_0}, \tag{4.22}$$

$$\text{precision} \quad = \quad \frac{std(ADC)}{\mu(ADC)}. \tag{4.23}$$

Similar parameters were derived for the accuracy and precision of the simulation of the ADK:

$$\text{accuracy} \quad = \quad \mu(ADK), \tag{4.24}$$

$$\text{precision} \quad = \quad std(ADK). \tag{4.25}$$

- Precision

  The number of simulated particles determines the precision of the simulated results.

  In the case of no surface relaxation ($\rho = 0$), simulations were performed for 100,000 random walkers. In the case of surface relaxation ($\rho \neq 0$), the number of random walkers decreases with increasing time, which will influence the precision of the simulation. The decrease of number of random walkers depends on the surface-to-volume ratio S/V determined by the fibre density and fibre radius according to equation (3.3). For each ρ, fibre density and fibre radius, the initial number of particles was determined so that still 50,000 particles were retained at the final diffusion time Δ.

- Accuracy

  The accuracy of the simulation is mainly determined by the step length of the random walk simulations.

  The effect of decreasing step length was simulated for random packing geometries of cylinders with a diameter of $20\,\mu$m with different fibre densities. The number of random walkers was 50.000. The results are shown in figure 4.3. Decreasing the step length in the simulations results in a slight increase of the diffusion coefficient (and a decrease of the kurtosis) for high fibre densities. E.g., for a step length of 1.6 μm, the simulated
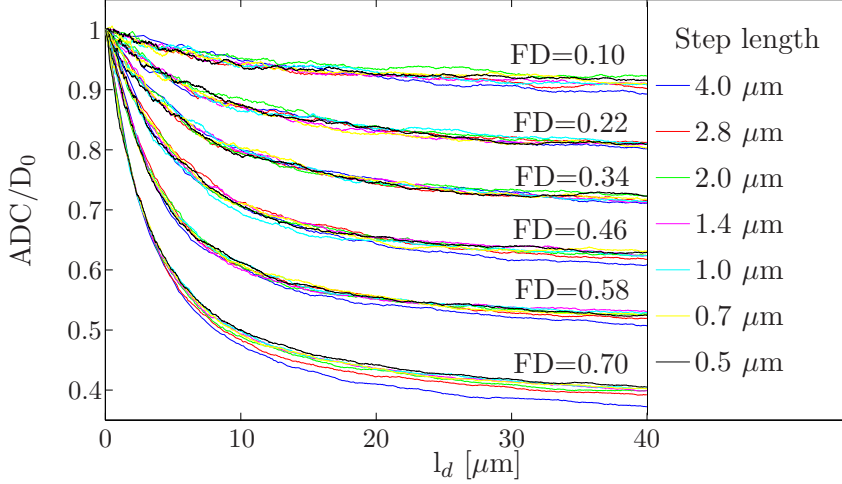
Figure 4.3: Simulation results of the apparent diffusion coefficient in the x-direction for randomly packed cylinder geometries with a diameter of 20 μm and different fibre densities for varying step length (4 μm, 2.8 μm, 2 μm, 1.4 μm, 1 μm, 0.7 μm, 0.5 μm.)

ADC_X and ADK_X differ in average $0.5\,\%$ and $5\,\%$ or less from the ADC_X and ADK_X simulated with the smallest step length of $0.5\,\mu$m.

The time step t of further simulations was chosen so that the corresponding step length $\sqrt{6D_0 t}$ was smaller than $\frac{r_{\text{fibre}}}{10}$. Using this step length results in accurate simulation results without unnecessary prolonging the simulation time given the fact that the simulation time increases quadratically with decreasing step length.

Performed simulations

All simulations were performed for a phantom temperature of $20^\circ C$ ($D_0 = 2.023 \times 10^{-3}\,\text{mm}^2/\text{s}$ [30]).

1. *Simulation of the time-dependent ADC*

   Simulation of $ADC(\Delta)$ to verify the theory for diffusion in porous media, as described in section 4.2. In addition, these simulations were used to validate the diffusion measurements in the fibre bundles as described further in section 4.4.
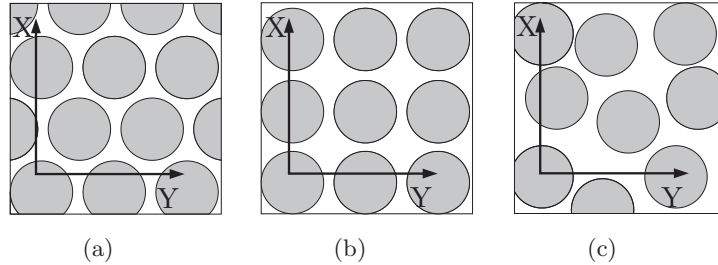
Figure 4.4: *The different types of fibre packing geometries and the corresponding coordinate axes used in the MC simulations: (a) hexagonal, (b) square, (c) random.*

2. *Simulation of the time-dependent ADK*

   These simulations were also used to validate the diffusion measurements in the fibre bundles (see further in section 4.4).

   For the study of both the ADC and ADK, simulations were performed in fibre packing geometries of parallel aligned cylinders with a diameter of $20\,\mu$m and for a free diffusion length l_d of $50\,\mu$m, corresponding to a Δ of $1.3\,$s. Following aspects were investigated:

   - Effect of the fibre geometry
     Ordered (hexagonal, square) and random packing geometries of parallel aligned cylinders were studied (see figure 4.4).

   - Effect of the variation of the fibre radius
     The effect of variations of the fibre radius within one packing was investigated by generating random packing geometries containing cylinders with a fixed diameter of $20\,\mu$m and comparing these simulation results with those obtained in random packing geometries containing cylinders with a Gaussian distributed diameter of $20\,\mu$m $\pm$ $4.1\,\mu$m (standard deviation).

   - Effect of the fibre density
     The effect of fibre density was investigated by increasing the density in steps of 0.04 starting from 0.02 up to the closest possible fibre packing.

Ordered packing geometries with varying fibre density (FD = 0.02, 0.06, ...) were obtained by generating hexagonal and square grids whereby the distance between neighbouring grid points, representing the centre point of the cylinders, was narrowed down to the most dense packing (0.91 for a hexagonal and 0.785 for a square packing). For these simulations, the cylinders had a fixed diameter of $20\,\mu$m.

Homogeneously randomly packed fibre geometries were produced by random generation of a given number of circles in a square ($1\,$mm $\times$ $1\,$mm), whereby the circles were not allowed to overlap. For cylinders with a variable diameter, the order of the placement of circles was chosen according to decreasing circle diameter such that the highest feasible packing density was obtained. The highest fibre density that could be achieved within a reasonable calculation time was 0.54 for the simulations with a constant diameter of $20\,\mu$m and 0.7 for the simulations with a variable diameter of $20\,\mu$m $\pm$ $4.1\,\mu$m.

- Effect of fibre clustering

  In the previous chapter, we demonstrated that hydrophobic fibre materials show the best performance to be used as diffusion phantoms. Due to the hydrophobic nature of the fibre, clustering of the fibres in the phantoms can be expected.

  To model the diffusion in the fibre bundles appropriately, the effect of clustering has been investigated. Clustered packing geometries were generated whereby the fibres were densely grouped together in randomly chosen circular clusters. An example of a clustered packing geometry is shown in figure 4.5. The overall fibre density of the packing geometries was 0.18, 0.26, 0.34, 0.42 and 0.5. Simulations were performed in the clustered geometries for 50.000 particles and compared to the simulations performed in homogeneously randomly packed geometries with a similar overall fibre density.

- Effect of surface relaxation

  Simulations were performed in case of no surface relaxation ($\rho = 0\ \mu$m/s) and in case of a surface relaxation with $\rho = 3\ \mu$m/s.

<div align="center">(a)   (b)</div>
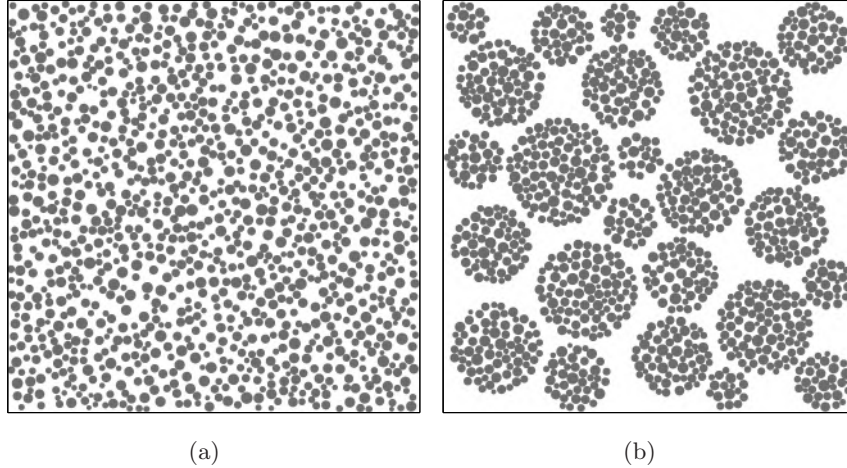
Figure 4.5: Two packing geometries with an overall fibre density of 0.42. (a) homogeneously packed (b) packed in clusters

3. *Simulation of the fractional anisotropy (FA)*

   FA-values are derived from the simulated diffusion coefficients according to equation (4.19). The FA-simulations were performed to explain the experimental results described in the previous chapter and further in section 4.4.2. Simulations were performed in random packing geometries for a Δ of 50 ms while investigating the following:

   - Effect of fibre radius
     The effect of the fibre radius was examined by increasing the mean fibre radius r_{fibre} from 2 μm up to 40 μm in steps of 2 μm.

   - Effect of fibre density
     The effect of the fibre packing density was examined by increasing the fibre density from 0.1 up to 0.7 in steps of 0.04.

   - Effect of surface relaxation
     The effect of surface relaxation was evaluated by increasing the surface relaxivity from 0 μm/s up to 20 μm/s.

fibre packing geometry	accuracy	precision
Hexagonal	0.30%	0.51%
Square	-0.41%	0.42%
Random	0.11%	0.21%

Table 4.2: The accuracy and precision of the simulation of ADC_Z calculated according to equation (4.22) and (4.23)

4.3.2   Results

4.3.2.1   Simulation results of the apparent diffusion coefficient (ADC)

- **Precision and accuracy**

  Figure 4.6(a) shows the ADC obtained from the MC-simulations in the z-direction (along the cylinder) for the hexagonal packing arrangement. In this direction the ADC equals the diffusion coefficient of a free medium and is independent from diffusion time or packing density. ADC_Z was also found to equal D_0 for the square and random packing geometries. The calculated values for the accuracy and precision of the simulation of the ADC are presented in table 4.2. There is some variation in the accuracy between the different fibre pakcing geometries. However, for each fibre geometry, the accuracy value is smaller than the precision value and thus acceptable.

- **Effect of fibre geometry and fibre density**

  The ADC in the x-direction (perpendicular to the cylinder direction) is shown for a hexagonal packing (figure 4.6(b)), a square packing (figure 4.7(a)) and random packing (figure 4.7(b)) as a function of l_d and FD. Within the confidence levels as determined in the accuracy and precision study, the ADC was found to be identical in both the x- and the y-direction.

- **Effect of variation of the fibre radius**

  The simulated ADC for the random packing geometries with a fixed diameter were similar to the results for a random packing with a variable diameter. Hence, the results are not shown here.

- **Time dependency:**

  When looking at the ADC in the transverse plane as a function of the diffusion length l_d ($\sqrt{(D_0\Delta)}$, a short-time diffusion
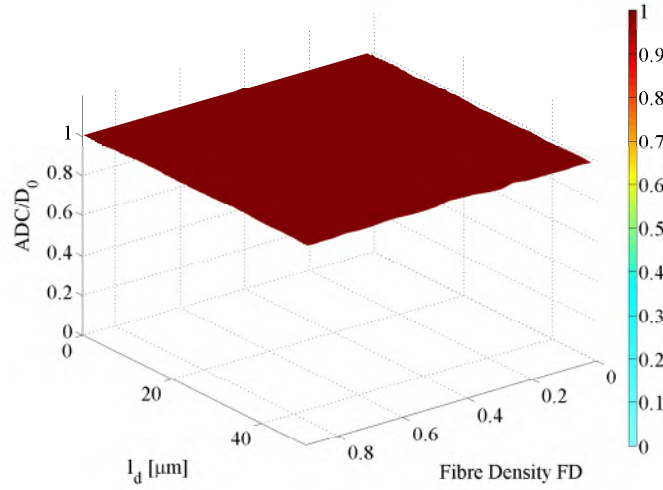
(a) z-direction, hexagonal fibre geometry
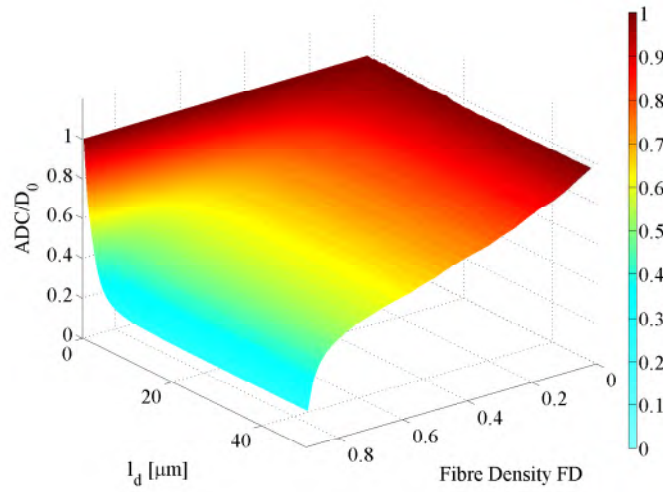
(b) x-direction, hexagonal fibre geometry

Figure 4.6: Simulation results of the apparent diffusion coefficient (ADC). (a) ADC_Z/D_0, i. e. the simulated relative diffusivity in the longitudinal direction, is similar for the three tested packing densities and shown for a hexagonal fibre geometry as a function of l_d and FD. (b) ADC_X/D_0, i.e. the simulated relative diffusivity in the transverse plane, for a hexagonal fibre geometry as a function of l_d and FD.
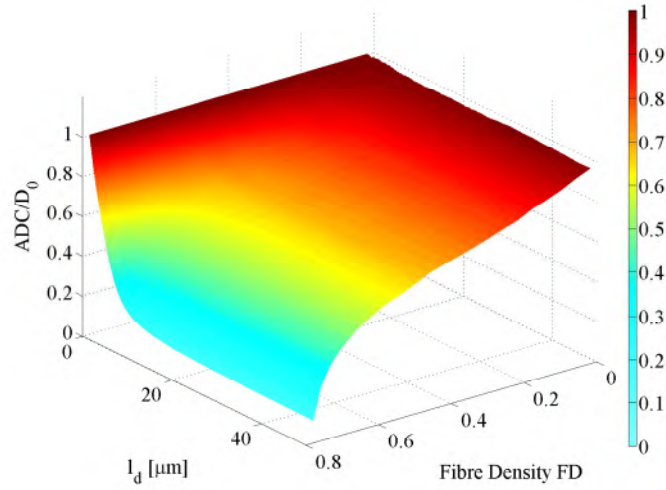
(a) x-direction, square fibre geometry
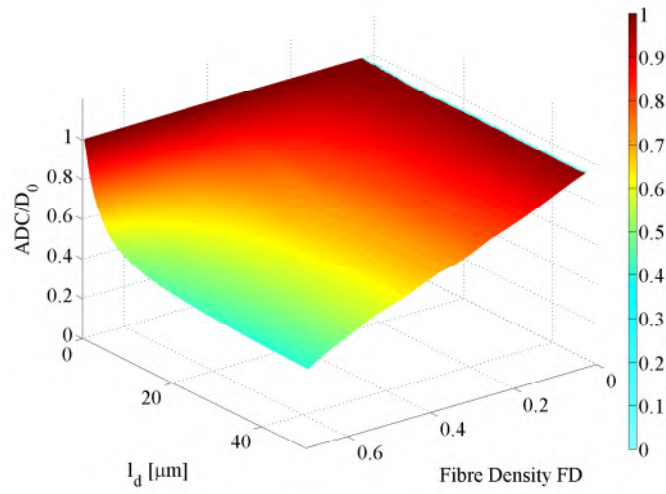
(b) x-direction, random fibre geometry

Figure 4.7: Simulation results of the apparent diffusion coefficient (ADC). ADC_X/D_0, i.e. the simulated relative diffusivity in the transverse plane as a function of l_d and FD for square (a) and random (b) packing geometry.
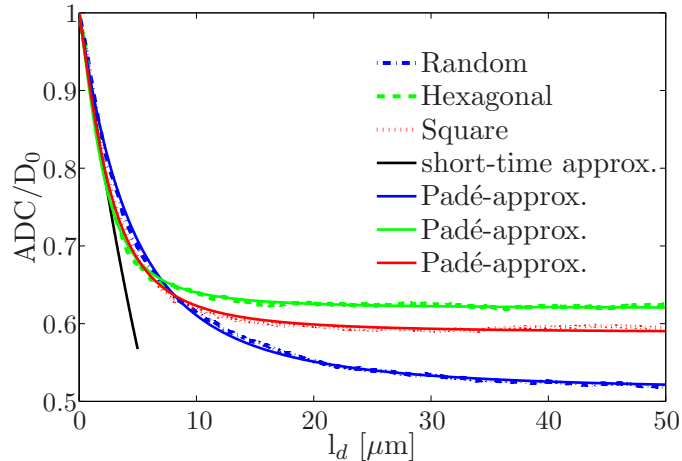
Figure 4.8: ADC_X as a function of the mean diffusion length l_d in the transverse plane for the three tested fibre geometries with a given fibre density of 0.58. The short-time diffusion regime, equation (4.1), is shown and the Padé-approximation for intermediate diffusion times, equation (4.14), is fitted through the simulation results.

regime with a time-dependent ADC, a long-time diffusion limit with a constant ADC, with a transition period in between. As an example, figure 4.8 shows the time-decay of the ADC as a function of l_d for the three tested packing geometries each with a packing density of 0.58.

In the next items, we present the comparison between the simulated ADC and the models for the time-dependent diffusion coefficient as described in section 4.2.

1. Short-time diffusion regime
As shown in figure 4.8, the decay of the ADC in the short-time regime is the same in the three cases and corresponds to equations (4.1) and (3.3) with $r_{\text{fibre}} = 10$ μm and FD = 0.58. However, the ADC-decay curves deviate in the long-time diffusion limit for each geometry and fibre density.

2. Transition between short-time regime and long-time limit:

– To test for anomalous diffusion (see equation (2.17)), the data can be replotted as $\log(r_{rms}^2)$ versus $\log(\Delta)$. Normal diffusion yields a slope of 1; anomalous diffusion yields a slope of $2/d_w \leq 1$ with d_w the walk dimension. One can

derive the following equation from equation (2.17):

$$\frac{r_{rms}^2}{\Delta} \propto \Delta^{2/d_w - 1}.$$

A clear picture of the dependence of the diffusion behaviour with respect to the diffusion time is obtained when plotting log r_{rms}^2/Δ as a function of log t. Then normal diffusion yields a line slope of 0, and anomalous diffusion yields a line slope of $2/d_w$-1 [18].

Logarithmic plots of r_{rms}^2/Δ versus Δ are shown in figure 4.9 for the three different packing geometries. $<r^2>/\Delta$ is in fact proportional to the ADC. The plots show that at intermediate diffusion times, the diffusion is anomalous, whereas for very short and long diffusion times, the diffusion is normal. It is clearly visible that the transition time from anomalous to normal diffusion occurs at a longer diffusion time for the random than for the ordered packing geometries.

– The Padé interpolation formula, equation (4.14), was fitted to the simulation results using a Levenberg-Marquardt algorithm to obtain the ADC in the long-time diffusion limit (figure 4.10(a)), $\frac{1}{\Lambda}$ and the Padé length $\sqrt{D_0\theta}$ (figure 4.10(b)). The goodness of the fit was evaluated visually and by calculating the correlation coefficient R^2. A good correspondence with the Padé interpolation (equation (4.14)) was obtained for the random geometries ($R^2 \geq$ 0.995), for the hexagonal packing geometries with $0.2 \leq FD \leq 0.88$ ($R^2 \geq 0.992$) and for the square packing geometries with $0.2 \leq FD \leq 0.7$ ($R^2 \geq 0.993$). For very low fibre densities (≤ 0.2), R^2 is lower due to variations caused by statistical noise. For higher fibre densities the ADC started to deviate systematically from equation (4.14) with increasing fibre density and tortuosity Λ. The worst fit, i.e. an overestimation of the Padé length, was found for the highest packing geometries ($R^2 = 0.985$ for FD $= 0.78$ for the square geometry and $R^2 = 0.98$ for FD $= 0.91$ for the hexagonal geometry).

The fitted Padé lengths (figure 4.10(b)) are about 5 μm larger for a random packing than for ordered packing geometries, which indicates a longer transition between short- and long-time diffusion limit.
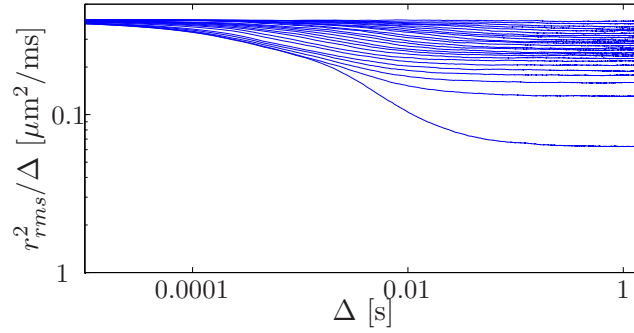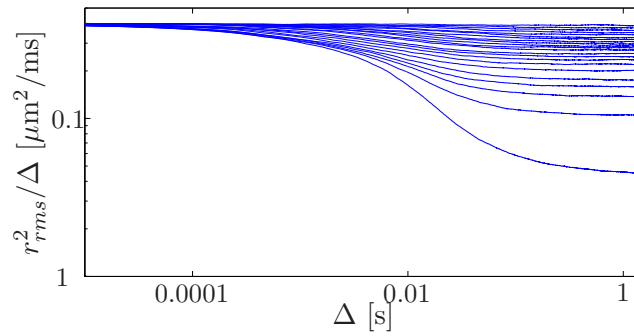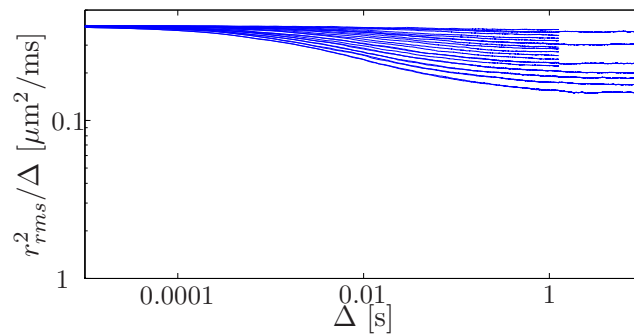
Figure 4.9: Logarithmic plots of r^2_{rms}/Δ as a function of Δ for various fibre densities (0.1 up to the closes packing) and packing geometries (a) hexagonal, (b) square, (c) random. For the plot of the random geometry, extra simulations are performed with 25.000 particles for longer diffusion times.
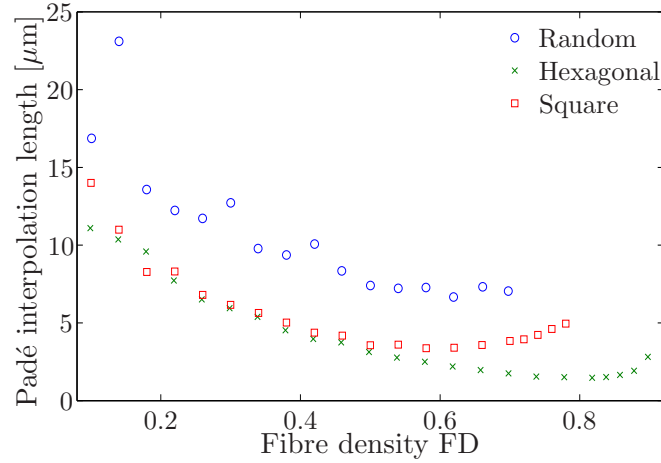
(a)
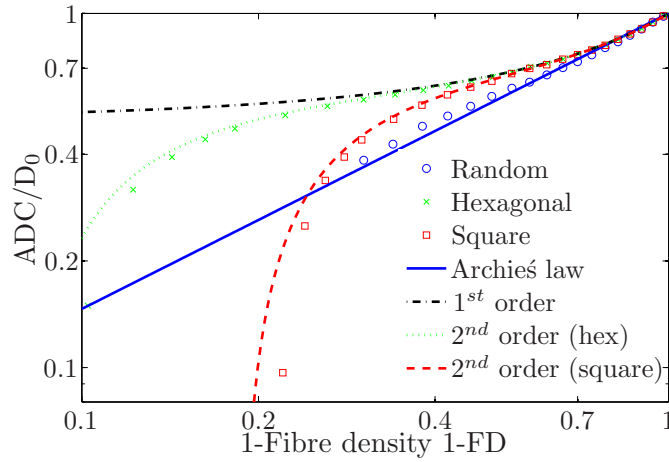
(b)

Figure 4.10: Fitted parameters of the Padé-approximation (4.14) for different FD. (a) The Padé length, $\sqrt{D_0\theta}$. (a) the ADC in the transverse plane (an average is taken of ADC_X and ADC_Y)in the long-time limit plotted as a function of (1-FD) in a double logarithmic scale and compared to the Archieś law (equation (4.8)) and the Maxwell-Garnett equations of the 1st and 2nd order for a hexagonal and square packing geometry (4.10,4.11).

3. Long-time diffusion limit

The ADC becomes $\frac{1}{\Lambda}$ in the long-time limit. Values for the ADC in the long-time diffusion limit were obtained when fitting the Padé interpolation formula, equation (4.13), to the simulation data and shown in figure 4.10(b).

– The fitting for the regular packing geometries (figure 4.10(a)) confirm the derived Maxwell-Garnett formulas of the 1st and 2nd order for a hexagonal and square packing geometry (equations (4.10) and (4.11)).

– Archie's law, equation (4.8), was fitted to the simulation results using a Levenberg-Marquard algorithm to obtain β for the different geometries. For the random packing geometries, it was possible to fit equation (4.8) for all porosities (0.3-0.7) resulting in $\beta_{random} = 0.790 \pm 0.014$ with $R^2 = 0.9935$. In contrast, for ordered geometries no reasonable fit was obtained against equation (4.8) for the simulation data with low porosities. The best fits were obtained for the range of porosities 0.3-0.98 for the square geometry and 0.14-0.98 for the hexagonal geometry resulting in $\beta_{square} = 0.636 \pm 0.020$ with $R^2 = 0.9827$ and $\beta_{hexagonal} = 0.4685 \pm 0.025$ with $R^2 = 0.9187$.

- **Effect of fibre clustering**

  The ADC for clustered geometries and random geometries with equal fibre densities is shown in figure 4.11. The simulations reveal that the transition between short and long diffusion time takes longer for clustered packing geometries than for homogeneous packing geometries. Moreover, ADC_X in the long-time diffusion limit is slightly lower for clustered geometries than for homogeneous geometries. The difference in ADC_X between both cases increases with overall fibre density.

- **Effect of the surface relaxation**

  The effect of surface relaxation on the simulated diffusion coefficient is shown in figure 4.12 where ADC_X is shown in the case of absence of surface relaxation and in the case of a surface relaxivity ρ of $3\,\mu$m/s. The ADC decreases slightly in the presence of surface relaxation. For a fibre density of 0.7, the decrease in ADC is $3\,\%$.
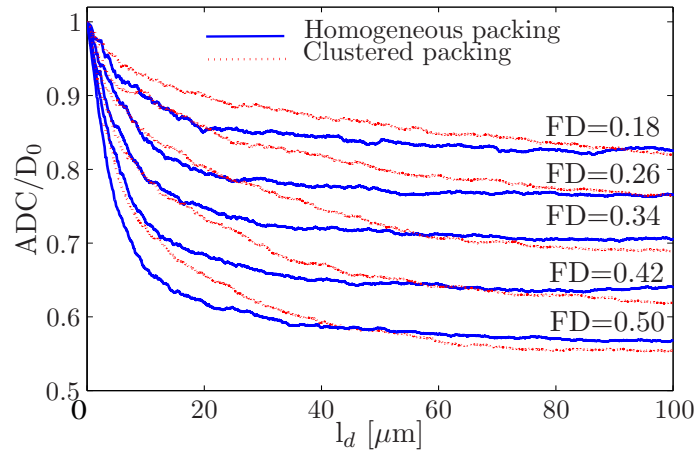
Figure 4.11: Effect of clustering on the simulated apparent diffusion coefficient in the x-direction for varying FD in a randomly packed fibre geometry. The dotted red lines represent ADC_X for the clustered geometry while the solid blue lines represent ADC_X in the homogeneous random geometries.
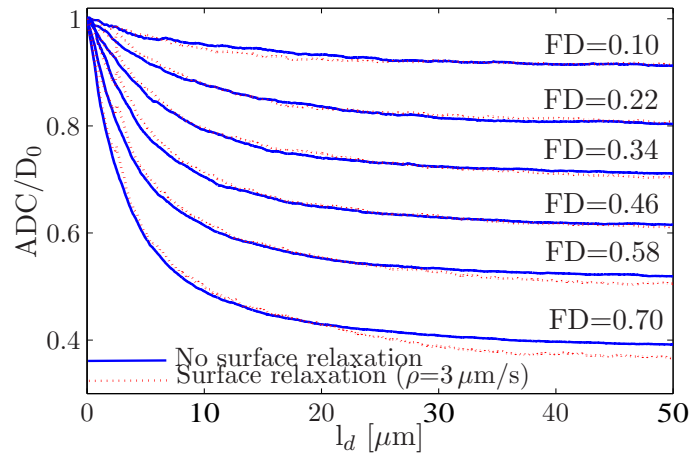

Figure 4.12: Effect of the surface relaxation on the simulated apparent diffusion coefficient in the x-direction for varying FD in a randomly packed fibre geometry. The solid blue lines correspond with the ADC_X without surface relaxation while the dotted red lines represent the ADC_X with surface relaxation for a given relaxivity $\rho = 3\,\mu m/s$.

fibre packing geometry	accuracy	precision
Hexagonal	0.1%	0.8%
Square	0.03%	1.0%
Random	-0.1%	1.0%

Table 4.3: The accuracy and precision of the simulation of ADK_Z calculated according to equation (4.24) and (4.25)

4.3.2.2   Simulation results of the apparent diffusion kurtosis (ADK)

- **Precision and accuracy**

  Figure 4.13(a) shows the ADK obtained from MC-simulations in the z-direction. In this direction the ADK was found to equal zero for the three different packing geometries. The calculated values for the accuracy and precision of the simulation of the ADK are presented in table 4.3. There is some variation in the accuracy between the different fibre pakcing geometries. However, for each fibre geometry, the accuracy value is smaller than the precision value and thus acceptable.

- **Effect fibre geometry and density**

  The ADK in the x-direction (perpendicular to the cylinder direction) is shown for a hexagonal packing (figure 4.13(b)), a square packing (figure 4.14(a)) and random packing (figure 4.14(b)) as a function of l_d and FD. Within the confidence levels as determined in the accuracy and precision study, the ADK was found to be identical in both the x- and the y-direction.

  Whereas the diffusion kurtosis reaches zero in the longitudinal direction and for long diffusion lengths in the transverse plane, the kurtosis becomes positive (leptokurtic) in the transverse plane at intermediate diffusion lengths, indicating a diffusion profile more sharply peaked and containing more extreme values than a Gaussian diffusion profile. For low fibre densities, the ADK increases slightly with increasing fibre density and is similar for the three packing geometries, while the ADK increases considerably for higher fibre densities, whereby the highest kurtosis values are found for the square packing geometries. It is also seen that the ADK stays positive for longer diffusion lengths for the random than for the ordered packing geometries.
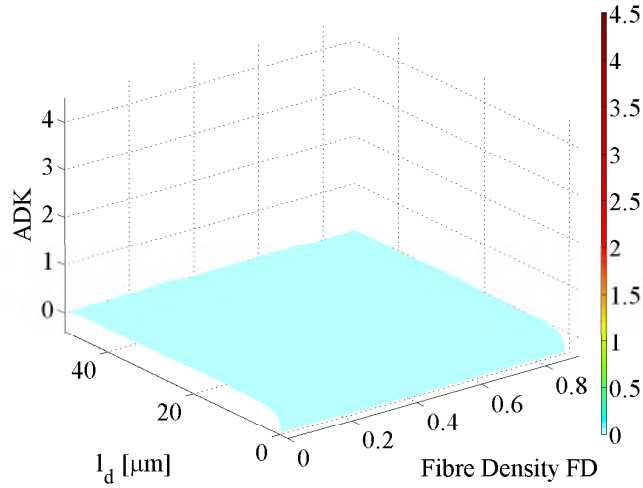
(a) z-direction, hexagonal fibre geometry
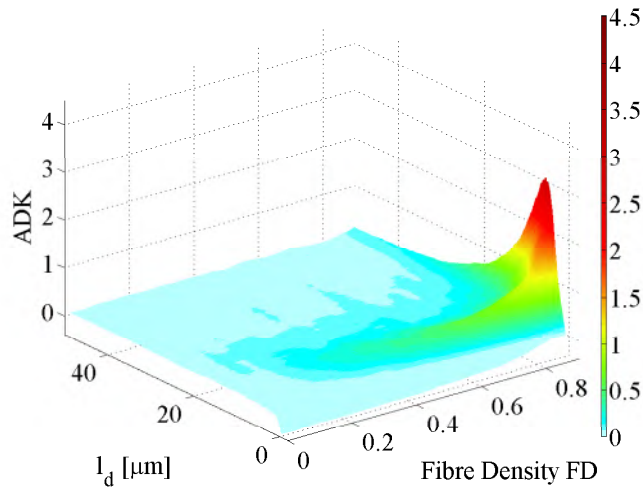
(b) x-direction, hexagonal fibre geometry

Figure 4.13: Simulation results of the apparent diffusion kurtosis ADK). (a) ADK_Z, i. e. the kurtosis in the longitudinal direction, is similar for the three packing geometries and is shown for a hexagonal fibre geometry as a function of l_d and FD. (b) ADK_X/D_0, i.e. the simulated relative diffusivity in the transverse plane, for a hexagonal fibre geometry as a function of l_d and FD.
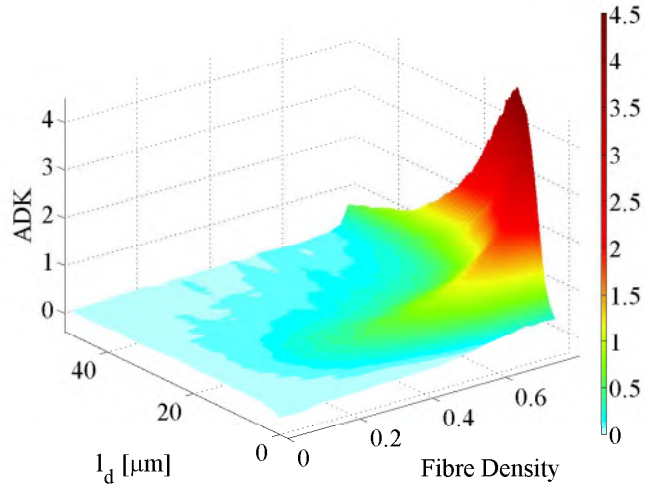
(a) x-direction, square fibre geometry
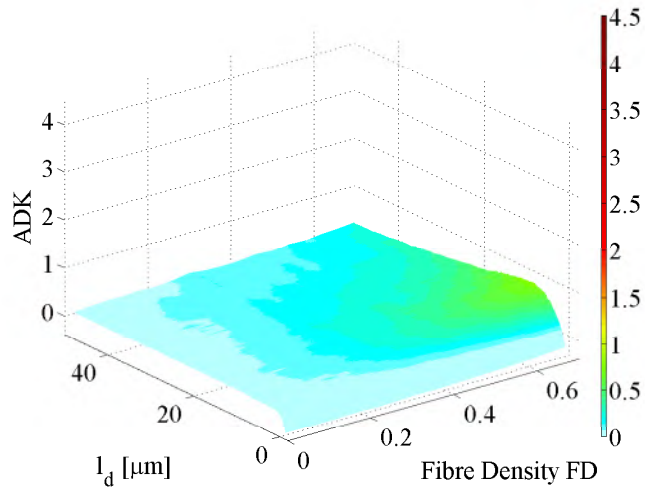
(b) x-direction, random fibre geometry

Figure 4.14: Simulation results of the apparent diffusion kurtosis ADK). ADK_X/D_0, i.e. the simulated relative diffusivity in the transverse plane as a function of l_d and FD for square (a) and random (b) packing geometry.
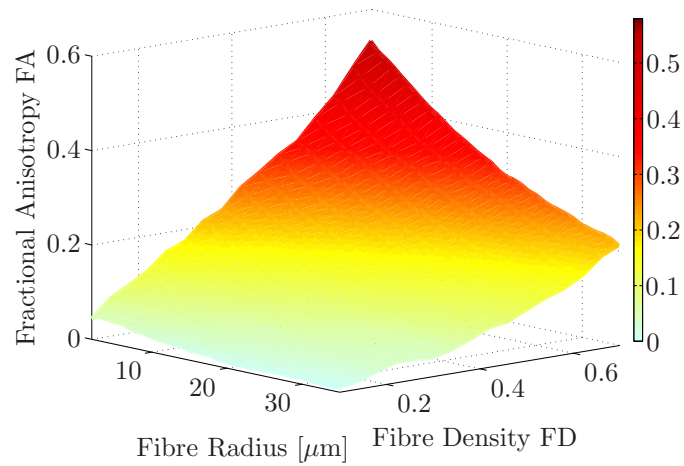
(a)
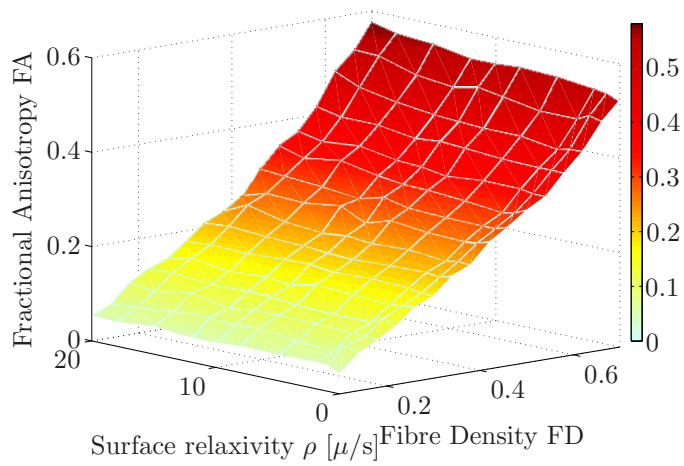
(b)

Figure 4.15: (a) Simulated FA-values for fibres without surface relaxation as a function of the fibre diameter and fibre density. (b) FA values for fibre with a radius of $2\,\mu m$ as a function of the fibre density and the surface relaxivity. The diffusion time Δ was $50\,ms$.

4.3.2.3 Simulation results of the fractional anisotropy (FA)

Based on the simulated ADCś in the x-,y-,z-directions, FA was derived using equation (4.19). FA-values were derived for randomly packed fibre geometries consisting various fibre densities and fibre diameters.

- **Effect of fibre radius and fibre density**

  Simulated values for FA as a function of the fibre radius and fibre density ($\Delta = 50$ ms) are shown in figure 4.15(a). FA increases significantly with increasing fibre density and decreasing radius.

- **Effect of surface relaxation**

  The effect of surface relaxation on FA is shown in figure 4.15(b) for a fibre radius of $2 \, \mu$m and a diffusion time Δ of 50 ms. For fibre bundles with a high fibre density and small radius, there is a slight increase in FA with increasing surface relaxation e.g. for a fibre density of 70 % the FA increases with 7% for an increase in relaxivity from 0 up to $20 \, \mu$m/s.

4.4 Experimental verification of the diffusion in an anisotropic fibre phantom

4.4.1 Materials and methods

Fibre phantoms

Since it was shown in chapter 3 that Dyneema$^{\circledR}$ is the preferred fibre material for constructing diffusion phantoms, the following experiments were carried out with this fibre material. The fibre bundles were manufactured as described in chapter 3.

To determine the micro-structure and the packing geometry, a fibre bundle with an external diameter of 3 mm was manufactured and scanned with an X-ray micro-CT at an isotropic resolution of $3.4\,\mu$m. A directional X-ray tube was used, with a focal spot size of approximately $3.5\,\mu$m, a tube voltage of $60\,$kV and an electron beam power of $9\,$W [150]. The data were acquired by a CMOS flat panel with a replaceable Gadox scintillator, containing 512 by 1024 pixels at a pixel size of $48\,\mu$m. To compensate for the relatively small difference in the attenuation coefficient between water and the fibres, iodine was added to the water ($0.97\,$mol/l) to increase its attenuation coefficient. This resulted in reconstructed cross-sections showing void areas, corresponding with the fibres.

To evaluate the effect of the packing density on the diffusion properties experimentally, 54 straight fibre bundles with varying FD were fabricated by contracting different number of fibres in a shrinking tube to an inside diameter of $9.5\,$mm. The fibre bundles were fixed to a PMMA plate and placed in a cylindrical container.

MRI measurements

Measurements were performed at 20°C on a Siemens Trio scanner ($3\,$T, Erlangen, Germany) equipped with an 8-element head coil. The fibre bundles were oriented parallel to $\vec{B}_0$ to eliminate magnetic field gradients that result from local susceptibility differences between water and fibres [97, 151].

- *DW-MRI* was performed in 60 directions with a DW EPI SE sequence with a receiver band width of 1275 Hz/pixel. A total of 20 slices was acquired in a repetition time (TR) of $8\,$s and with an effective echo time (TE) of $93\,$ms. To minimize the influence of eddy currents, a TRSE [40] diffusion preparation was used with b-factors of 0 and $700\,$s/mm^2. The actual

diffusion time Δ was estimated to be 36 ms based on the scanning protocol. The spatial resolution was 2 mm × 2 mm × 2 mm. The diffusion weighted images were used to estimate the DT's by linear regression and to derive the directional dependency of the diffusion coefficient [43]. Fibre tracking was performed using an Euler line integration algorithm [152].

- *Proton density* measurements were performed with a multiple spin echo sequence with 32 T_2-weighted contrasts with an inter-echo time spacing ΔTE = 40 ms, a TR of 10 s and BW = 130 Hz/pixel. The resolution was 0.9 mm × 0.9 mm × 2 mm. The proton density fraction was obtained as described in section 3.4.2. The *fibre density* was calculated as FD = (1-PD).

NMR bulk measurements

The time-dependent ADC and ADK were obtained in a fibre bundle with a measured proton density of 0.45 ± 0.05. Quantitative diffusion-measurements were performed on a 0.5 T bench-top NMR relaxometer equipped with a pulsed field gradient unit (Brüker Minispec mq20). Both a DW PFG stimulated echo (STE) and a spin echo (SE) sequence were used. Various diffusion weighted gradients (0 up to 2 T/m) were applied perpendicular to the fibre direction for increasing diffusion times (Δ = 20 ms up to 100 ms for the STE, Δ = 4 ms up to 50 ms for the SE, δ = 0.7 ms).

The acquired signal was averaged over 15 measurements to obtain a sufficiently high SNR. To minimize the influence of field inhomogeneities and gradient imperfections on the resulting b-factors, a calibration was performed on a water sample with dimensions similar to the fibre phantom.

The temperature was kept constant at 40°C ($D_0 = 3.28 \times 10^{-3}$ mm^2/s [30]). The difference in radius between 20°C and 40°C was not measurable. $ADC(\Delta)$ and $ADK(\Delta)$ were obtained by fitting the $ln\left(\frac{S(b)}{S(b=0)}\right)$-curve to the 2nd order cumulant expansion formula (see section 2.4.3.2):

$$ln\left(\frac{S(b)}{S(b=0)}\right) = -bADC + \frac{1}{6}b^2ADC^2ADK + O(b^3) \qquad (4.26)$$

using a Levenberg-Marquardt algorithm.

4.4.2   Results

Micro structure

Figure 4.16(a) and figure 4.16(b) show a cross-section and a 3D reconstruction of the micro-CT scans. It can be seen that the fibres are randomly packed and that the fibres are aligned parallel in the longitudinal direction. The quality and resolution of the micro-CT scans (about 5 μm) were too low to perform further processing.

FA measurements

Figure 4.17 shows the measured FA-values of the Dyneema$^{\circledR}$ fibre bundles as a function of the measured FD-values. The error bars of the experimental data correspond to the standard deviation over the chosen ROI's within the fibre bundles (containing 297 ± 45 voxels for the FD-measurements).

ROI's for the FA measurements were determined on the reconstructed fibre bundle using tractography and contained 96 ± 41 voxels.

The fits to obtain the FD were performed using a Levenberg-Marquardt algorithm with all correlation coefficients ≥ 0.997. The standard deviation of the FD was found to increase with FD.

The measured FA-values can be compared with the simulated FA-values for the same diffusion time as in the MR diffusion experiment ($\Delta = 36\,\text{ms}$). Simulations are shown for a random and a hexagonal fibre packing geometry. The best correspondence between the experimental and simulated FA is found for a random packing geometry. As an illustration of the time-dependency, the simulated FA-values in the long-time diffusion limit are also shown in figure 4.17. For $\Delta = 36\,\text{ms}$ the long-time diffusion limit is already reached in case of the hexagonal packing geometry but not for the random packing geometry.

The diffusion measurements performed for the different fibre materials (see chapter 3) were simulated to enable the comparison between experiment and simulation. FA was simulated for a diffusion time Δ of 50 ms and with fibre radii derived from the SEM-measurements (see table 3.1). In figure 4.18, FA-values as a function of the measured FD are compared to the simulated FA-values. The effect of surface relaxation was neglected during the simulations.
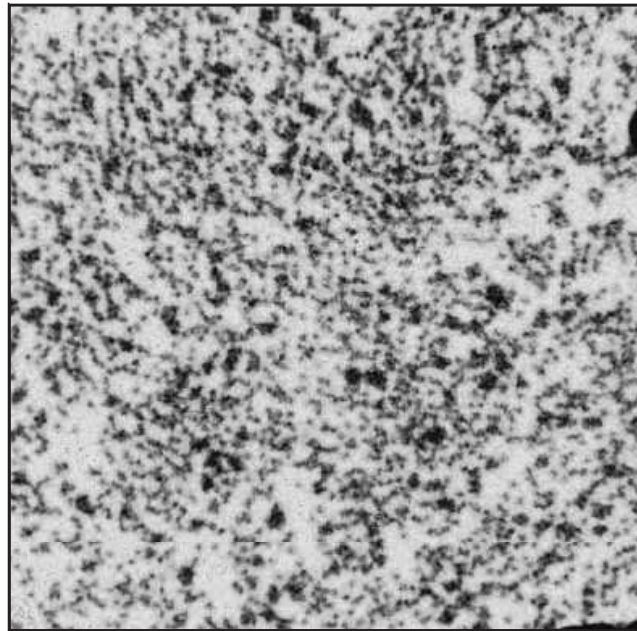
(a)
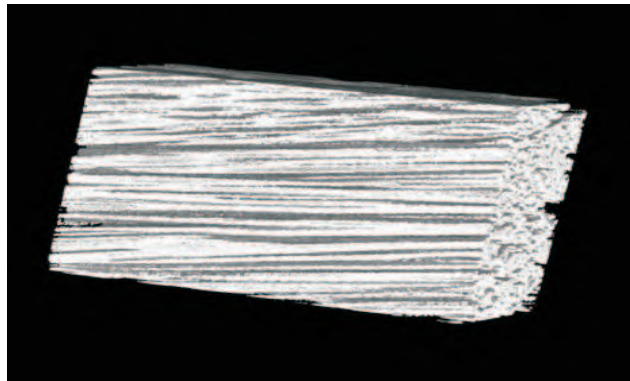
(b)

Figure 4.16: (a) micro-CT image of a cross-section of a fibre phantom. (b) three dimensional reconstruction of a small ROI chosen within the fibre phantom. The void area representing the fibres is rendered opaque (white) while the iodine-doped water is rendered transparent.
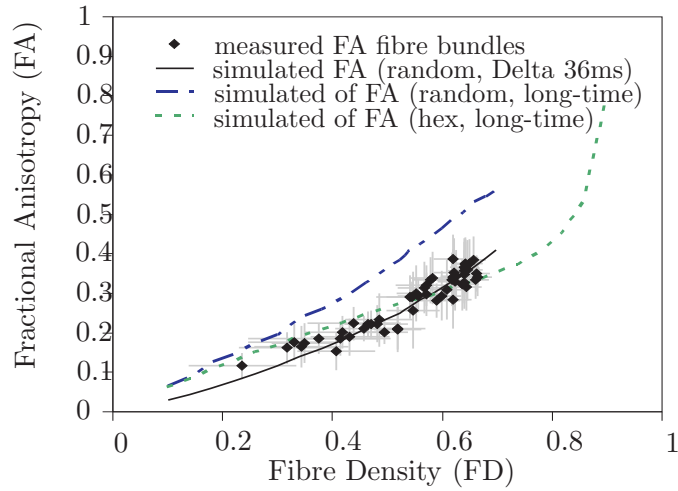
Figure 4.17: Comparison between the measured FA and the simulated FA of fibre bundles with a random and hexagonal fibre packing. The diffusion time Δ = 36 ms corresponds with a long-time diffusion limit for a hexagonal fibre packing geometry but not for a random fibre packing geometry which as also plotted for illustration.
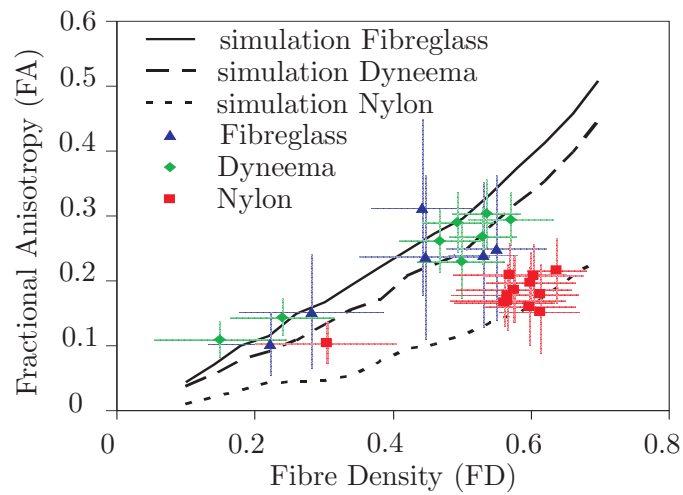
Figure 4.18: FA as a function of fibre density for the different fibre bundles as described in chapter 3. The measured FA-values of the fibre bundles are compared with the simulated FA-values for the different measured radii (see table 3.1) for Δ = 50 ms.

Time-dependent diffusion properties

Figure 4.19(a) shows the measured ADC(Δ) (obtained by a bulk NMR measurement) of a fibre phantom in comparison with the simulated ADC(Δ) for a random fibre packing with density of 0.54, 0.58 and 0.62. The same comparison between experiment and simulation is shown for the ADK(Δ) in figure 4.19(b). The ADC and ADK-values were fitted using a Levenberg-Marquardt algorithm with all correlation coefficients ≥ 0.998.

Taking into account the error bars, indicating the 95% confidence bounds of the fit, the fitted ADC-values were the same for the SE and STE sequence, whereas for the fitting results of the ADK, a difference of 10% was found. There is a good agreement between the experimental measured ADC(Δ) and the simulated ADC(Δ) with FD = 0.58, which matches the measured ADK(Δ) with a FD of 0.58 and the experimentally measured curve.

4.5   Discussion

4.5.1   MC simulations

Molecular diffusion of water in the interstitial space between fibres was modelled in the short- and long-time diffusion limit using MC simulations of random walk. The influence of the fibre density and the packing geometry on the diffusion properties (ADC, FA, ADK) has been investigated quantitatively.

At short diffusion times, the decay of the ADC as a function of the diffusion time is the same for both ordered and random geometries and depends only on the fibre radius and fibre density according to equation (4.1) as shown in figure 4.8. At long diffusion times, the ADC becomes constant and can be characterized by the tortuosity Λ, (equation (4.4)),which depends on the fibre density and the fibre packing geometry.

Models for the tortuosity in the long term diffusion limit

For low fibre densities, the simulated ADC agrees with the Maxwell-Garnett formula of the first order, equation (4.9), for all fibre packing geometries (see figure 4.10(b)). The simulated diffusion coefficients in the case of hexagonal and square packing geometries correspond very well with the higher-order analytical Maxwell-Garnett formulas for a hexagonal and a square packing (equations (4.10) and (4.11)) for
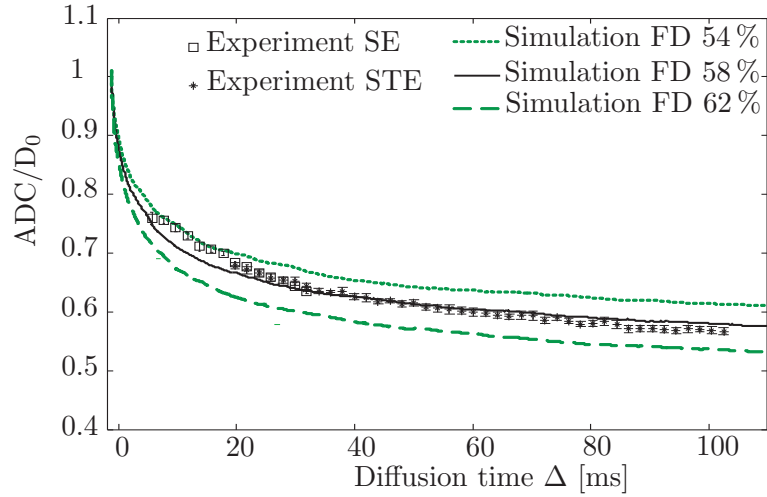
(a)
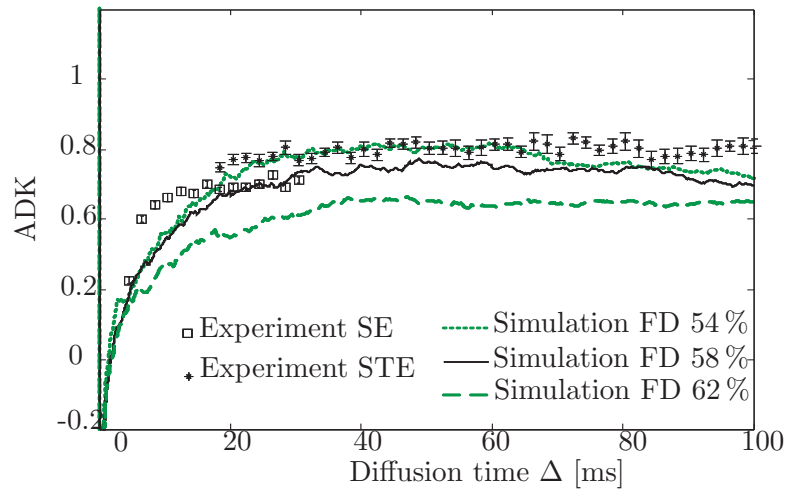
(b)

Figure 4.19:   Comparison between the measured and simulated time-dependent apparent diffusion coefficient ADC(Δ) (a) and kurtosis ADK(Δ) diffusion parameters of a fibre phantom with FD = 0.55 ± 0.05. A spin echo (SE) sequence is used for the diffusion measurements at short diffusion times (4 ms ≤ Δ ≤ 36 ms) and a stimulated echo (STE) sequence for long diffusion times (20 ms ≤ Δ ≤ 100 ms). Simulated values for the ADC and ADK are given for fibre densities FD = 0.54, 0.58 and 0.62.

all fibre densities, except for fibre densities close to the maximum obtainable packing density.

The tortuosity was also predicted by the empirical law of Archie, equation (4.8), and applied to the simulation results. Whereas the tortuosity fits well to equation (4.8) for high porosities or low fibre densities, the power-law relation does not apply for structures with a low porosity. The validity of Archie's law for low fibre densities is obvious and in fact a linear behaviour instead of a scaling law. One would expect the Archie's law to apply for high fibre densities, near the theoretical limit for FD approaching 1. However, no data points can be generated close to FD = 1. Based on the simulations performed in this study, the law of Archie appears to be less suitable than the first order Maxwell-Garnett formula, equation (4.9), to predict the tortuosity at low FD.

Pocket effect

In contrast to the results for ordered packing arrangements, the simulations in the random packing geometries revealed more diffusion restriction and thus higher tortuosity and anisotropy values, especially at lower fibre densities (see figure 4.10). This may be attributed to the fact that for random geometries there is a larger variation in the distance between fibres. In case of nearly touching fibres, pockets or lakes are created in which the diffusing particles get trapped, resulting in an effective diffusion coefficient of zero in the long-time diffusion limit. This is illustrated in figure 4.20.

This so called "pocket-effect" [145, 153] also appears from figure 4.11 where the diffusion in the clustered randomly packed fibre geometries is more restricted than in homogeneously random packed geometries. It also explains the differences in tortuosity between hexagonal and square packings for higher densities (see figure 4.10(b)), where the diffusion process is mainly dominated by the pore structure of the interstitial space [154, 155].

As proven by the simulation shown in figure 4.10(b), the large spread in inter-fibre distance in a random packing geometry also results in a longer transition time between the short- and long-time diffusion limit in comparison with ordered geometries. In the case of clustered random fibre packing geometries, the transition time between the short- and long-time diffusion limit is even much longer (see figure 4.11).

In clinical DW-MRI, the diffusion time Δ is typically 50 ms or
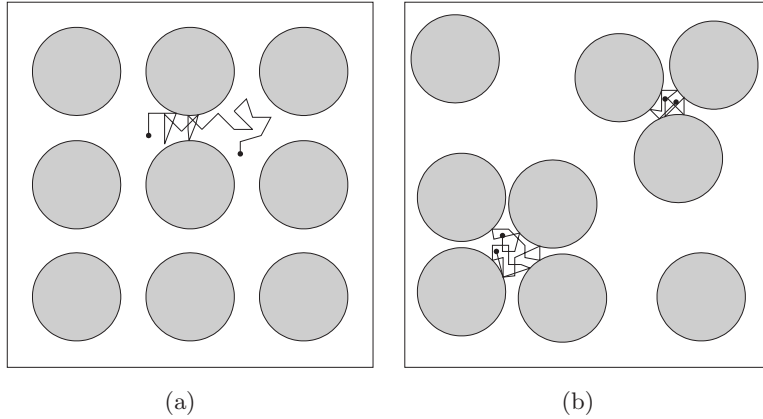
Figure 4.20: Illustration of the "pocket-effect": both geometries have the same density. (a) In the order geometry, the particles can travel relatively unhindered. (b) In the random geometry, lakes are created in which the particles are locally trapped

more. The time-dependency of the diffusion cannot be neglected when performing quantitative measurements and is related to the fibre size and the fibre density. This appears from figure 4.15(a). Decreasing fibre diameter will result in a higher measured FA. Increasing the diffusion time, will also result in a higher measured FA.

Transition between the short- and long-time diffusion limit.

The simulation results were used to test the accuracy of the Padé approximation for increasing fibre densities. The Padé form of the ADC(Δ) in equation (4.14) is a formula that enables interpolation between the analytical short- and long-time diffusion limits. The physical interpretation of the Padé length $\sqrt{D_0\theta}$ is not straightforward since there exist different length scales in the fibre packing geometries. Several experimental studies show that the Padé-equation (4.14) adequately fits ADC(Δ) for random bead packs [132, 133] and porous rocks [135]. The simulations confirm that this equation is also appropriate for fitting 2D geometries but some deviations are found for the ordered packing geometries at the highest fibre densities. Therefore the Padé approximation seemed less suitable in the case of 2D geometries with very high fibre packing densities.

Besides the Padé approximant, the time dependence of diffusion-weighted MR signals can also be parametrized with an anomalous

diffusion model as described in [17, 73]. Figure 4.9 shows that the diffusion is anomalous at intermediate diffusion times and normal at long diffusion times. The results shown here are in agreement with [18] where the anomalous diffusion due to obstacles in three dimensions is studied. Similarly to the fitted Padé lengths, which are larger for random packing geometries than for ordered packing geometries, the crossover time occurs much later for random than for ordered geometries, and is the longest for clustered random geometries. The diffusion in the interstitial space of random geometries at typical diffusion times used in DW-MRI can thus be considered as anomalous.

Surface relaxation

The simulations confirm the theory describing the effect of surface relaxation [137, 148] as explained in section 4.2. The effect of surface relaxation on the diffusion coefficient is shown in figure 4.12 by comparing the ADC in the case of absence of surface relaxation with the ADC in case of surface relaxation (with a surface relaxivity of $3\,\mu$m/s). The ADC remains equal at short diffusion times and decreases slightly in the long-time diffusion limit due to surface relaxation. This decrease increases with increasing fibre density, as expected from equation (4.12).

The effect of surface relaxation on the measured FA is shown in figure 4.15(b). Diffusion in fibres with a small fibre radius will reach the long-time diffusion limit sooner than in fibres with a larger radius. As a result, the measured FA is slightly increased due to surface relaxation. The increase in FA depends on the fibre density and surface relaxivity. As shown in chapter 3 hydrophobic fibre materials are the most appropriate fibre materials to use because their surface relaxivity is rather low and its effect on the measured ADC and FA negligible.

Kurtosis

MC simulations are frequently used to model diffusion in porous media. In addition, this study shows how MC simulations can be used for modelling the diffusion kurtosis, though it is found that the diffusion kurtosis is more susceptible to statistical variations. The diffusion kurtosis reaches zero for long diffusion lengths (see figure 4.14), confirming the hypothesis of a Gaussian diffusion profile that can be described by the tortuosity. However, for intermediate diffusion

lengths the diffusion kurtosis becomes positive. As the considered porous medium can be regarded as a single compartment system, the ADK reveals the non-Gaussian diffusion behaviour for intermediate diffusion lengths caused by the presence of barriers. As shown in figure 4.14, the diffusion kurtosis increases considerably with fibre density so that the DW-MRI signal shows a non-exponential decay for large b-values.

Several models in literature for brain white matter suppose the "slow exchange" limit to be valid and the diffusion in the extra-axonal part to be Gaussian [103, 143] (see section 5.2). The MC results here show a non-Gaussian diffusion profile in the interstitial space. The question raises whether the assumption made in some diffusion models [103,143] is correct that the signal attenuation at high b-values is caused exclusively by diffusion in the intra-axonal space. Although the Monte-Carlo simulations performed here suggest non-Gaussian diffusion in the interstitial space, the findings of this study cannot be extrapolated directly to the case of diffusion in the extra-axonal space. The geometry of brain white matter differs from the model of packed cylinders used in this study. The diameter of the cylinders used in the simulations was in average $20\,\mu m$ and the maximum fibre packing density for a random packing geometry in this study was 0.7. The diameter of the axons in brain white matter is much smaller than $20\,\mu m$ [27] and the axon density is measured to be about 0.8 [33] (see section 2.3.2). Both differences can diminish or shorten the effect of kurtosis in the diffusion measurements. In the next chapter, MC random walk simulations are performed in a more realistic geometry mimicking BWM.

4.5.2   Experiments

Figure 4.17 demonstrates a good agreement between the experimentally derived FA in the fibre bundles and the corresponding simulated FA for random fibre packing geometries. The hypothesis of a random packing geometry is verified by micro-CT imaging (figure 4.16). The random geometry is a consequence of the fabrication method of the fibre bundles. Although in reality the fibres are not perfectly parallel, the variation in the longitudinal directions is negligible in comparison with the close packing arrangement in the transverse plane. Thus, the model of parallel aligned cylinders is suitable for modelling the diffusion in the fibre phantom.

The transition from the short- into the long-time diffusion limit is

shorter for smaller fibre diameters. Consequently, the measured FA depends on the fibre diameter as shown in figure 4.18. There is again a good agreement between simulations and experiments.

Since the FA-measurements were performed on a clinical MR-scanner, the narrow pulse approximation [133] may not be valid anymore and is a potential source of inaccuracy in the comparison. In the calculations for the comparison, the diffusion time Δ is derived as the time between the onset of the first diffusion gradient and the onset of the third gradient in the TRSE sequence. However, Δ equals the effective diffusion time, i.e. the time at which the PDF is measured, only in the case that the duration of the diffusion gradients $\delta << \Delta$. For clinical sequences, this condition is not fulfilled. For the used TRSE sequence, the effective diffusion time could be estimated to be 36 ms instead of 30 ms [156]. The difference between the FA-values derived at a diffusion time of 36 ms and 30 ms is smaller than 1.6 % for all fibre densities. As the uncertainties on the measured FA-values are much higher than 1.6 % (see figure 4.17), it is justified to take the effect of the finite width of the diffusion gradients not into account when comparing the simulations with the experiments.

The time-dependent ADC and ADK were also measured and compared with the simulations. Figure 4.19 shows that the best agreement is obtained for a random fibre packing geometry with the corresponding measured fibre density.

By performing the measurement at 40°C, the term $(bD_0)^2$ was relatively high so that the signal decay is described by equation (4.26) from which the ADK can be determined. The small differences between the ADK measured with the SE and the STE sequence can be explained by the slightly different range of b-values used in both experiments. The precision of the signal decay measured with the NMR scanner or relaxometer is not high enough to resolve the higher order coefficients (kurtosis, ...). However, incorporation of higher order terms in the fitting of $\ln(S)$ was necessary to obtain an accurate description of the ADC.

The cumulant expansion form of the second order has been chosen to fit to the data since the parameters of this model (the ADC and ADK) could be simulated using random walkers. Since the phantoms are one-compartment systems, others models such as the bi-exponential form (see section 2.4.3.1) are not straightforward to interpret or simulate which makes validation hard. In the next chapter, we will investigate in more detail the validity of measuring higher order moments such as the kurtosis.

The homogeneity of the fibre density increased with increasing fibre density. For low FD, the Dyneema$^®$ fibres tend to cluster in the middle of the shrinking tube of the fibre phantom as observed in the micro-CT image (figure 4.16). The simulated ADC as a function of the diffusion length (figure 4.11) predicts a lowering of the FA because of a longer transition time from short into long diffusion time. In contrast, the experimental data show that for low fibre densities the measured FA was in average equal or higher than the FA obtained from the simulations in a homogeneous random geometry. This indicates that the considered clustered geometries used for the simulations do not correspond to the true geometries within the fibre phantoms. The assumption that the fibres are homogeneously random packed within the size of the voxels seems valid. Possible deviations in the co-registration between the proton density and FA-images due to the difference in resolution, may have caused a slight overestimation of FA for the low fibre densities.

4.6   Conclusion and original contributions

The diffusion in the interstitial space of anisotropic fibre bundles was measured using DW-MRI and bulk NMR diffusion measurements. The measured diffusion parameters agree with those obtained through MC random walk simulations in media consisting of parallel randomly packed cylinders. The MC simulations confirm the accuracy and validity of analytical models for ordered fibre packing geometries. The simulations in the random packed fibre geometries showed a higher FA and a longer transition diffusion time between the short- and long-time diffusion limit in comparison with ordered packing geometries.

We conclude that Dyneema$^®$ fibre phantoms are appropriate for testing DW-MRI sequences and diffusion parameters on clinical MRI-scanners. There are several potential applications for Dyneema$^®$ fibre phantoms. As the diffusion behaviour of the phantoms is well-known, they can serve as a daily reproducible reference measurement for DTI and can be used to investigate systematic errors of FA and other diffusion parameters. They are also helpful in multi-centre studies. The FA-values were high enough to perform fibre tracking and are therefore helpful in testing fibre tractography algorithms. The large variety of available shrinking tubes with different shapes and sizes enables the construction of fibre tract topologies. In chapter 6, some possible applications of the fibre phantoms are illustrated.

5

Validation of models for the diffusion weighted MRI signal in brain white matter

5.1 Introduction

As has been mentioned in chapter 2, the origin of the anisotropic DW MR-signal observed in brain white matter is still not completely understood. The contributions of the three components (intracellular diffusion, extracellular diffusion and exchange between the intracellular and extracellular space - see figure 2.18) are still unknown. To understand the diffusion in a complex geometry such as the brain white matter, a simpler model is considered including the main parts of the white matter structures.

In this chapter, the MC random walk simulations are discussed in the light of validation of diffusion models in BWM. MC random walk simulations were performed for BWM micro-structure. The bi-exponential model and the cumulant expansion form have been evaluated as a function of the considered b-interval and the exchange between the compartments. Other diffusion models described in the scientific literature will also be discussed.

5.2 Models for the diffusion in brain white matter

Models for the diffusion in BWM described in the literature are summarized, without the intention of being complete but rather to highlight the specific assumptions. Most of the models rely on the assumption of a Gaussian diffusion profile and a steady state regime of the diffusion process, corresponding to the long-time diffusion limit. Considering the exchange between the intracellular and extracellular space, a slow exchange limit with no exchange and the opposite case of a fast exchange limit can be distinguished, depending on the diffusion time Δ, the membrane permeability and the thickness of the myelin sheet [157].

The first parameter to describe diffusion anisotropy was the diffusion tensor DT, proposed by Basser et al [43]. The free diffusion physical model (with a Gaussian displacement profile) is assumed to be valid in the excited volume, but with D_0 replaced by the ADC in each direction.

The ADC concept has been widely adopted in the literature. Several numerical studies have been performed to model the ADC and corresponding DT in WM using MC random walk simulations. In these studies complex geometries with assumed micro structure and architecture similar to WM [158–160] are simulated. An analytical model describing the DW signal decay in bovine optic nerve was derived in [161] and can be applied to derive diffusion parameters such as the free diffusion coefficients, permeabilities and geometrical dimensions. Another framework was developed by Sen et al for predicting the long-time ADC of water parallel and perpendicular to a pack of myelinated axons in case of the slow exchange diffusion limit [143].

To explain the non-mono-exponential signal attenuation at high b-values, the assumption of a Gaussian diffusion profile had to be revisited. In the slow exchange limit, the two-compartment model assumes the presence of a fast and slow diffusion water pool with each a Gaussian diffusion profile. In this case the MR signal S as a function of b can be described by a bi-exponential function as explained in section 2.4.3.1. In vivo studies were performed by Niendorf et al [57] in the brain of a rat with b-factors up to 10000 s/mm^2. Fitting the bi-exponential model yielded an ADC_{fast} of 0.824 m^2/s and an ADC_{slow} of 0.168 m^2/s with corresponding fractions respectively 0.8 $\pm$ 0.02 and 0.17 $\pm$ 0.02. The assumption is often made that water

in the extracellular space corresponds to the fast diffusion pool and water in the intracellular space corresponds to the slow diffusion pool. However, the volume fractions obtained by fitting the bi-exponential model do not agree with those known for the intra- and extracellular compartments, i.e. 0.8 and 0.2 respectively [32].

The cumulant expansion form (see section 2.4.3.2) is proposed as a model free description for S fitting the MR signal for high b-factors. In this chapter, the usefulness of the cumulant expansion form is discussed.

The q-space approach, explained in section 2.4.3.3, provides also a model free description of the MR signal in BWM. A composite hindered and restricted model of diffusion (CHARMED) within axons is introduced by Assaf et al in [103]. This model provides a theoretical framework that uses the q-space approach to model the restricted diffusion in the intracellular space and the DT model to describe the hindered diffusion in the extracellular space. The CHARMED model is elaborated to extract the axon diameter and density in WM (AxCaliber) [162].

5.3   Random walk simulations of the DW MRI signal in WM

Software phantom construction

The diffusion process was modelled in a raster with a square cross-section of $1\,\mathrm{mm} \times 1\,\mathrm{mm}$ filled with infinitely long parallel aligned rigid cylinders. The diameters and density of the cylinder packing were chosen similar to those observed in brain white matter [33]. The radii of the cylinders were distributed according to a Gaussian distribution with a mean radius of $5\,\mu$m and a standard deviation of $1.75\,\mu$m. The density of the cylinder packing was $79.5\,\%$. Figure 5.1 shows a cross-section of the cylinder packing.

Random walk simulation

The diffusion process was modelled by MC random walk simulation as described in the previous chapter (section 4.3). The first and higher order moments of the total travelled distance in the direction perpendicular and parallel to the fibres were used to calculate the ADC and the ADK.
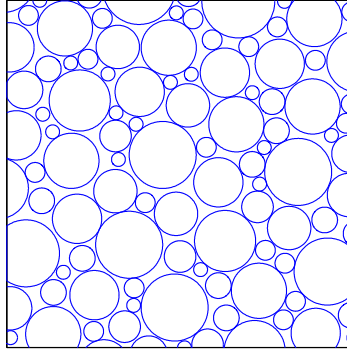
Figure 5.1: A cross-section of $80\,\mu m \times 80\,\mu m$ through the generated phantom consisting of parallel cylinders, showing the random packing geometry and the variation in diameter of the cylinders.

Diffusion MR experiment simulation

The diffusion weighted MR-signal $S(b)$ itself was also simulated as a function of the b-value by extending the MC simulations and taking the spin phase of the particles into account.

When applying a diffusion gradient $\vec{G}$ in a given direction $\vec{n}$ during a time δ, the phase ϕ of the diffusion spin phasors was incremented during each time step dt by:

$$\Delta\phi = \gamma\,\vec{G}\,.\,\vec{r}\,\,dt,$$

where γ is the gyromagnetic ratio, $\vec{r}$ is the position of the spin and

$$\vec{G} = \left\{ \begin{array}{rl} G\vec{n} & \text{if } 0 < t <= \delta \\ -G\vec{n} & \text{if } \Delta < t <= \Delta + \delta \\ 0 & \text{at other times.} \end{array} \right.$$

The diffusion weighted MR-signal S is then derived from the phases of all spins: $S = \sum e^{i\phi}$. For all calculations and fittings, the magnitude of this signal will be used, and will be further denoted as S.

The diffusion gradient is chosen perpendicular to the fibers. The gradient strength was varied with a constant gradient duration ($\delta = 0.7$ ms). Increasing diffusion times Δ (2 ms up to 100 ms) were considered so that the corresponding b-factors, defined by $\gamma^2\delta^2 G^2(\Delta - \delta/3)$, ranged from 0 up to 10.000 s/mm^2. The intrinsic diffusion coefficients for free media D_0 for the intra- and extracellular space of

brain white matter were taken as $10^{-9}\,\mathrm{m}^2/\mathrm{s}$ inside the cylinders and $2.5\,10^{-9}\,\mathrm{m}^2/\mathrm{s}$ outside the cylinders [103].

All particles were considered to reflect elastically at the cylinder boundaries. In a first case, the diffusion process has been simulated inside and outside of the cylinders simultaneously to obtain the ADC, the ADK and $S(b)$. In a second case, the diffusion process has been simulated separately inside the cylinders and outside the cylinders to obtain the corresponding apparent diffusion coefficients ADC_{in} and ADC_{ex}.

Simulations were performed for 300.000 spins with a timestep dt of 0.07 ms. The accuracy of the simulation of the DW-MRI signal S was determined by simulating the diffusion weighted MR signal in a free medium, showing a mono-exponential decay of S as a function of b according to $S = e^{-bD_0}$.

Evaluation of diffusion models

Validation of a bi-exponential diffusion model

The validity of the bi-exponential model was tested by fitting the simulated S(b)/S(b=0)-curve equation for each diffusion time Δ against the bi-exponential model using a Levenberg-Marquardt algorithm:

$$\frac{S(b)}{S(0)} = \alpha e^{-b\mathrm{ADC}_{\mathrm{slow}}} + (1 - \alpha)e^{-b\mathrm{ADC}_{\mathrm{fast}}}. \qquad (5.1)$$

The fitted values for α, $\mathrm{ADC}_{\mathrm{slow}}$ and $\mathrm{ADC}_{\mathrm{fast}}$ were compared to the theoretical value for α (0.795) and the simulated values for the diffusion coefficient inside the cylinders and outside the cylinders ADC_{in} and ADC_{ex}.

The effect of the considered b-interval was evaluated by increasing the interval from [0-500 s/mm^2] up to [0-10.000 s/mm^2] in steps of 500 s/mm^2. Original data sets contained 50 up to 1000 data points.

Validation of the cumulant expansion form

The model free cumulant expansion form b^N has also been evaluated:

$$ln(\frac{S(b)}{S(0)}) = C_1 b + C_2 b^2 + C_3 b^3 + \dots . \qquad (5.2)$$

This formula describes the cumulant expansion of ln S in powers of the applied gradients. The coefficients of the first and second
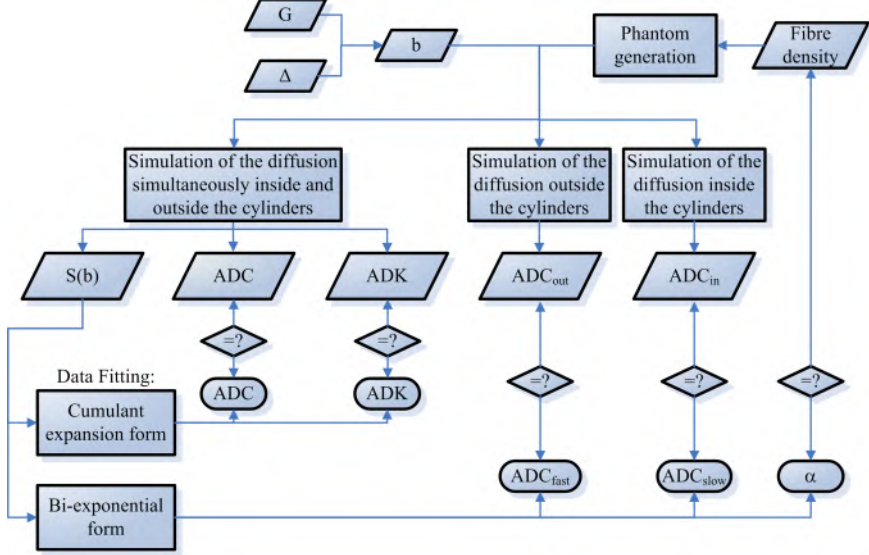
Figure 5.2: Flow chart of the evaluation of the diffusion models.

order yield the apparent diffusion coefficient ADC and the kurtosis ADK [62]:

$$C_1 = -ADC, \tag{5.3}$$

$$C_2 = \frac{1}{6}ADK \cdot ADC^2. \tag{5.4}$$

The termination of the series in equation (5.2) after the Nth order term is called the b^N cumulant expansion form. The applicability of the cumulant expansion form depends crucially on its convergence. This was investigated by fitting polynomials of the order $N = 1$ up to 10 to the logarithm of $S(b)$ for each diffusion time Δ using a Levenberg-Marquardt algorithm. For every fitted b^N cumulant form, the fitted first and second order coefficients were used to obtain the ADC and the ADK using equations (5.3) and (5.4). The fitted values for the ADC and ADK were then compared with the simulated values. The effect of the considered b-interval was evaluated as well by increasing the interval from [0-500 s/mm^2] up to [0-10.000 s/mm^2] in steps of 500 s/mm^2. A schematic overview of the procedure to evaluate the diffusion models is presented in figure 5.2.
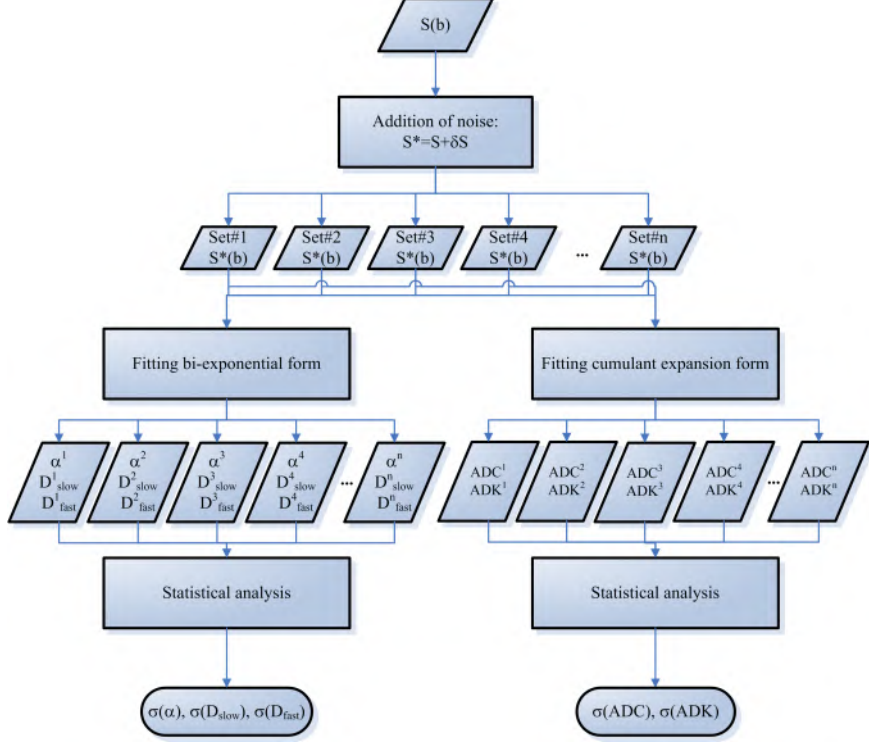
Figure 5.3: Flow chart of the evaluation of the noise characteristics.

Evaluation of the noise characteristics

The effect of noise on the precision of the fitting results has been investigated by simulations with the following data set $S(\text{b}=0, 600, 1200, 1800, 2400)$. Starting from this 5-point data set, we constructed 10.000 hypothetical data sets S^* by superimposing on each simulated complex point S a statistical error produced by a Gaussian noise generator: $S^* = S + \delta S$. A standard deviation of 1% of $S(0)$ was taken. Both the bi-exponential model and the cumulant expansion forms b^N with N=2,3,4 were fitted for each of the 10.000 data point sets. The standard deviation σ and mean value μ of the fitted parameters (α, ADC_{fast} and ADC_{slow} for the bi-exponential model and the ADC and the ADK for the cumulant expansion form) were derived numerically. A schematic overview of the procedure to evaluate the noise characteristics is presented in figure 5.3.

Exchange

The effect of exchange between the intra cellular and extra cellular space has also been assessed. Exchange was incorporated in the random walk simulations by the method described in [159]. Every time a water molecule hits a cylinder wall, the last step is recalculated and the particle is either transmitted or (specularly) reflected at the cylinder surface with a probability that is determined by the permeability P. The exchange probability for incident particles from the intracellular is $p_{I \rightarrow E}$ and for incident particles from the extracellular space is $p_{E \rightarrow I}$. The permeability P, $p_{I \rightarrow E}$ and $p_{E \rightarrow I}$ are related according to:

$$P = \frac{1}{4}\sqrt{\frac{6D_I}{dt}} p_{I \rightarrow E} = \frac{1}{4}\sqrt{\frac{6D_E}{dt}} p_{E \rightarrow I}. \tag{5.5}$$

The DW MR signal was simulated for 300.000 spins whereby P increased from 0 up to $100\,\mu$m/s in steps of $10\,\mu$m/s.

5.4   Results

Evaluation of the diffusion models

Validation of a bi-exponential model

For all diffusion times Δ, the datasets $S(b)$ are well fitted to a bi-exponential model, equation (5.1), with a correlation coefficient of minimum 0.9999. Figure 5.4(a) shows the fitted values for $(1\text{-}\alpha)$ as a function of Δ for increasing b-intervals. $(1\text{-}\alpha)$ is the fraction corresponding with the fastest ADC and should equal the water fraction outside the cylinders, i.e. 0.2. The best agreement between theoretical and fitted values of $(1\text{-}\alpha)$ is obtained for long diffusion times. When including a large b-interval in the fit, the water fraction inside the cylinders α is underestimated, especially at short diffusion times.

Figure 5.4(b) presents the fitted values for ADC_{fast} and ADC_{slow} as a function of Δ for increasing b-intervals. ADC_{slow} corresponds with the fitted fraction α and should thus be compared with ADC_{in} while ADC_{fast} should be compared with ADC_{ex}. The best agreement is obtained for long diffusion times. When including a large b-interval in the fit, ADC_{fast} and ADC_{slow} are underestimated, especially for short diffusion times.

(a) (1-α)
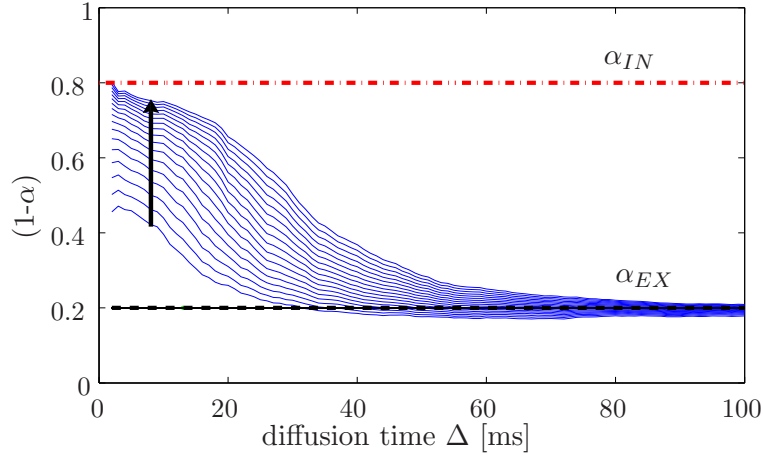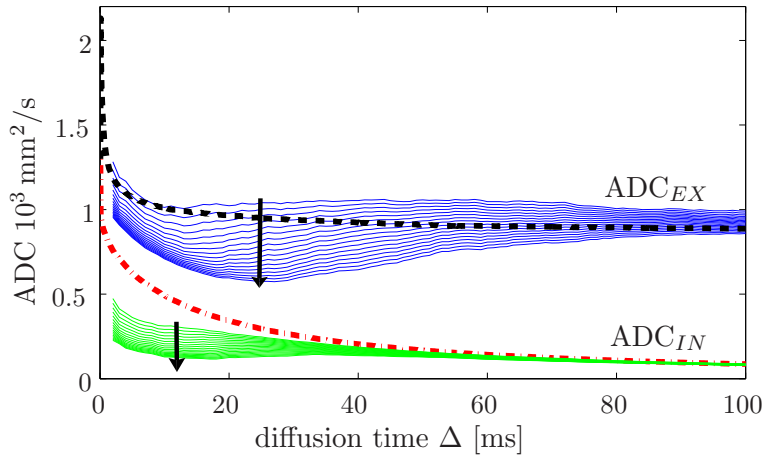
(b) ADC

Figure 5.4: Simulated values for (1-α) and the ADC's in a bi-exponential model. Fitted values are shown whereby the considered b-interval increases from [0-500 s/mm^2] up to [0-10000 s/mm^2], as indicated by the arrow in each figure. (a) 1-α, the fraction corresponding to ADC_{fast}, as a function of the diffusion time Δ. The theoretical fraction of the cylinder packing (α_{IN} - dotted red line) and the fraction outside the cylinders (α_{EX} - dotted black line) are also shown. (b) Fitted values for ADC_{fast} (blue lines) and ADC_{slow} (green lines) as a function of the diffusion time Δ. The simulated values for the ADC inside the cylinders (ADC_{IN} - dotted black line) and outside the cylinders (ADC_{EX} - dotted red line) are also plotted as a comparison.

Validation of the cumulant expansion form

For all diffusion times Δ, the datasets $S(b)$ were fitted to the cumulant expansion form b^N, equation (5.2), for increasing b-intervals. The fitted ADC and ADK values are compared to their simulated values for increasing N in figure 5.5 and figure 5.6 respectively. The cumulant expansion fits of $S(b)$ with the highest correlation coefficients resulted in fitted values for the ADC and ADK which were closest to the simulated values.

The minimum order N to obtain a good agreement between fitted and simulated values for the ADC and the ADK decreases with decreasing b-interval. When $N >= 7$, the fitted values for the ADC and ADK match the simulated values for all considered b-ranges. Cumulant expansion fits with $N = 3$ result in accurate fits for the ADC and the ADK for b-intervals ranging up to $2500\,\text{s/mm}^2$. Even for the shortest b-interval of $[0\text{-}500\,\text{s/mm}^2]$, the third order term should be included in the fit to obtain an accurate fit of the ADK. When taking the b-interval too large or N too low, the difference between fitted and simulated ADC is rather low but considerably larger for the ADK.

Evaluation of the noise characteristics

The effect of noise on the fitted parameters of both the bi-exponential model and the cumulant expansion form is demonstrated in figure 5.7(a) and 5.7(b). For the bi-exponential model, the largest errors are found on ADC_{fast} and α. For the cumulant expansion model, the relative variations in the fitted ADC and ADK-values increase with increasing order N. The bi-exponential model is found to be more sensitive to noise than the cumulant expansion model.
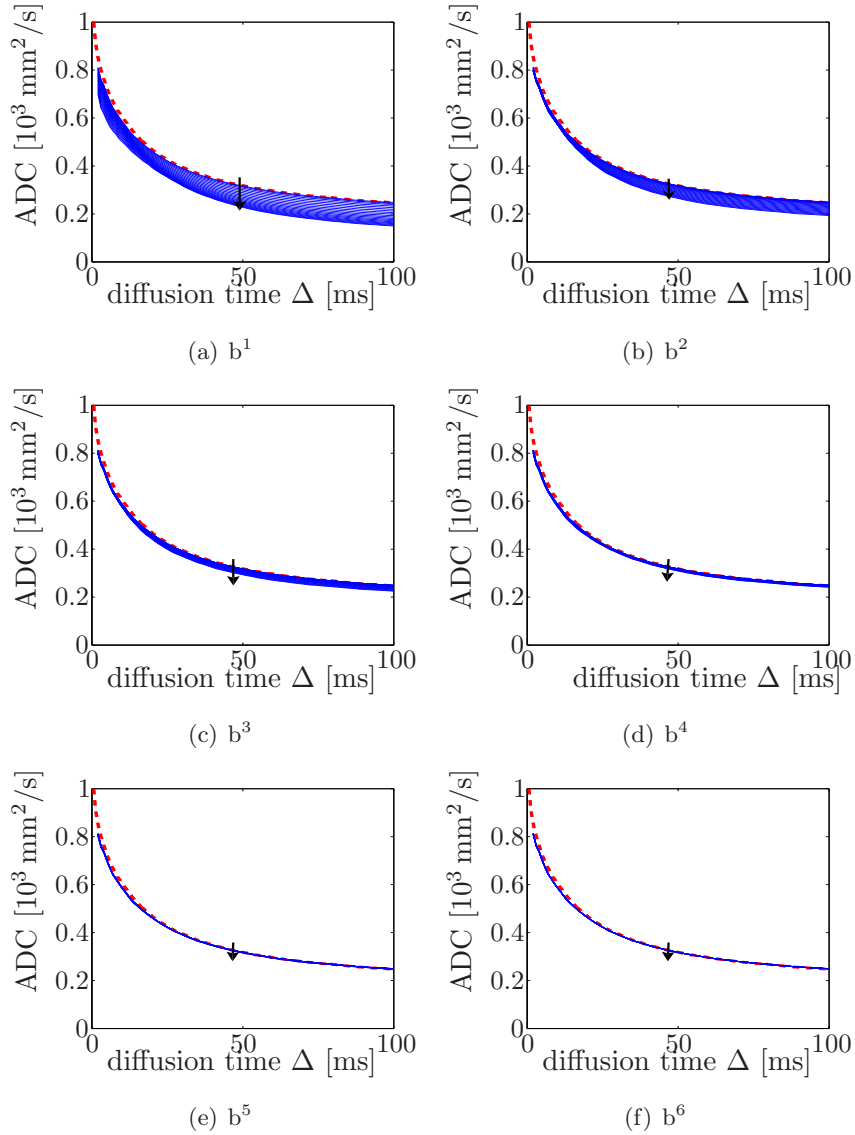
Figure 5.5: Fitting results of the ADC using the b^N cumulant expansion in comparison to the simulated values (dotted red line) for $N=1$ up to 6. Fits are shown whereby the considered b-interval increases from $[0\text{-}500\,s/mm^2]$ up to $[0\text{-}10000\,s/mm^2]$, as indicated by the arrow in each figure. The larger the considered b-interval, the more higher order terms need to be included in the b^N-fit to obtain a good correspondence between fitted and theoretical ADC-values. When $N \geq 6$, the fitted values for the ADC equal the simulated values for all considered b-ranges.
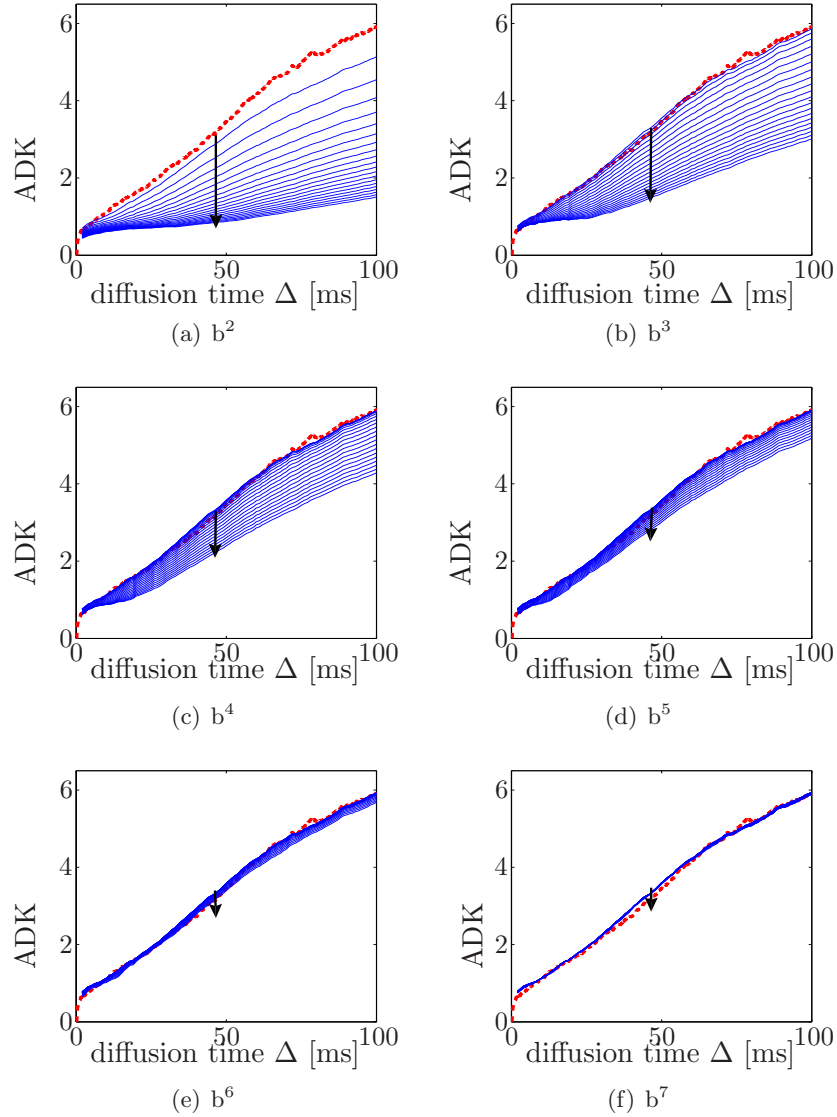
Figure 5.6: *Fitting results of the ADK using the b^N cumulant expansion in comparison to the simulated values (dotted red line) for $N=2$ up to 7. Fits are shown whereby the considered b-interval increases from $[0-500\,s/mm^2]$ up to $[0-10000\,s/mm^2]$, as indicated by the arrow in each figure. The larger the considered b-interval, the more higher order terms need to be included in the b^N-fit to obtain a good correspondence between fitted and theoretical ADK-values. When $N \geq 7$, the fitted values for the ADK equal the simulated values for all considered b-ranges.*

(a) bi-exponential model

(b) cumulant expansion form
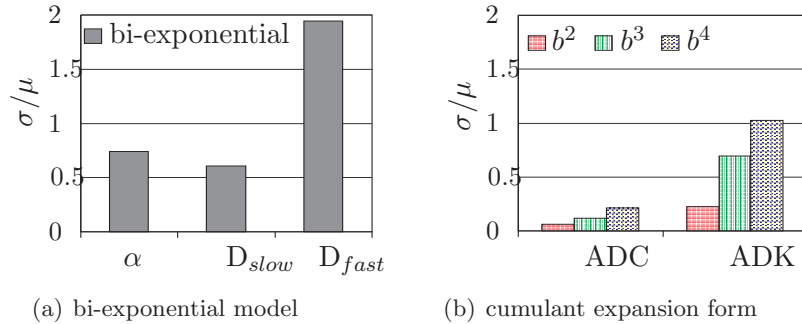
Figure 5.7: Relative noise levels when fitting the bi-exponential model (a) and the cumulant expansion form (b) to a 5-point data set superimposed with gaussian noise with a standard deviation of 1%.

Evaluation of the effect of exchange

Figure 5.8 shows the natural logarithm of the simulated DW MR signal $S(b)$ for increasing permeability and a diffusion time Δ of 50 ms. In the slow exchange limit, i.e. no exchange between the inside and outside of the cylinders during the considered diffusion time Δ, the $S(b)$-curve is clearly not exponential. When increasing the exchange between the inside and outside of the cylinder, the $S(b)$-attenuation curve becomes more similar to an exponential decay. It can be derived from figure 5.8 that in the fast exchange limit, the $S(b)$-curve becomes exponentially. The corresponding fitted ADC- and ADK-values are shown in figure 5.9 as a function of the permeability. The effect of exchange is larger on the fitted ADK parameter than on the ADC parameter.

The simulated $S(b)$-curves in the considered b-interval [0-2500 s/mm^2] for all diffusion times Δ were used to fit the described models for the DW MR signal (equations (5.1) and (5.2)). Figure 5.10 shows the fitting result of the bi-exponential model for increasing permeability. The fraction corresponding to ADC$_{fast}$ increases with increasing permeability (figure 5.10(a)). As can be seen in figure 5.10(b), ADC$_{fast}$ decreases and ADC$_{slow}$ increases slightly for increasing permeability P.

Figure 5.11 shows the results when fitting the b^3 cumulant expansion form to the simulated $S(b)$-curve for increasing permeabilitiy. The ADC increases with increasing permeability (see figure 5.11(a)) while the ADK decreases with increasing permeability (see figure 5.11(b)).
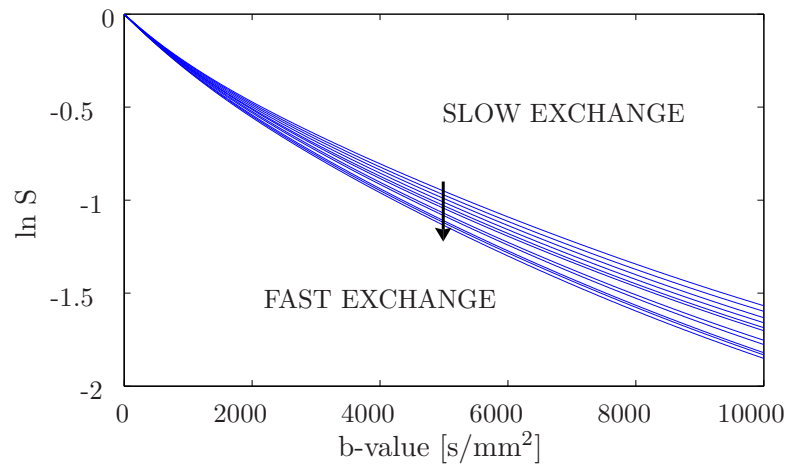
Figure 5.8: Simulation of the DW MR signal $S(b)$ for a diffusion time Δ of 50 ms. The arrow stands for increasing permeability P from 0 up to $100\,\mu m/s$.
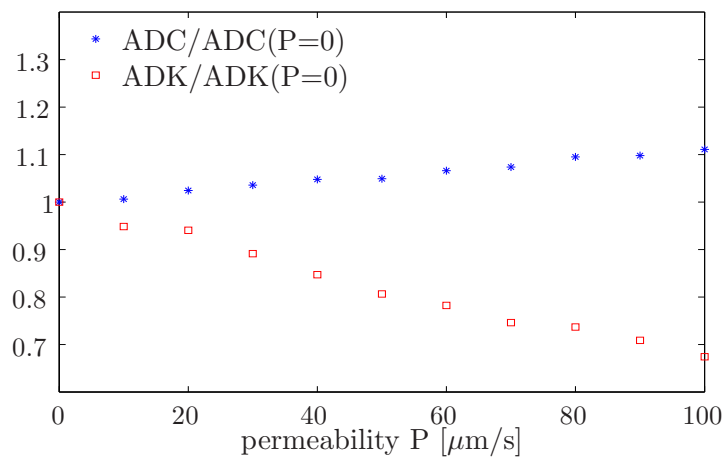
Figure 5.9: The relative ADC- and ADK-values as a function of the permeability P. ADC and ADK were fitted for a diffusion time Δ of 50 ms using the b^3 cumulant expansion form. The considered b-interval was [0-2500 s/mm^2]

(a) (1-α)
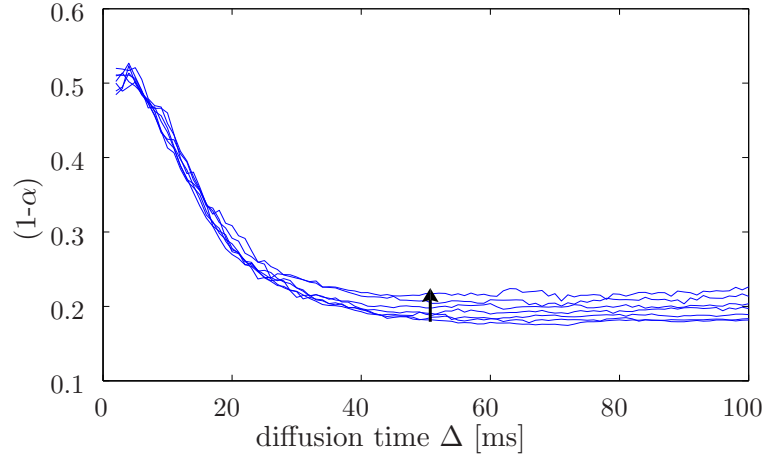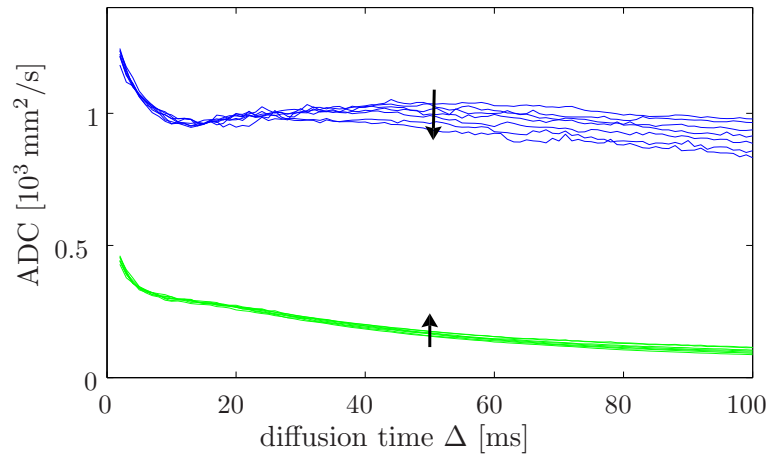
(b) ADC

Figure 5.10: Bi-exponential fitting results for $S(b)$ in the considered b-interval [0-2500 s/mm^2]. The arrows indicate the trend of increasing (1-α, ADC_{slow}) or decreasing (ADC_{fast}) for increasing permeability P from 0 up to 100 $\mu m/s$. (a) 1-α, the fraction corresponding to D_{fast}, as a function of the diffusion time Δ. (b) Fitted values for ADC_{fast} (blue lines) and ADC_{slow} (green lines) as a function of the diffusion time Δ.
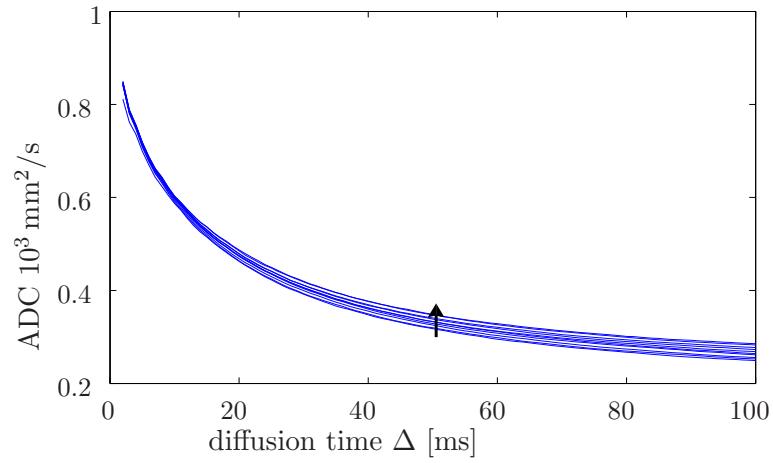
(a) ADC
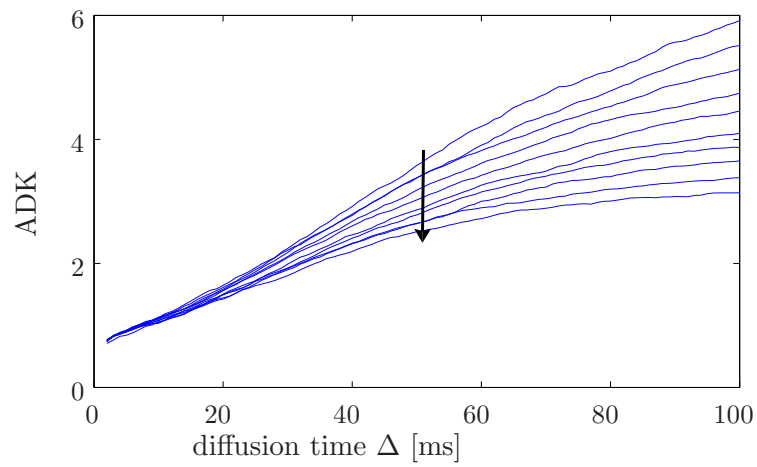
(b) ADK

Figure 5.11: Fitting results of the b^3 cumulant expansion in the considered b-interval $[0\text{-}2500\,s/mm^2]$ for increasing permeability P. (a) the ADC as a function of the diffusion time Δ. (b) the ADK as a function of the diffusion time Δ.

5.5   Discussion

Validation of the diffusion models

As can be derived from figure 5.4(a) and figure 5.4(b), the fitted values for ADC_{fast}, ADC_{slow} and α are dependent on the b-interval and the diffusion time Δ. The fitted values for $(1-\alpha)$ differ from the real water fraction outside the cylinders at short diffusion times. This indicates that the fitted fractions and corresponding diffusion coefficients are not solely attributed to the diffusion inside and outside the cylinders. Pseudo bi-exponential diffusion weighted signal attenuation can also be observed in single compartment systems such as the intra cellular space [103] and the interstitial space between fibres. The good quality of fitting a bi-exponential function to the data is not sufficient to prove the accuracy of this model. The results in this study suggest that the signal attenuation curve is not truly bi-exponential.

This study proves the convergence of the cumulant expansion form when fitting the diffusion weighted signal attenuation. The results of figure 5.5 and 5.6 show that the ADC and the ADK could be accurately fitted if the order N is large enough. The cumulant expansion form might be a better option to fit the diffusion weighted MR signal in b-intervals in the range of $[0 - 2500\,\text{s/mm}^2]$.

Noise effects

It is also shown that the cumulative expansion form is less noise sensitive than the bi-exponential model (figure 5.7). The noise simulations in figure 5.7 reveal that fitting the cumulant expansion form is more robust against noise than fitting the bi-exponential model. ADC_{fast} is more sensitive to noise than ADC_{slow} because ADC_{fast} corresponds to the smallest water fraction (0.2). Although the accuracy of the ADC and ADK improves with increasing order N (figures 5.5 and 5.6), the precision of the ADC and ADK decreases with increasing N (figure 5.7(b)).

For the parameter estimation, the magnitude data is fitted by a nonlinear least square method using a Levenberg-Marquardt algorithm. For SNR levels lower than three the noise distribution starts to deviate from a Gaussian distribution and becomes Rician [163]. In that case, a maximum likelihood estimation of the signal amplitude that takes into account the Rician noise behaviour, could result in more accurate fitting results [164].

Effect of the exchange

In case of exchange between the intracellular and extracellular space, the bi-exponential model, based on a two-compartment system in the slow exchange diffusion limit, is not straightforward interpretable any more. This is clearly demonstrated by the simulations in figure 5.10. When the permeability increases, the fitted compartment $(1-\alpha)$, corresponding with the fast ADC, increases and can no longer be associated with a physical compartment. The bi-exponential model fails in the case of intermediate and fast diffusion exchange across the cylinder walls.

On the other hand, using the cumulant expansion form turns out to be useful to explain the diffusion process in multi compartment system with or without mutual exchange. According to figures 5.11 and 5.9, increasing permeability results in an increase of the ADC and a decrease of the ADK. This can also be derived from figure 5.8: in the fast exchange limit, the diffusion is Gaussian with a mono-exponential signal attenuation and a kurtosis equal to zero. However when the exchange across the cell membrane slows down, the attenuation curve moves from the bottom left upwards to the right top and the kurtosis becomes positive. The relative change in the ADK is much higher than the relative change in the ADC when changing the permeability (see figure 5.9), which indicates that the kurtosis is a good probe for the presence of membranes and other barriers and is sensitive for changes in permeability.

Models for the DW MR signal that incorporate the kurtosis may reveal new insights in the physiology of cells during pathological states. As an example, because of the remarkable correlation with membrane depolarization and cell swelling induced by ischaemia [77], it has long been assumed that the decrease in ADC observed in WM during stroke is caused by an increase of intracellular water. As demonstrated in the simulations above, the decrease in ADC may also be caused by a sudden drop of the membrane permeability resulting in an increase of the kurtosis. The kurtosis has been compared in [165] between normal rat brain (0.53 ± 0.05) and ischaemic rat brain (1.42 ± 0.1), confirming this hypothesis. Another potential clinical application is the detection of cancer and metastases [33]. The water ADC is significantly decreased in malignant tissues. The origin of the change in the observed ADC is not completely understood. Fitting the kurtosis as a measure for the permeability could provide useful additional information.

5.6 Conclusion and original contribution

In this chapter, MC random walk simulations were performed in a geometry with intra- and extracellular compartments imitating BWM. The bi-exponential model and the cumulant expansion form were evaluated as models for the DW MRI signal in BWM. The good accuracy of the bi-exponential fit does not prove the validity of the model since there is a strong dependence on the considered b-interval and diffusion time. The cumulant expansion form is proposed as an alternative. The diffusion coefficient and kurtosis could be accurately fitted when higher-order terms are included in the cumulant expansion form. Preliminary results show that the cumulant expansion form is less sensitive to noise than the bi-exponential models. More research is required to determine the optimal order N and b-interval as a trade-off between accuracy and precision of the fitted parameters.

The kurtosis appeared to be a useful parameter to detect changes in membrane permeability. Fitting the kurtosis could be useful to link the observed changes in ADC in pathologies such as acute stroke and malignant tumours to the underlying cell physiology.

6

Applications of anisotropic diffusion fibre phantoms

6.1 Introduction

This chapter points out some potential applications where anisotropic fibre phantoms may be useful as DW MRI test objects. Because of their well-known structure and anisotropy, they are suitable for sequence design, optimisation and the evaluation of imaging artefacts which is exemplified in section 6.2. Since the fibre bundles are also flexible, they can be used to create structures that imitate the *in vivo* white matter tracts. This is illustrated in section 6.3. In section 6.4, a crossing fibre phantom is proposed which can be used to test fibre tractography algorithms.

6.2 Testing DWI sequences

While developing and testing new diffusion sequences, fibre phantoms may be used as a relatively easy-to-make and stable anisotropic test object with a well-known structure. As an example, the effect of susceptibility artefacts in standard EPI and spiral acquisition techniques is illustrated here using diffusion fibre phantoms.

Materials and methods

Two fibre bundles were fabricated and fixed in a closed container filled with Gd-doped physiological saline. To evaluate the influence of susceptibility artefacts a spherical air cavity was positioned between the two bundles.

Imaging was performed on a 1.5T Siemens Symphony scanner using an 8 elements head coil. Diffusion-weighted images were acquired in 6 directions with b- factors of 0 and 1000 s/mm^2. To minimize the influence of eddy currents, a TRSE diffusion preparation was used [40]. The $\vec{k}$-space was sampled with an 8-interleaved Archimedean spiral trajectory with a maximum gradient amplitude of 19.5 mT/m and a maximum slew rate of 94 mT/m/s [13]. For comparison, also single shot standard EPI scans were acquired with a bandwidth of 1346 Hz/Px and 20 averages. For both sequences, the image resolution was 2.5 x 2.5 x 2.5 mm (64 x 64 matrix, 160 x 160 mm FOV, 2.5 mm slice thickness). A total of 20 slices were acquired with a TR of 2000 ms and TE = 80 ms.

Results

In figure 6.1, the diffusion unweighted (b = 0) images recorded with a Cartesian and spiral EPI sequence are shown. A standard T_2 TSE image (figure 6.1(a)) is also shown as a reference. The spatial distortions are less pronounced in the spiral image (figure 6.1(b) than in the Cartesian sampled EPI-images (figures 6.1(c) and 6.1(d)). Figure 6.1(c) and 6.1(d) illustrate the dependence of the susceptibility artefacts on the phase encoding (PE) direction.

Discussion

Fast sequences are sensitive to susceptibility artefacts. The $\vec{k}$-space trajectory of spiral and Cartesian EPI is described in section 2.2.3. The different trajectories result also in different point spread functions. The radial symmetric point spread function of a spiral acquisition results mainly in blurring artefacts and less geometric distortions compared to Cartesian EPI acquisition. Depending on the phase encoding direction, the tracked fibre bundles are biased near transitions between regions with different magnetic susceptibility such as air and water. The phantoms allow quantitative analysis of the effect of susceptibility differences on e.g. diffusion parameters such as FA and ADC and on the accuracy of the extracted fibre tracts.

(a) T$_2$ TSE

(b) spiral

(c) EPI
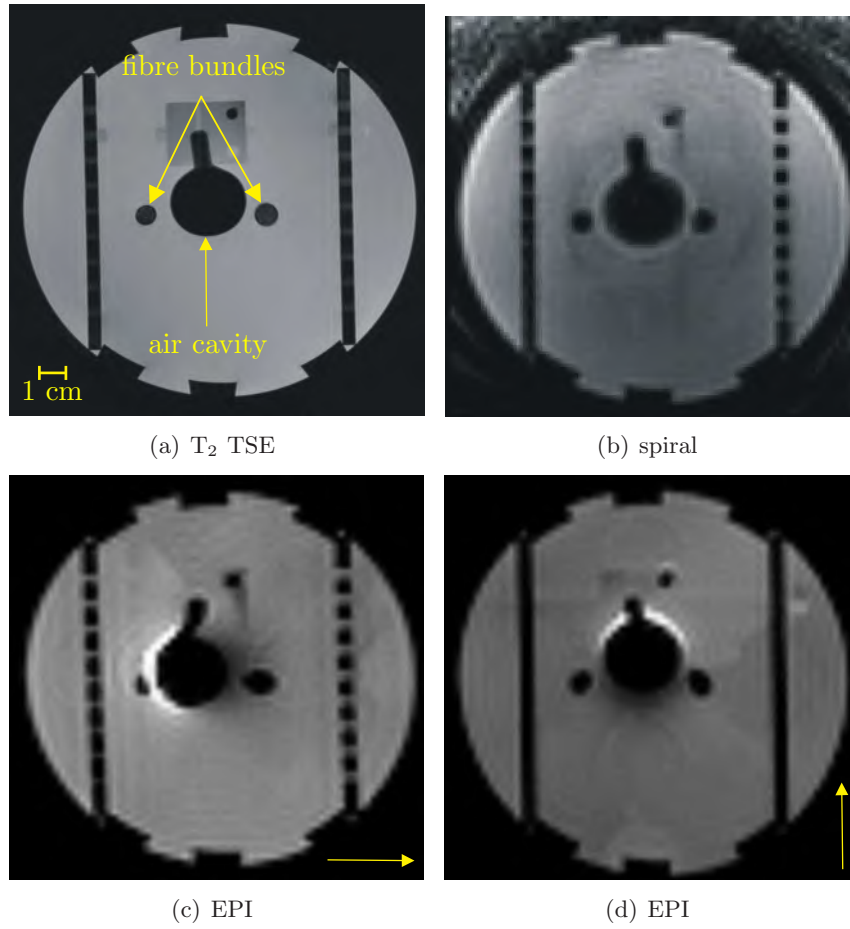
(d) EPI

Figure 6.1: MR images of a fibre phantom containing a spherical air cavity: (a) T$_2$ TSE ,(b) spiral, (c) and (d) EPI images, the phase-encoding direction is indicated by the arrow.

6.3   Head phantom

The feasibility of using an anthropomorphic head fibre phantom is discussed here.

Materials and methods

The constructed fibres as well as the corresponding *in vivo* fibre bundles in brain white matter are shown in figure 6.2. Fibre bundles with different diameters and geometries were constructed to imitate some of the major neural fibre tracts: corticospinal tracts, optical tracts, corpus callosum (forceps maior and minor) and fronto-occipital tracts (illustrated in figure 6.2).

For this experiment, fibre bundles were placed in a hydrogel consisting of 1.25 % (w/w) agarose and 0.275 mM Gd-DTPA to obtain T_1- and T_2-values similar to BWM. The hydrogel serves as a matrix to reduce flow artefacts. The fibre bundles were fixed in a plastic container with a shape as the human head. A hollow pipe imitating the trachea was also added (see figure 6.3).

DW-MRI was performed on a 3T Siemens Trio scanner using a birdcage head coil. The $\vec{k}$-space (explained in section 2.2.3) was sampled line by line (standard SE) with a bandwidth of 390 Hz/Px and 5 averages. TRSE diffusion gradients were applied in 12 directions with b-factors of 0 and 700 s/mm^2. The resolution was 2mm $\times$ 2mm $\times$ 2mm (128 $\times$ 128 matrix, 256 $\times$ 256 FOV, 2 mm slice thickness). A total of 10 slices was acquired for a TR of 300 ms with a TE of 60 ms.

Results

Figure 6.4 show T_1-weighted cross-sections of the brain in three orthogonal directions. Although images were scanned at a very short TE (4 ms), the signal in the fibre bundles is much lower in comparison to the signal of the hydrogel. Except for the corticospinal tract, the signal in the fibre bundles on the DWI's appeared to be too low to perform fibre tracking.

Figures 6.5(a) and 6.5(b) show FA-maps of slices through the corticospinal tracts and the forceps minor (figure 6.5(a)) and the forceps maior (figure 6.5(b)) of the corpus callosum. The reconstructed fibre tracts of the corticospinal tract are shown in figure 6.5(c). Measured FA was 0.321 ± 0.119 in the corticospinal tract.

(a) (b)

(c) (d)
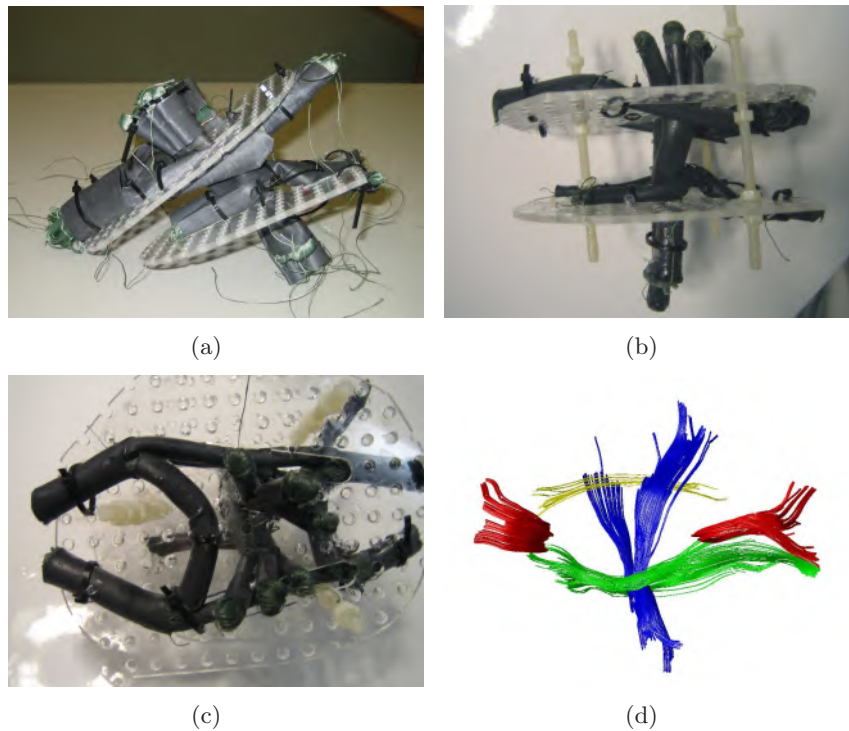
Figure 6.2: Fibre bundles inside the head phantom: (a) the fibre bundles before shrinking, (b) the fibre bundles after shrinking, (c) sight at the top (d) Illustration of the in vivo fibre tracts that served as a template for the construction of the head phantom. The blue fibre bundles represent the corticospinal tracts, the red fibre bundles represent the forceps maior and minor of the corpus callosum, the yellow fibre bundles represent the optical tracts and the green fibre bundles represent the fronto-occipital tracts.

(a)   (b)
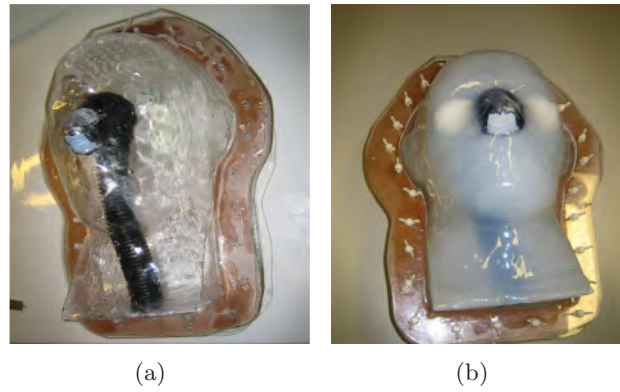
Figure 6.3: Head phantom: (a) a hollow pipe representing the trachea is positioned inside the phantom, (b) the phantom in his final form, filled with gel and the fibres inside.
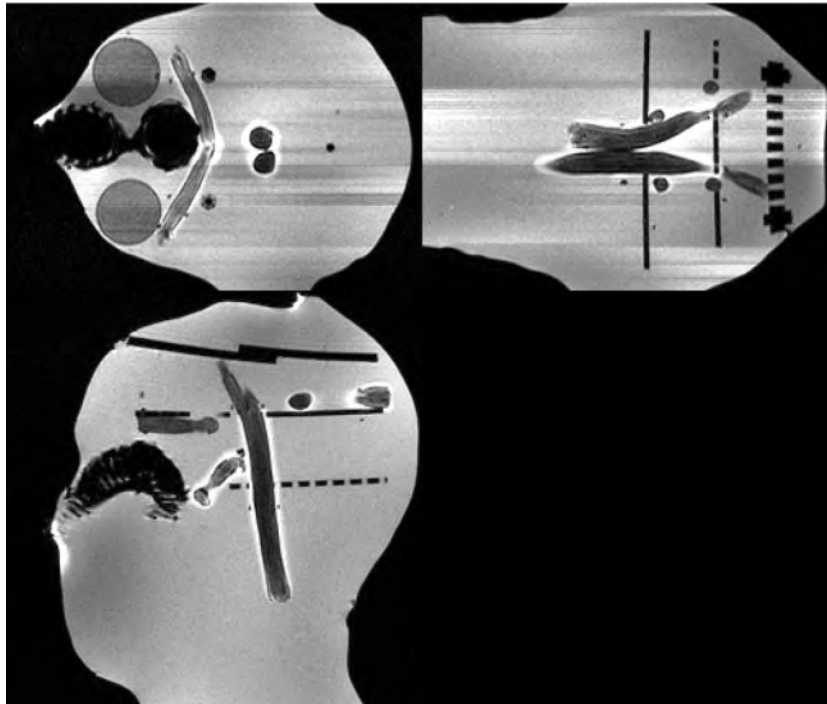
Figure 6.4: A coronal, sagittal and transversal cross-section of the head phantom. A T_1-weighted scan was performed with a TE of 4 ms and a TR of 12 ms. The signal in the fibre bundles is rather low.

(a) FA

(b) FA
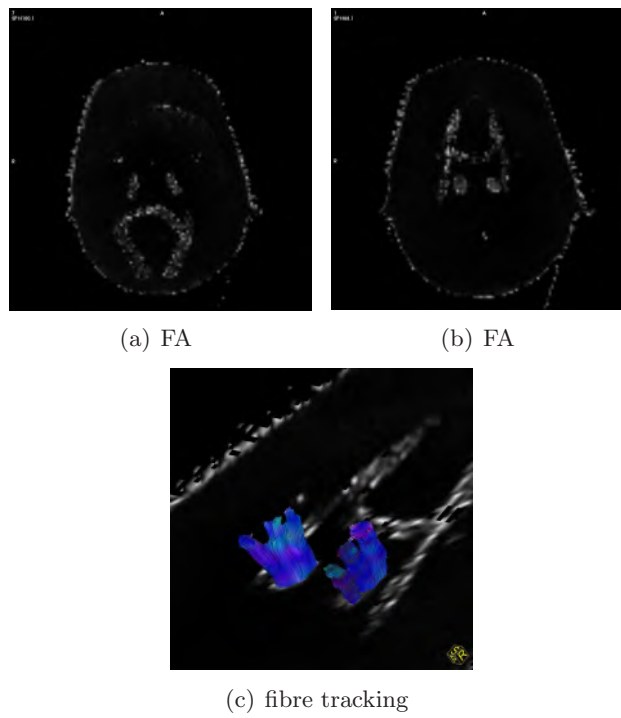
(c) fibre tracking

Figure 6.5: Result of DWI on the head phantom: (a), (b) FA-images of different slices of the head phantom. (c) fibre tracking of the corticospinal tract

Discussion

This study illustrates the feasibility of constructing a realistic anthropomorphic head phantom. There is a good agreement of the MR images (figures 6.4, 6.5(a) and 6.5(b)) and the constructed fibre tracts with reality.

When the gel composition was optimized in terms of T_1 and T_2, the effect of surface relaxation and internal magnetic gradients as described in chapter 3 was neglected. This resulted in a short overall T_2 and a corresponding low SNR as noticed in figure 6.4. Consequently, fibre tracking could not be performed, except for the corticospinal tracts in which the SNR was slightly higher. This is due to the fact that the corticospinal tracts run parallel to the static magnetic field $\vec{B}_0$ by which the effect of internal gradients is minimized (see section 3.4.2).

This study is rather a proof of concept to show the feasibility of manufacturing an anthropomorphic head phantom. The effect of internal gradients and surface relaxation as described in chapter 3 should be taken into account when fabricating realistic anthropomorphic diffusion head phantoms in the future.
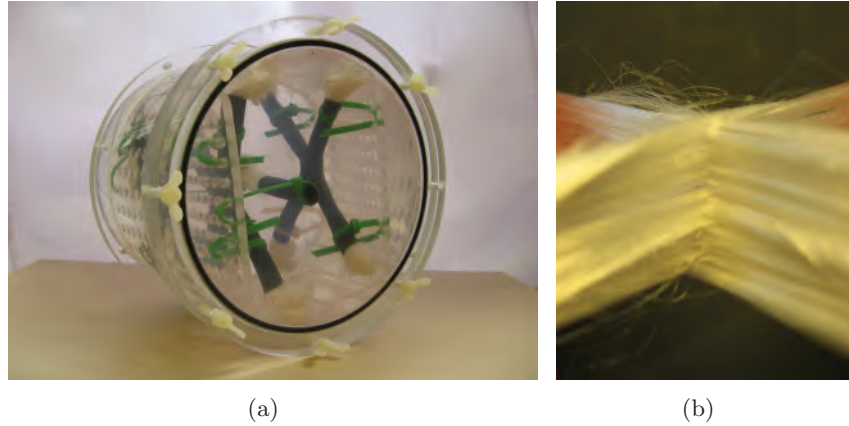
Figure 6.6: (a) Crossing fibre phantom and (b) illustration of the fibre crossing itself

6.4 A crossing fibre phantom for the validation of fibre tracking algorithms

The DT model is widely used to extract the main fibre direction in a voxel. However, the model fails in voxels with multiple fibre directions. The constrained spherical deconvolution (CSD) technique, based on the fibre orientation distribution function (ODF) (see section 2.4.3.3), has recently been proposed to overcome this limitation [67]. Crossing fibre phantoms were constructed as test objects for the validation of tractography methods in crossing fibres.

Materials and methods

A 90° crossing fibre phantom was made of Dyneema® fibres. The fibres were grouped in parallel bundles of 780 filaments which were crossed (see figure 6.6(b)), surrounded by a shrinking tube and submerged in water (see figure 6.6(a)).

DW-MRI was performed on a 3T Siemens Trio scanner using a knee birdcage coil. Diffusion weighted TRSE gradients were applied in 256 directions and a b-factor of 0 and 2500 s/mm^2 using an EPI read-out sequence with a band width of 1565 Hz/pixel. A total of 44 slices was acquired with a TR of 6.7 s and a TE of 109 ms. The resolution was 2 mm × 2 mm × 2 mm.

Fibre tractography was performed with a DTI streamline algo-
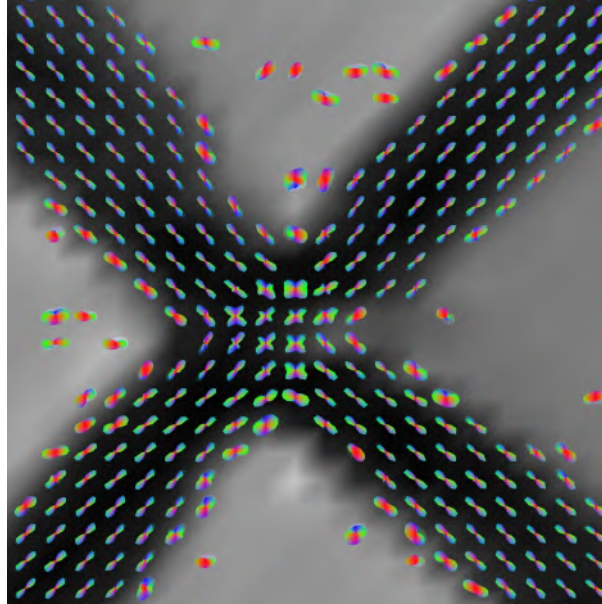
Figure 6.7: The estimated fibre orientation distribution function (ODF) is shown in each voxel as a surface rendered plot.

rithm [85] with the following parameters: step size = 1 mm, maximum angle = 70°, minimum FA = 0.1. Subsequently, the streamline algorithm was extended with CSD to extract multiple fibre orientations. The performance of CSD was compared with the original streamline algorithm.

Results

Figure 6.7 shows the estimated fibre ODF in a slice through the crossing fibre phantom. Two fibre directions are clearly noticed at the crossing. Figure 6.8(a) shows the results from DTI tractography using the streamline algorithm initiated in ROI 1 (green tracts) and ROI 2 (red tracts). At the intersection of both bundles, tracts turn left or right. The reconstructed fibre tracts are not in agreement with the actual phantom that only contains crossing fibres in that region. Figure 6.8(b) shows the tractography results of the CSD algorithm showing that the tracts run straight at the intersection of both bundles.
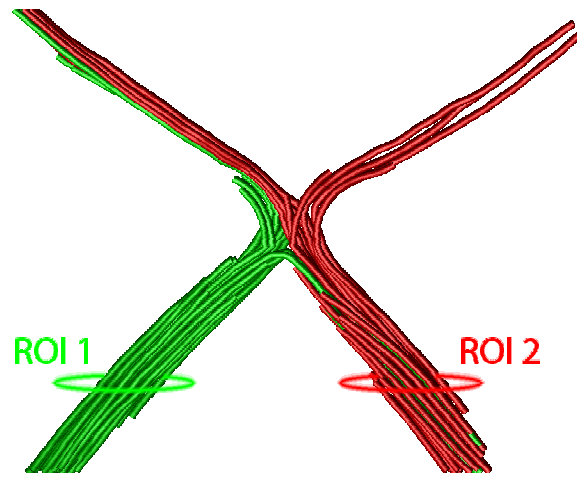
(a) DTI
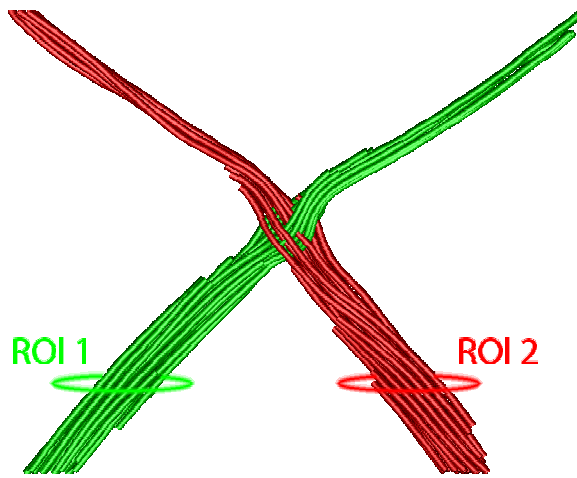
(b) CSD

Figure 6.8: Tractography results on the crossing fibre phantom using (a) diffusion tensor imaging (DTI) and (b) constrained spherical deconvolution (CSD).

Discussion

The use of a hardware crossing fibre phantom for testing fibre tractography algorithms is demonstrated here. In literature, fibre crossing phantoms made of rayon textile [117] and acrylic fibres [116] are also described for the validation of q-ball imaging. In [113], the use of both kissing and crossing fibre phantoms made of polyester fibres is discussed to evaluate the performance streamline and probabilistic fibre tracking algorithms.

The main advantages of using hardware crossing fibre phantoms are the well-known structure and the possibility of testing the effect of imaging parameters such as SNR. On the other hand, fibre phantoms containing tubular fibres as present in BWM instead of full fibres would come closer to the reality as mentioned in chapter 3.

6.5   Conclusion and original contributions

In this chapter, several potential applications for anisotropic fibre phantoms are discussed. Anisotropic fibre phantoms showed to be useful for sequence design, optimization and investigation of image artefacts. The feasibility of creating an anthropomorphic head phantom is demonstrated. The possibility of creating a crossing fibre phantom to evaluate the performance of fibre tracking algorithms is also mentioned. Fibre phantoms can also be used as a calibration standard in multi-centre studies and as a model for the validation of diffusion models (see chapter 5).

7
Overall Conclusion

The aim of this work was to develop methods for the validation of DW-MRI in WM, for sequence testing, for the validation of diffusion models and for the evaluation of fibre tractography algorithms. Both hardware and software diffusion phantoms are developed for this purpose. In this final chapter, we summarize the main contributions of this work and highlight some aspects for future study.

Chapter 2 introduces briefly the basic principles of MRI, DW-MRI, the diffusion in WM and its applications in clinic. DW-MRI shows potential in the examination of stroke, tumours, ageing and white matter diseases. The white matter anisotropy also enables fibre tractography, i.e. the reconstruction of neural fibre tracts.

Chapter 3 overviews the different kinds of hardware phantoms: isotropic versus anisotropic, biological versus synthetic. Synthetic anisotropic fibre bundles are proposed as phantoms for the validation of DW-MRI because of their well-known structure, their long preservability and the possibility to create complex geometries such as curved fibres and fibre crossings. The manufacturing process of the fibre bundles was optimized to create homogeneously packed fibre bundles in a reproducible way. The main factors influencing the outcome of the DW-MRI experiment were determined. On the one hand, the fibre density and fibre diameter are two important factors that determine the diffusion properties such as the fractional anisotropy (FA). On the other hand, the fibre material parameters of

surface relaxation and magnetic susceptibility determine the SNR.

With respect to the tested materials discussed in chapter 3, Dyneema® is found to be the most suited fibre material for testing DW-MRI because of the combination of a high FA and a reasonable SNR. Future work may include the study of other potential fibre materials to manufacture diffusion phantoms. Particularly capillaries are interesting to create more realistic phantoms imitating the diffusion in both the intra- and extracellular space of WM. The ideal fibre would be hollow, slightly hydrophilic with a small fibre diameter ($< 10~\mu$m) and a magnetic susceptibility close to water (-9 ppm).

In chapter 4, the anisotropic fibre bundles are shown to be useful experimental systems for validating analytical and computational diffusion models. The diffusion is modelled in the interstitial space between fibres by MC simulations of random walkers. The fibre phantoms can be considered as 2D porous media for which the diffusion can be described by analytical models. The MC simulations confirm the accuracy and validity of analytical models for ordered fibre packing geometries. The simulations in random packed fibre geometries show a higher FA and a longer transition time between the short and long-time diffusion limit in comparison with ordered packing geometries. The diffusion parameters (FA, ADC and ADK) in the interstitial space of fibre bundles were measured using DW-MRI and bulk NMR diffusion measurements. The measured diffusion parameters agree with those obtained through MC random walk simulations in media consisting of parallel randomly packed cylinders. Hence, the Dyneema® fibre bundles are appropriate for testing DW-MRI sequences and diffusion parameters on clinical MR-scanners quantitatively.

In chapter 5, the MC simulations were elaborated to model the diffusion in a geometry with intra- and extracellular compartments imitating WM. The results were compared with existing models for the DW-MRI signal in WM. A bi-exponential function fits the simulated DW-MRI signal accurately but the fitted values for the slow diffusion coefficient, the fast diffusion coefficient and corresponding volume fractions depend on the considered b-interval and diffusion time. Alternatively, the cumulant expansion form also fits the DW-MRI signal accurately. Moreover, the diffusion coefficient and kurtosis could be accurately fitted when including higher-order terms in the cumulant expansion form. The cumulant expansion form seemed to be less sensitive to noise than the bi-exponential model. The accuracy of the fitted parameters increases by including higher order terms

while the precision decreases. More research is required to determine the optimal order of the cumulant expansion form and b-interval in the presence of measured DW-MRI data.

The simulations also suggest that diffusion kurtosis maps may provide additional information to ADC- and FA-maps. The kurtosis showed to be a useful parameter to detect changes in membrane permeability. It might be interesting to correlate the kurtosis against the observed changes in ADC in pathologies such as stroke and malignant tumours to the underlying cell physiology.

Chapter 6 illustrates some potential applications for Dyneema® fibre phantoms. Because of their well-known structure and anisotropy, they show to be useful for sequence design, optimization and investigation of the effect of image artefacts. We have illustrated the potential use for the evaluation of artefacts when comparing MR-sequences with a standard EPI readout and a spiral readout. The large variety of available shrinking tubes with different shapes and sizes enables the construction of an anthropomorphic head phantom. When fabricating realistic head phantoms, the effect of surface relaxivity and magnetic susceptibility should be incorporated when determining the gel composition in terms of T_1 and T_2 relaxation times. The FA-values in the fibre bundles is high enough to perform fibre tracking and showed therefore helpful in testing fibre tractography algorithms. The possibility of creating a crossing fibre phantom to evaluate the performance of fibre tracking algorithms is demonstrated.

It is our hope that the design of both hardware diffusion phantoms and synthetic phantoms and the methodological developments set out in this thesis will be helpful for ongoing work on the validation of DW-MRI. Future work may involve the fabrication of a fibre phantom that can serve as a daily reproducible reference measurement for DW-MRI and for the investigation of systematic errors in FA and other diffusion parameters. The fibre phantoms may also be applied as a calibration standard in multi-centre studies. Future work should also investigate in more detail the usefulness of the kurtosis as a sensitive parameter to detect cell pathological changes and its potential for clinical applications.

References

[1] P.T. Callaghan. *Principles of nuclear magnetic resonance microscopy*. Oxford University Press, 1991.

[2] E. Haacke, R. Brown, M. Thompson, and R. Venkatesan. *Magnetic Resonance Imaging: Physical Principles and Sequence Design*. Wiley-Liss, New York, Chichester, 1999.

[3] M. Bernstein, K. King, and X. Zhou. *Handbook of MRI pulse sequences*. Elsevier Academic press, Amsterdam, 2004.

[4] M.T. Vlaardingerbroek and J.A. den Boer. *Magnetic Resonance Imaging: Theory and Practice*. Springer-Verlag, Berlin, 1999.

[5] E. M. Purcell, H. C. Torrey, and R. V. Pound. *Resonance Absorption by Nuclear Magnetic Moments in a Solid*. Physical Review, 69(1-2):37–38, 1946.

[6] F. Bloch. *Nuclear Induction*. Physical Review, 70(7-8):460–474, 1946.

[7] P. C. Lauterbur. *Image Formation by Induced Local Interactions: Examples Employing Nuclear Magnetic Resonance*. Nature, 242(5394):190–191, 1973.

[8] P. Mansfield. *Multi-planar image formation using NMR spin echoes*. Journal of Physics C: Solid State Physics, 10(3):L55–L58, 1977.

[9] N. Bloembergen, E. M. Purcell, and R. V. Pound. *Relaxation Effects in Nuclear Magnetic Resonance Absorption*. Physical Review, 73(7):679–712, 1948.

[10] S. J. Mears, T. Cosgrove, L. Thompson, and I. Howell. *Solvent Relaxation NMR Measurements on Polymer, Particle, Surfactant Systems*. Langmuir, 14(5):997–1001, 1998.

[11]   P. Tofts. *Quantitative MRI of the brain, Measuring Changes Caused by Disease.* John Wiley and Sons, Chichester, UK, 2003.

[12]   E. L. Hahn. *Spin Echoes.* Physical Review, 80(4):580–594, 1950.

[13]   G. H. Glover. *Simple analytic spiral K-space algorithm.* Magnetic Resonance in Medicine, 42(2):412–415, 1999.

[14]   R. G. Nunes, P. Jezzard, and S. Clare. *Investigations on the efficiency of cardiac-gated methods for the acquisition of diffusion-weighted images.* Journal of Magnetic Resonance, 177(1):102–110, 2005.

[15]   R. Brown. *A brief account of microscopical observations made in the months of June, July, and August, 1827, on the particles contained in the pollen of plants; and on the general existence of active molecules in organic and inorganic bodies.* Philospohical Magazine, 4:161–173, 1828.

[16]   A. Einstein. *Über die von der molekularkinetischen Theorie der Wärme gefordete Bewegung von in ruhenden Flüssigkeiten suspendierten Teilchen".* Annals of Physics, 4:549–560, 1905.

[17]   E. Ozarslan, P. J. Basser, T. M. Shepherd, P. E. Thelwall, B. C. Vemuri, and S. J. Blackband. *Observation of anomalous diffusion in excised tissue by characterizing the diffusion-time dependence of the MR signal.* Journal of Magnetic Resonance, 183(2):315–323, 2006.

[18]   M. J. Saxton. *Anomalous diffusion due to binding: a Monte Carlo study.* Biophys J, 70(3):1250–1262, 1996.

[19]   S. Havlin and D. Ben-Avraham. *Diffusion in disordered media.* Advance in Physics, 36(6):695–798, 1987.

[20]   A. Peters, S.L. Palay, and H.D. Webster. *The fine structure of the Nervous system.* Oxford University Press, New York Oxford, 1991.

[21]   A. S. Lamantia and P. Rakic. *Cytological and quantitative characteristics of four cerebral commissures in the rhesus monkey.* The Journal of comparative neurology, 291(4):520–537, 1990.

[22]   D. Le Bihan, E. Breton, D. Lallemand, P. Grenier, E. Cabanis, and M. Laval-Jeantet. *MR imaging of intravoxel incoherent*

motions: application to diffusion and perfusion in neurologic disorders. Radiology, 161(2):401–407, 1986.

[23] T. L. Chenevert, J. A. Brunberg, and J. G. Pipe. *Anisotropic diffusion in human white matter: demonstration with MR techniques in vivo.* Radiology, 177(2):401–405, 1990.

[24] M. E. Moseley, Y. Cohen, J. Kucharczyk, J. Mintorovitch, H. S. Asgari, M. F. Wendland, J. Tsuruda, and D. Norman. *Diffusion-weighted MR imaging of anisotropic water diffusion in cat central nervous system.* Radiology, 176(2):439–445, 1990.

[25] R. Turner, D. Le Bihan, J. Maier, R. Vavrek, L. K. Hedges, and J. Pekar. *Echo-planar imaging of intravoxel incoherent motion.* Radiology, 177(2):407–414, 1990.

[26] D. Le Bihan. *Looking into the functional architecture of the brain with diffusion MRI.* Nature Reviews Neuroscience, 4(6):469–480, 2003.

[27] C. Beaulieu. *The basis of anisotropic water diffusion in the nervous system - a technical review.* NMR in Biomedicine, 15(7-8):435–455, 2002.

[28] L. Minati and W. P. Weglarz. *Physical foundations, models, and methods of diffusion magnetic resonance imaging of the brain: A review.* Concepts in Magnetic Resonance Part A, 30A(5):278–307, 2007.

[29] C. Nicholson and E. Syková. *Extracellular space structure revealed by diffusion analysis.* Trends Neurosci, 21(5):207–215, 1998.

[30] P. S. Tofts, D. Lloyd, C. A. Clark, G. J. Barker, G. J. M. Parker, P. McConville, C. Baldock, and J. M. Pope. *Test liquids for quantitative MRI measurements of self-diffusion coefficient in vivo.* Magnetic Resonance in Medicine, 43(3):368–374, 2000.

[31] Y. Assaf and Y. Cohen. *Detection of Different Water Populations in Brain Tissue Using 2H Single- and Double-Quantum-Filtered Diffusion NMR Spectroscopy.* Journal of Magnetic Resonance, Series B, 112(2):151–159, 1996.

[32] C. Nicholson and J. M. Phillips. *Ion diffusion modified by tortuosity and volume fraction in the extracellular microenvironment*

of the rat cerebellum. The Journal of physiology, 321:225–257, 1981.

[33] D. Le Bihan. *The 'wet mind': water and functional neuroimaging.* Physics Medicine Biology, 52(7):57–90, 2007.

[34] H. Y. Carr and E. M. Purcell. *Effects of Diffusion on Free Precession in Nuclear Magnetic Resonance Experiments.* Physical Review, 94:630–638, 1954.

[35] D. E. Woessner. *Effects of Diffusion in Nuclear Magnetic Resonance Spin-Echo Experiments.* Journal of Chemical Physics, 34:2057–2061, 1961.

[36] D. E. Woessner. *Nuclear Spin Relaxation in Ellipsoids Undergoing Rotational Brownian Motion.* The Journal of Chemical Physics, 37(3):647–654, 1962.

[37] E. O. Stejskal. *Use of Spin Echoes in a Pulsed Magnetic-Field Gradient to Study Anisotropic, Restricted Diffusion and Flow.* Journal of Chemical Physics, 43(10):3597–3603, 1965.

[38] W. S. Price. *Pulsed-field gradient nuclear magnetic resonance as a tool for studying translational diffusion: part I. Basic theory.* Concepts in Magnetic Resonance, 9(5):299–336, 1997.

[39] L. Z. Wang, A. Caprihan, and E. Fukushima. *The Narrow-Pulse Criterion for Pulsed-Gradient Spin-Echo Diffusion Measurements.* Journal of Magnetic Resonance, Series A, 117(2):209–219, 1995.

[40] T. G. Reese, O. Heid, R. M. Weisskoff, and V. J. Wedeen. *Reduction of eddy-current-induced distortion in diffusion MRI using a twice-refocused spin echo.* Magnetic Resonance in Medicine, 49(1):177–182, 2003.

[41] G. Zheng and W. S. Price. *Suppression of background gradients in (B_0 gradient-based) NMR diffusion experiments.* Concepts in Magnetic Resonance Part A, 30A(5):261–277, 2007.

[42] R. M. Cotts, Sun T. Hoch, M.J.R., and Markert J.T. *Pulsed field gradient stimulated echo methods for improved NMR diffusion measurements in heterogeneous systems.* Journal of Magnetic Resonance, 83(2):252 –266, 1989.

[43] P. J. Basser, J. Mattiello, and D. Le Bihan. *Estimation of the effective self-diffusion tensor from the NMR spin echo.* Journal of Magnetic Resonance Series B, 103(3):247–254, 1994.

[44] L. C. Chang, D. K. Jones, and C. Pierpaoli. *RESTORE: robust estimation of tensors by outlier rejection.* Magnetic Resonance in Medicine, 53(5):1088–1095, 2005.

[45] J. F. Mangin, C. Poupon, C. Clark, D. Le Bihan, and I. Bloch. *Distortion correction and robust tensor estimation for MR diffusion imaging.* Medical Image Analysis, 6(3):191–198, 2002.

[46] P. J. Basser, J. Mattiello, and D. Lebihan. *MR diffusion tensor spectroscopy and imaging.* Biophysical Journal, 66(1):259–267, 1994.

[47] P. J. Basser and C. Pierpaoli. *Microstructural and physiological features of tissues elucidated by quantitative-diffusion-tensor MRI.* Journal of Magnetic Resonance B, 111(3):209–219, 1996.

[48] C. Pierpaoli and P. J. Basser. *Toward a quantitative assessment of diffusion anisotropy.* Magnetic Resonance in Medicine, 36(6):893–906, 1996.

[49] N. G. Papadakis, D. Xing, C. L. Huang, L. D. Hall, and A. T. Carpenter. *A Comparative Study of Acquisition Schemes for Diffusion Tensor Imaging Using MRI.* Journal of Magnetic Resonance, 137(1):67–82, 1999.

[50] C. F. Westin, S. E. Maier, H. Mamata, A. Nabavi, F. A. Jolesz, and R. Kikinis. *Processing and Visualization of Diffusion Tensor MRI.* Medical Image Analysis, 6(2):93–108, 2002.

[51] C. Pierpaoli, P. Jezzard, P. J. Basser, A. Barnett, and G. Di Chiro. *Diffusion tensor MR imaging of the human brain.* Radiology, 201(3):637–648, 1996.

[52] D. K. Jones, M. A. Horsfield, and A. Simmons. *Optimal strategies for measuring diffusion in anisotropic systems by magnetic resonance imaging.* Magnetic Resonance in Medicine, 42(3):515–525, 1999.

[53] S. Skare, M. Hedehus, M. E. Moseley, and T. Q. Li. *Condition number as a measure of noise performance of diffusion tensor data*

acquisition schemes with MRI. Journal of Magnetic Resonance, 147(2):340–352, 2000.

[54] K. M. Hasan, D. L. Parker, and A. L. Alexander. *Comparison of gradient encoding schemes for diffusion-tensor MRI.* Journal of Magnetic Resonance Imaging, 13(5):769–780, 2001.

[55] D. K. Jones. *The effect of gradient sampling schemes on measures derived from diffusion tensor MRI: A Monte Carlo study.* Magnetic Resonance in Medicine, 51(4):807–815, 2004.

[56] T. E. Conturo, R. C. McKinstry, E. Akbudak, and B. H. Robinson. *Encoding of anisotropic diffusion with tetrahedral gradients: a general mathematical diffusion formalism and experimental results.* Magnetic Resonance in Medicine, 35(3):399–412, 1996.

[57] T. Niendorf, R. M. Dijkhuizen, D. G. Norris, M. van Lookeren Campagne, and K. Nicolay. *Biexponential diffusion attenuation in various states of brain tissue: implications for diffusion-weighted imaging.* Magnetic Resonance in Medicine, 36(6):847–857, 1996.

[58] Y. Assaf and Y. Cohen. *Non-Mono-Exponential Attenuation of Water and N-Acetyl Aspartate Signals Due to Diffusion in Brain Tissue.* Journal of Magnetic Resonance, 131(1):69–85, 1998.

[59] R. V. Mulkern, H. P. Zengingonul, R. L. Robertson, P. Bogner, K. H. Zou, H. Gudbjartsson, C. R. Guttmann, D. Holtzman, W. Kyriakos, F. A. Jolesz, and S. E. Maier. *Multi-component apparent diffusion coefficients in human brain: relationship to spin-lattice relaxation.* Magnetic Resonance in Medicine, 44(2):292–300, 2000.

[60] D. S. Tuch, T. G. Reese, M. R. Wiegell, N. Makris, J. W. Belliveau, and V. J. Wedeen. *High angular resolution diffusion imaging reveals intravoxel white matter fiber heterogeneity.* Magnetic Resonance in Medicine, 48(4):577–582, 2002.

[61] V. G. Kiselev and K. A. IlÝasov. *Is the "biexponential diffusion" biexponential?* Magnetic Resonance in Medicine, 57(3):464–469, 2007.

[62] J. H. Jensen, J. A. Helpern, A. Ramani, H. Lu, and K. Kaczynski. *Diffusional kurtosis imaging: the quantification of non-*

gaussian water diffusion by means of magnetic resonance imaging. Magnetic Resonance in Medicine, 53(6):1432–1440, 2005.

[63] A. F. Fröhlich, L. Östergaard, and V. G. Kiselev. *Effect of impermeable boundaries on diffusion-attenuated MR signal.* Journal of Magnetic Resonance, 179:223–233, 2006.

[64] P. T. Callaghan, C. D. Eccles, and Y. Xia. *NMR microscopy of dynamic displacements: k-space and q-space imaging.* Journal of Physics E: Scientific Instruments, 21(8):820–822, 1988.

[65] D. G. Cory and A. N. Garroway. *Measurement of translational displacement probabilities by NMR: an indicator of compartmentation.* Magnetic Resonance in Medicine, 14(3):435–444, 1990.

[66] J.-D. Tournier, F. Calamante, D. G. Gadian, and A. Connelly. *Direct estimation of the fiber orientation density function from diffusion-weighted MRI data using spherical deconvolution.* NeuroImage, 23(3):1176–1185, 2004.

[67] J-D. Tournier, F. Calamante, and A. Connelly. *Robust determination of the fibre orientation distribution in diffusion MRI: Non-negativity constrained super-resolved spherical deconvolution.* NeuroImage, 35(4):1459–1472, 2007.

[68] L. R. Frank. *Characterization of anisotropy in high angular resolution diffusion-weighted MRI.* Magnetic Resonance in Medicine, 47(6):1083–1099, 2002.

[69] P. J. Basser. *Relationships between diffusion tensor and q-space MRI.* Magnetic Resonance in Medicine, 47(2):392–397, 2002.

[70] C. Liu, R. Bammer, and M. E. Moseley. *Limitations of apparent diffusion coefficient-based models in characterizing non-gaussian diffusion.* Magnetic Resonance in Medicine, 54(2):419–428, 2005.

[71] D. S. Tuch. *Q-ball imaging.* Magnetic Resonance in Medicine, 52(6):1358–1372, 2004.

[72] Kevin M. Bennett, Kathleen M. Schmainda, Raoqiong B. (tong), Daniel B. Rowe, Hanbing Lu, and James S. Hyde. *Characterization of continuously distributed cortical water diffusion rates with a stretched-exponential model.* Magnetic Resonance in Medicine, 50(4):727–734, 2003.

[73] M. G. Hall and T. R. Barrick. *From diffusion-weighted MRI to anomalous diffusion imaging.* Magnetic Resonance in Medicine, 59(3):447–455, 2008.

[74] P. Mürtz, C. Krautmacher, F. Träber, J. Gieseke, H. Schild, and W. Willinek. *Diffusion-weighted whole-body MR imaging with background body signal suppression: a feasibility study at 3.0 Tesla.* European Radiology, 17(12):3031–3037, 2007.

[75] D. W. Townsend. *Multimodality imaging of structure and function.* Physics in medicine and biology, 53(4):R1–R39, 2008.

[76] W. Hacke and S. Warach. *Diffusion-weighted MRI as an evolving standard of care in acute stroke.* Neurology, 54(8):1548–1549, 2000.

[77] C.H. Sotak. *Nuclear magnetic resonance (NMR) measurement of the apparent diffusion coefficient (ADC) of tissue water and its relationship to cell volume changes in pathological states.* Neurochemistry International, 45(4):569–582, 2004.

[78] J. Neil, J. Miller, P. Mukherjee, and P. S. Hüppi. *Diffusion tensor imaging of normal and injured developing human brain - a technical review.* NMR in Biomedicine, 15(7-8):543–552, 2002.

[79] M. Moseley. *Diffusion tensor imaging and aging - a review.* NMR in Biomedicine, 15(7-8):553–560, 2002.

[80] M. A. Horsfield and D. K. Jones. *Applications of diffusion-weighted and diffusion tensor MRI to white matter diseases - a review.* NMR in Biomedicine, 15(7-8):570–577, 2002.

[81] K. O. Lim and J. A. Helpern. *Neuropsychiatric applications of DTI - a review.* NMR in biomedicine, 15(7-8):587–593, 2002.

[82] S. Mori, S. Wakana, l. M. Nagae-Poetscher, and P.C.M. van Zijl. *MRI Atlas of Human White Matter.* Elsevier, Amsterdam, the Netherlands, 2005.

[83] A. Leemans. *Modeling and Processing of Diffusion Tensor Magnetic Resonance Images for Improved Analysis of Brain Connectivity.* PhD thesis, Universiteit Antwerpen, Belgium, 2006.

[84] J.D. Clayden. *Comparative Analysis of Connection and Disconnection in the Human Brain Using Diffusion MRI: New Methods*

and Applications. PhD thesis, University of Edingburgh, UK, 2008.

[85] P. J. Basser, S. Pajevic, C. Pierpaoli, J. Duda, and A. Aldroubi. *In vivo fiber tractography using DT-MRI data.* Magnetic Resonance in Medicine, 44(4):625–632, 2000.

[86] S. Mori and P. C. van Zijl. *Fiber tracking: principles and strategies - a technical review.* NMR in Biomedicine, 15(7-8):468–480, 2002.

[87] A. Leemans, J. Sijbers, M. Verhoye, A. Van der Linden, and D. Van Dyck. *Mathematical framework for simulating diffusion tensor MR neural fiber bundles.* Magnetic Resonance in Medicine, 53(4):944–953, 2005.

[88] M. E. Bastin and P. A. Armitage. *On the use of water phantom images to calibrate and correct eddy current induced artefacts in MR diffusion tensor imaging.* Magnetic Resonance Imaging, 18(6):681–687, 2000.

[89] G. Steidle and F. Schick. *Echoplanar diffusion tensor imaging of the lower leg musculature using eddy current nulled stimulated echo preparation.* Magnetic Resonance in Medicine, 55(3):541–548, 2006.

[90] K.M. Hasan, A.L. Alexander, and P.A. Narayana. *Does fractional anisotropy have better noise immunity characteristics than relative anisotropy in diffusion tensor MRI? An analytical approach.* Magnetic Resonance in Medicine, 51:413–417, 2004.

[91] H. J. Laubach, P. M. Jakob, K. O. Loevblad, A. E. Baird, M. P. Bovo, R. R. Edelman, and S. Warach. *A phantom for diffusion-weighted imaging of acute stroke.* Journal of Magnetic Resonance Imaging, 8(6):1349–1354, 1998.

[92] I. Delakis, E. M. Moore, M. O. Leach, and J. P. De Wilde. *Developing a quality control protocol for diffusion imaging on a clinical MRI system.* Physics Medicine Biology, 49(8):1409–1422, 2004.

[93] M. Holz, S.R. Heil, and A. Sacco. *Temperature-dependent self-diffusion coefficients of water and six selected molecular liquids for calibration in accurate ^1H NMR PFG measurements.* Physical Chemistry Chemical Physics, 2:4740–4742, 2000.

[94] B. Hills. *Magnetic Resonance Imaging in Food Science.* John
      Wiley and Sons, New York, USA, 1998.

[95] D. Gullmar, T. Jaap, M. E. Bellemann, J. Haueisen, and J. R.
      Reichenbach. *DTI measurements of isotropic and anisotropic me-*
      dia. Biomedizinische Technik (Berlin), 47 Suppl 1 Pt 1:420–422,
      2002.

[96] M. Neeman, J. P. Freyer, and L. O. Sillerud. *A simple method*
      for obtaining cross-term-free images for diffusion anisotropy stud-
      ies in NMR microimaging. Magnetic Resonance in Medicine,
      21(1):138–143, 1991.

[97] J. D. Trudeau, W. T. Dixon, and J. Hawkins. *The Effect of*
      Inhomogeneous Sample Susceptibility on Measured Diffusion Ani-
      sotropy Using NMR Imaging. Journal of Magnetic Resonance B,
      108(1):22–30, 1995.

[98] S. Boujraf, R. Luypaert, H. Eisendrath, and M. Osteaux. *Echo*
      planar magnetic resonance imaging of anisotropic diffusion in as-
      paragus stems. Magnetic Resonance Materials in Physics, Biology
      and Medicine, 13:82–90, 2001.

[99] E. E. Sigmund and Y.-Q. Song. *Multiple echo diffusion ten-*
      sor acquisition technique. Magnetic Resonance Imaging, 24:7–18,
      2006.

[100] J. Lätt, M. Nilsson, A. Rydhög, R. Wirestam, F. Ståhlberg,
      and S. Brockstedt. *Effects of restricted diffusion in a biological*
      phantom: a q-space diffusion MRI study of asparagus stems at a
      3T clinical scanner. Magnetic Resonance Materials in Physics,
      Biology and Medicine, 20(4):213–222, 2007.

[101] S. Madi, K. M. Hasan, and P. A. Narayana. *Diffusion tensor*
      imaging of in vivo and excised rat spinal cord at 7 T with an
      icosahedral encoding scheme. Magnetic Resonance in Medicine,
      53(1):118–125, 2005.

[102] J. S. Campbell, K. Siddiqi, V. V. Rymar, A. F. Sadikot, and
      G. B. Pike. *Flow-based fiber tracking with diffusion tensor and*
      q-ball data: validation and comparison to principal diffusion di-
      rection techniques. Neuroimage, 27(4):725–736, 2005.

[103] Y. Assaf, R. Z. Freidlin, G. K. Rohde, and P. J. Basser. *New modeling and experimental framework to characterize hindered and restricted water diffusion in brain white matter.* Magnetic Resonance in Medicine, 52(5):965–978, 2004.

[104] M. Descoteaux, E. Angelino, S. Fitzgibbons, and R. Deriche. *Apparent diffusion coefficients from high angular resolution diffusion imaging: estimation and applications.* Magnetic Resonance in Medicine, 56(2):395–410, 2006.

[105] R. Z. Freidlin, E. Ozarslan, M. E. Komlosh, L. C. Chang, C. G. Koay, D. K. Jones, and P. J. Basser. *Parsimonious Model Selection for Tissue Segmentation and Classification Applications: A Study Using Simulated and Experimental DTI Data.* IEEE Transactions on Medical Imaging, 26(11):1576–1584, 2007.

[106] N. Yanasak and J. Allison. *Use of capillaries in the construction of an MRI phantom for the assessment of diffusion tensor imaging: demonstration of performance.* Magnetic Resonance Imaging, 24(10):1349–1361, 2006.

[107] E. A. H. von dem Hagen and R. M. Henkelman. *Orientational diffusion reflects fiber structure within a voxel.* Magnetic Resonance in Medicine, 48(3):454–459, 2002.

[108] C.-P. Lin, J. Van Wedeen, J.-H. Chen, C. Yao, and W.-Y. I. Tseng. *Validation of diffusion spectrum magnetic resonance imaging with manganese-enhanced rat optic tracts and ex vivo phantoms.* NeuroImage, 19(3):482–495, 2003.

[109] K.H. Cho, C.H. Yeh, Y.P. Chao, J.H. Chen, and C.P. Lin. *Accuracy assessment of q-ball imaging with phantom models.* In Proceedings of the International Society for Magnetic Resonance in Medicine 14th scientific meeting, page 642, Seattle, USA, 2006.

[110] L. G. Raguin, D. Hernando, D. Karampinos, L. Ciobanu, B. P. Sutton, Z.-P. Liang, and J. G. Georgiadis. *Quantitative analysis of q-space MRI data: theoretical and experimental validation.* In Proceedings of the International Society for Magnetic Resonance in Medicine 14th scientific meeting, page 2729, Seattle, USA, 2006.

[111] R. Lorenz, B. W. Kreher, Hennig J., M. E. Belleman, and K. A. Il'Yasov. *Anisotropic fiber phatom for DTI validation on a clinical scanner.* In Proceedings of the International Society

for Magnetic Resonance in Medicine 14th scientific meeting, page 2738, Seattle, USA, 2006.

[112]   F. B. Laun, B. Stieltjes, S. Huff, and Schad L. R. *Investigation of a DTI-phantom with properties similar to in vivo neuronal tissue.* In Proceedings of the International Society for Magnetic Resonance in Medicine 15th scientific meeting, page 1526, Berlin,Ge, 2007.

[113]   W. L. Pullens, A. Roebroeck, and R. Goebel. *Kissing or crossing: validation of DTI tractography in ground thruth hardware phantoms.* In Proceedings of the International Society for Magnetic Resonance in Medicine 15th scientific meeting, page 1479, Berlin,Ge, 2007.

[114]   E. Fieremans, S. Delputte, K. Deblaere, Y. De Deene, B. Truyens, Y. D'Asseler, E. Achten, I. Lemahieu, and R. Van de Walle. *A flexible hardware phantom for validation of diffusion imaging sequences.* In Abstracts of the International Society for Magnetic Resonance in Medicine, thirteenth scientific meeting & exhibition, page 1309, Miami Beach, 2005.

[115]   C. Reischauer, P. Staempfli, T. Jaermann, S. Kollias, and P. Boesiger. *Development of a temperature controlled anisotropic diffusion phantom.* In Proceedings of the International Society for Magnetic Resonance in Medicine 15th scientific meeting, page 3535, Berlin,Ge, 2007.

[116]   C. Poupon, B. Rieul, M. Perrin, J.-F. Mangin, and LeBihan D. *New diffusion phantoms dedicated to study and validation of HARDI diffusion models.* In Proceedings of the International Society for Magnetic Resonance in Medicine 15th scientific meeting, page 907, Berlin,Ge, 2007.

[117]   M. Perrin, C. Poupon, B. Rieul, P. Leroux, A. Constantinesco, J.-F. Mangin, and D. Le Bihan. *Validation of q-ball imaging with a diffusion fibre-crossing phantom on a clinical scanner.* Philosophical Transactions of the Royal Soeciety B-Biological Sciences, 360(1457):881–891, 2005.

[118]   Y. De Deene, N. Reynaert, and C. De Wagter. *On the accuracy of monomer/polymer gel dosimetry in the proximity of a high-dose-rate 192Ir source.* Physics in Medicine and Biology, 46(11):2801–2825, 2001.

[119] R. L. Kleinberg and J. A. Jackson. *An introduction to the history of NMR well logging.* Concepts in Magnetic Resonance, 13(6):340–342, 2001.

[120] R. L. Kleinberg. *Utility of NMR T2 distributions, connection with capillary pressure, clay effect, and determination of the surface relaxivity parameter rho2.* Magnetic Resonance Imaging, 14:761–767, 1996.

[121] W. F. Slijkerman and J. P. Hofman. *Determination of surface relaxivity from NMR diffusion measurements.* Magnetic Resonance Imaging, 16(5-6):541–544, 1998.

[122] J. Chen, G. J. Hirasaki, and M. Flaum. *NMR wettability indices: Effect of OBM on wettability and NMR responses.* Journal of Petroleum Science and Engineering, 52(1-4):161–171, 2006.

[123] G. Chen and H. Zhu. *Bacterial adhesion to silica sand as related to Gibbs energy variations.* Colloids Surf B Biointerfaces, 44(1):41–48, 2005.

[124] T. Englander, D. Wiegel, L. Naji, and K. Arnold. *Dehydration of Glass Surfaces Studied by Contact Angle Measurements.* Journal of Colloid and Interface Science, 179(2):635–636, 1996.

[125] N. Lopattananon, A. P. Kettle, D. Tripathi, A. J. Beck, E. Duval, R. M. France, R. D. Short, and F. R. Jones. *Interface molecular engineering of carbon-fiber composites.* Composites Part A: Applied Science and Manufacturing, 30(1):49–57, 1999.

[126] G. C. Borgia, R. J. Brown, and P. Fantazzini. *Scaling of spin-echo amplitudes with frequency, diffusion coefficient, pore size, and susceptibility difference for the NMR of fluids in porous media and biological tissues.* Physical Review E, 51(3):2104+, 1995.

[127] J. F. Schenck. *The role of magnetic susceptibility in magnetic resonance imaging: MRI magnetic compatibility of the first and second kinds.* Medical Physics, 23(6):815–850, 1996.

[128] Y. Nishiyama and T. Terao. *γ-Encoding transform NMR for uniaxially oriented samples.* Chemical Physics Letters, 352(5-6):479–485, 2002.

[129] M. Rákoš, Z. Varga, and R. Šimo. *Magnetic study of changes in the arranged contribution in polyamide fibres.* Czechoslovak Journal of Physics, 18(11):1456–1462, 1968.

[130] M. E. Stoll and T. J. Majors. *Reduction of magnetic susceptibility broadening in NMR by susceptibility matching.* Journal of Magnetic Resonance (1969), 46(2):283–288, 1982.

[131] D.R. Lide. *CRC Handbook of Chemistry and Physics, 88th edition.* CRC press, Boca Raton New York, 2003.

[132] L. L. Latour, P. P. Mitra, R. L. Kleinberg, and C. H. Sotak. *Time-Dependent Diffusion Coefficient of Fluids in Porous Media as a Probe of Surface-to-Volume Ratio.* Journal of Magnetic Resonance Series A, 101(3):342–346, 1993.

[133] R. W. Mair, P. N. Sen, M. D. Hürlimann, S. Patz, D. G. Cory, and R. L. Walsworth. *The narrow pulse approximation and long length scale determination in xenon gas diffusion NMR studies of model porous media.* Journal of Magnetic Resonance, 156(2):202–212, 2002.

[134] M.D. Hürlimann, K.G. Helmer, L.L. Latour, and C.H. Sotak. *Restricted diffusion in sedimentary rocks. Determination of surface-to-volume ratio and surface relaxivity.* Journal of Magnetic Resonance Series A, 111:169–178, 1994.

[135] Y.-Q. Song. *Determining pore sizes using an internal magnetic field.* Journal of Magnetic Resonance, 143(2):397–401, 2000.

[136] P. P. Mitra, P. N. Sen, L. M. Schwartz, and P. Le Doussal. *Diffusion propagator as a probe of the structure of porous media.* Physical Review Letters, 68(24):3555–3558, 1992.

[137] P. P. Mitra, P. N. Sen, and L. M. Schwartz. *Short-time behavior of the diffusion coefficient as a geometrical probe of porous media.* Physical Review B Cond. Matt., 47(14):8565–8574, 1993.

[138] L. L. Latour, K. Svoboda, P. P. Mitra, and C. H. Sotak. *Time-dependent diffusion of water in a biological model system.* Proceedings of the National Academy of Science U.S.A., 91(4):1229–1233, 1994.

[139] R. W. Mair, G.P. Wong, D. Hoffman, M. D. Hürlimann, S. Patz, L. M. Schwartz, and R. L. Walsworth. *Probing*

porous media with gas diffusion NMR. Physical Review Letters, 83(16):3324–3327, 1999.

[140] L. J. Zielinski and P. N. Sen. *Effects of finite-width pulses in the pulsed-field gradient measurement of the diffusion coefficient in connected porous media.* Journal of Magnetic Resonance, 165(1):153–161, 2003.

[141] R.J.S. Brown. *Connection between formation factor for electrical resistivity and fluid-solid coupling factor in Bioťs equations for acoustic waves in fluid-filled porous media.* Geophysics, 45(8):1269–1275, 1980.

[142] David L. Johnson and Pabitra N. Sen. *Multiple scattering of acoustic waves with application to the index of refraction of fourth sound.* Physical Review B, 24(5):2486–2496, 1981.

[143] P. N. Sen and P. J. Basser. *A model for diffusion in white matter in the brain.* Biophys J, 89(5):2927–2938, 2005.

[144] G.E. Archie. *The electrical resistivity log as an aid in determining some reservoir characteristics.* Transactions of the American Institute of Mining, Metallurgical and Petroleum Engineers, 146:54–62, 1942.

[145] C. Nicholson. *Diffusion and related transport mechanisms in brain tissue.* Rep. Prog. Physics, 64:815–884, 2001.

[146] David L. Johnson, T. J. Plona, C. Scala, F. Pasierb, and H. Kojima. *Tortuosity and Acoustic Slow Waves.* Physical Review Letters, 49(25):1840–1844, 1982.

[147] W. T. Perrins, D. R. Mckenzie, and R. C. Mcphedran. *Transport Properties of Regular Arrays of Cylinders.* Proceedings of the Royal Society of London A, 369:207–225, 1979.

[148] P. N. Sen, L. M. Schwartz, P. P. Mitra, and B. I. Halperin. *Surface relaxation and the long-time diffusion coefficient in porous media: Periodic geometries.* Physical Review B, 49(1):215–225, 1994.

[149] J. R. Banavar and L. M. Schwartz. *Magnetic resonance as a probe of permeability in porous media.* Physical review letters, 58(14):1411–1414, 1987.

[150] B. C. Masschaele, V. Cnudde, M. Dierick, P. Jacobs, L. Van Hoorebeke, and J. Vlassenbroeck. *UGCT: New X-ray radiography and tomography facility.* Nuclear Instruments and Methods in Physics Research Section A: Accelerators, Spectrometers, Detectors and Associated Equipment, 580:266–269, 2007.

[151] C. Beaulieu and P. S. Allen. *An in vitro evaluation of the effects of local magnetic-susceptibility-induced gradients on anisotropic water diffusion in nerve.* Magnetic Resonance in Medicine, 36(1):39–44, 1996.

[152] P. J. Basser and D. K. Jones. *Diffusion-tensor MRI: theory, experimental design and data analysis - a technical review.* NMR in Biomedicine, 15(7-8):456–467, 2002.

[153] J. R. Kalnin. *Calculations of the effective diffusion coefficient for inhomogeneous media.* Journal of Physics and Chemistry of Solids, 63:449–456, 2002.

[154] R. G. Thorne and C. Nicholson. *In vivo diffusion analysis with quantum dots and dextrans predicts the width of brain extracellular space.* Proceedings of the National Academy of Science, 103(14):5567–5572, 2006.

[155] K. C. Chen and C. Nicholson. *Changes in brain cell shape create residual extracellular space volume and explain tortuosity behavior during osmotic challenge.* Proceedings of the National Academy of Science, 97(15):8306–8311, 2000.

[156] E. J. Fordham, P. P. Mitra, and L. L. Latour. *Effective Diffusion Times in Multiple-Pulse PFG Diffusion Measurements in Porous Media.* Journal of Magnetic Resonance, Series A, 121(2):187–192, 1996.

[157] D. G. Norris. *The effects of microscopic tissue parameters on the diffusion weighted magnetic resonance imaging experiment.* NMR in Biomedicine, 14(2):77–93, 2001.

[158] H. G. Lipinski. *Monte Carlo simulation of extracellular diffusion in brain tissues.* Physics in Medicine and Biology, 35(3):441–447, 1990.

[159] A. Szafer, J. Zhong, and J. C. Gore. *Theoretical model for water diffusion in tissues.* Magnetic Resonance in Medicine, 33(5):697–712, 1995.

[160] J. C. Ford and D. B. Hackney. *Numerical model for calculation of apparent diffusion coefficients (ADC) in permeable cylinders– comparison with measured ADC in spinal cord white matter.* Magnetic Resonance in Medicine, 37(3):387–394, 1997.

[161] G. J. Stanisz, G. A. Wright, M. R. Henkelman, and A. Szafer. *An analytical model of restricted diffusion in bovine optic nerve.* Magnetic Resonance in Medicine, 37(1):103–111, 1997.

[162] P. J. Basser, T. Blumenfeld, G. Levin, Y. Yovel, and Y. Assaf. *AxCaliber: an MRI method to measure the diameter distribution and density of axons in neuronal tissue.* Magnetic Resonance Imaging, 25(4):550, 2007.

[163] Y. De Deene, R. Van de Walle, E. Achten, and C. De Wagter. *Mathematical analysis and experimental investigation of noise in quantitative magnetic resonance imaging applied in polymer gel dosimetry.* Signal Processing, 70(2):85–101, 10 1998.

[164] J. Sijbers and A.J. den Dekker. *Maximum likelihood estimation of signal amplitude and noise variance from MR data.* Magnetic Resonance in Medicine, 51(3):586–594, 2004.

[165] J.H. Jensen and J.A. Helpern. *Quantifying non-Gaussian water diffusion by means of pulsed-field-gradient MRI.* In Proceedings of the International Society for Magnetic Resonance in Medicine 11th scientific meeting, page 2154, Toronto, Canada, 2003.

Publications in international journals

[1] H. Q. Luong, E. Fieremans, K. Deblaere, J. Aelterman, B. Goossens, A. Pižurica, and W. Philips. *MRI resolution enhancement in the Fourier encoded plane.* to be submitted to IEEE transactions on medical imaging, 2008.

[2] N.P. Warlop, E. Achten, E. Fieremans, J. Debruyne, and G. Vingerhoets. *Directional diffusion and processing speed in relapsing-remitting multiple sclerosis and cognition in MS.* submitted to Brain and Cognition, 2008.

[3] E. Fieremans, Y. De Deene, S. Delputte, M. S. Özdemir, Eric Achten, and Ignace Lemahieu. *The design of anisotropic diffusion phantoms for the validation of diffusion weighted magnetic resonance imaging.* Physics in Medicine and Biology, 53(19):5405–5419, 2008.

[4] N.P. Warlop, E. Fieremans, E. Achten, J. Debruyne, and G. Vingerhoets. *Callosal function in MS patients with mild and severe callosal damage as reflected by diffusion tensor imaging.* Brain Research, 1226:218–225, 2008.

[5] E. Fieremans, Y. De Deene, S. Delputte, M.S. Özdemir, Y. D'Asseler, J. Vlassenbroeck, K. Deblaere, E. Achten, and I. Lemahieu. *Simulation and experimental verification of the diffusion in an anisotropic fiber phantom.* Journal of Magnetic Resonance, 190:189–199, 2008.

[6] M.S. Özdemir, H. Reyngoudt, Y. De Deene, H. S. Sazak, E. Fieremans, S. Delputte, Y. D'Asseler, W. Derave, I. Lemahieu, and E. Achten. *Absolute quantification of carnosine in human calf muscle by proton magnetic resonance spectroscopy.* Physics in Medicine and Biology, 52(23):6781–6794, 2007.

Publications in international conferences

[1] H.Q. Luong, E. Fieremans, K. Deblaere, J. Aelterman, B. Goossens, A. Pižurica, and W. Philips. *An In-Plane Resolution Enhancement Technique.* In Proceedings of the Radiological Society of North America, Chicago Illinois, USA, accepted, 2008.

[2] E. Fieremans, Y. De Deene, S. Baete, and I. Lemahieu. *Design of anisotropic fiber phantoms for the validation of diffusion weighted magnetic resonance imaging.* In Proceedings of the 9th International Bologna Conference Magnetic Resonance in Porous Media (MRPM9), pages P–066, Cambridge MA, USA, 2008.

[3] E. Fieremans, Y. De Deene, and I. Lemahieu. *Validation of models for the diffusion weighted MR signal in brain white matter.* In Proceedings of the IEEE International Symposium on Biomedical Imaging: from Nano to Macro, pages 7915–918, Arlington, USA, 2008.

[4] E. Fieremans, C. Chen, Y. De Deene, E. Achten, and I. Lemahieu. *The role of surface relaxivity and magnetic susceptibility in the design of anisotropic fiber phantoms.* In Proceedings 16th Scientific Meeting, International Society for Magnetic Resonance in Medicine, page 1788, Toronto, Canada, 2008.

[5] Y. De Deene, S. Baete, E. Fieremans, S. Delputte, B. Ozkalayci, S. Assecondi, V. Keereman, M. Özdemir, and S. Vandenberghe. *MR engineering research at the Ghent University.* In First Benelux in vivo MR methods symposium - 2007, pages 78–82, Nijmegen, the Netherlands, 2007.

[6] E. Fieremans, Y. De Deene, and I. Lemahieu. *Validation of diffusion imaging with anisotropic fiber phantoms.* In First Benelux in vivo MR methods symposium - 2007, page 28, Nijmegen, the Netherlands, 2007.

[7] E. Fieremans, Y. De Deene, S. Delputte, and I. Lemahieu. *Validation of diffusion models with anisotropic fiber phantoms.* In MRI of brain connectivity and microstructure, page C3, Dead Sea, Israel, 2007.

[8] E. Fieremans, Y. De Deene, Y. D'Asseler, E. Achten, and I. Lemahieu. *Quantifying the diffusion in an anisotropic fiber phantom.* In Book of Abstracts EUROMAR Magnetic Resonance Conference, page 183, Tarragona, Spain, 2007.

[9] E. Fieremans, S. Delputte, Y. De Deene, Y. D'Asseler, E. Achten, and I. Lemahieu. *Simulation and experimental verification of the diffusion in the interstitial space.* In Proceedings of the joint annual meeting ISMRM-ESMRMB, page 1539, Berlin, Germany, 2007.

[10] S. Delputte, H. Dierckx, E. Fieremans, Y. D'Asseler, R. Achten, and I. Lemahieu. *Postprocessing of brain white matter fiber orientation distribution functions.* In Proceedings IEEE International Symposium on Biomedical Imaging: from Nano to Macro, pages 784–787, Arlington, USA, 2007.

[11] E. Fieremans, Y. De Deene, S. Delputte, E. Achten, Y. D'Asseler, and I. Lemahieu. *Simulation of the diffusion in the interstitial space of a fiber phantom.* In Proceedings of the IEEE International Symposium on Biomedical Imaging: from Nano to Macro, pages 788–791, Arlington, USA, 2007.

[12] E. Fieremans, S. Delputte, Y. De Deene, Y. D'Asseler, E. Achten, I. Lemahieu, and R. Van de Walle. *Phantom optimization for diffusion tensor magnetic resonance imaging.* In Proceedings of the International Society for Magnetic Resonance in Medicine 14th scientific meeting, page 1036, Seattle, USA, 2006.

[13] S. Delputte, E. Fieremans, Y. Dedeene, Y. D'Asseler, E. Achten, I. Lemahieu, and R. Van de Walle. *Quantitative Validation of White Matter Fiber Tractography by use of an Anatomically Realistic Synthetic Diffusion Tensor Phantom.* In Proceedings of the International Society for Magnetic Resonance in Medicine 14th Scientific Meeting, page 2739, Seattle, USA, 2006.

[14] Steven Delputte, H Dierckx, Els Fieremans, Yves D'Asseler, Eric Achten, and Ignace Lemahieu. *Correlation and regularization*

of white matter fiber orientation distribution functions. In Proceedings of the IEEE/EMBS Benelux symposium, Belgian Day on Biomedical Engineering, page 65, Brussel, 2006.

[15] E. Fieremans, S. Delputte, Y. De Deene, E. Achten, Y. D'Asseler, I. Lemahieu, and R. Van de Walle. *Modelling the diffusion in the interstital space of a fiber phantom.* In Book of abstracts European Society for Magnetic Resonance in Medicine and Biology 23rd annual scientific meeting, page 596, Warsaw, Poland, 2006.

[16] E. Fieremans, S. Delputte, Y. De Deene, Y. D'Asseler, E. Achten, I. Lemahieu, and R. Van de Walle. *Comparison of fiber materials for a head diffusion phantom.* In Book of abstracts 22nd annual scientific meeting European Society for Magnetic Resonance in Medicine and Biology, page S291, Bazel, Switserland, 2005.

[17] E. Fieremans, S. Delputte, Y. De Deene, K. Deblaere, B. Truyens, Y. D'Asseler, E. Achten, I. Lemahieu, and R. Van de Walle. *Initial results of a hardware diffusion head phantom.* In Book of abstracts of the European Society for Magnetic Resonance in Medicine and Biology 22nd annual scientific meeting, pages S291–S292, Bazel, Switserland, 2005.

[18] E. Fieremans, S. Delputte, K. Deblaere, Y. De Deene, B. Truyens, Y. D'Asseler, E. Achten, I. Lemahieu, and R. Van de Walle. *A flexible hardware phantom for validation of diffusion imaging sequences.* In Abstracts of the International Society for Magnetic Resonance in Medicine, thirteenth scientific meeting & exhibition, page 1309, Miami Beach, USA, 2005.

[19] S. Delputte, A Leemans, E. Fieremans, Y. De Deene, Y. D'Asseler, I. Lemahieu, E. Achten, J. Sijbers, and R. Van de Walle. *Density Regularized Fiber Tractography of the Brain White Matter using Diffusion Tensor MRI.* In Abstracts of the International Society for Magnetic Resonance in Medicine, 13th scientific meeting, page 1309, Miami Beach, USA, 2005.

Publications in national conferences

[1] B. Jeurissen, A. Leemans, E. Fieremans, and J. Sijbers. *Fiber tractography on a crossing fiber phantom using constrained spherical deconvolution MRI*. In Liege Image Days 2008: Medical Imaging, March 2008.

[2] Els Fieremans, Y. De Deene, and I. Lemahieu. *Phantom design for the validation of diffusion magnetic resonance imaging in brain white matter*. In Abstracts of the 8th FTW PhD symposium, Gent, 12 2007.

[3] E. Fieremans, S. Delputte, Y. De Deene, Y. D'Asseler, E. Achten, I. Lemahieu, and R. Van de Walle. *Phantom design for diffusion tensor magnetic resonance imaging*. In F. Jacobs, editor, Abstract book of the 21st annual symposium of the Belgian Hospital Physicist Association, page 64, Gent, 1 2006.

[4] E. Fieremans, S. Delputte, Y. De Deene, K Deblaere, Bart Truyens, Y. D'Asseler, E. Achten, I. Lemahieu, and R. Van de Walle. *Initial results of a hardware diffusion head phantom*. In M. Nyssen, C. Veraart, and P. Verdonck, editors, Abstract book of the fifth Belgian Day on Biomedical Engineering, page 62, 10 2005.

[5] S. Delputte, E. Fieremans, K. Deblaere, Y. De Deene, Y. D'Asseler, I. Lemahieu, R. Van de Walle, and E. Achten. *A flexible hardware phantom for validation of diffusion tensor MRI tractography*. In M. Nyssen, C. Veraart, and P. Verdonck, editors, Abstract book of the 4th Belgian day on Biomedical Engineering, page 40, 10 2004.

[6] Els Fieremans and Steven Delputte. *Sequence design and Validation for Diffusion Tensor Magnetic Resonance Imaging*. In Abstracts of the 5th FTW PhD symposium, Gent, 12 2004.

[7] E. Fieremans. *Sequence design for diffusion tensor magnetic resonance imaging.* In Abstracts of the 4th FTW PhD symposium, Gent, 12 2003.